UNIVERSITY OF CAPE TOWN

FACULTY OF ENGINEERING AND THE BUILT ENVIRONMENT

Department of Civil Engineering

An Investigation into the Volume Change Characteristics of Loess Like Soil in Mount Moorosi Village in Lesotho

Geotechnical Engineering Group

Author: Monica Damane
Supervisor: Assoc. Prof. Denis Kalumba
Co-supervisor: Mrs. Laxmee Sobhee-Beetul

[June 2019]

A thesis submitted in partial fulfilment of the requirement for the award of the degree of Master of Science in Engineering Specialising in Geotechnical Engineering at the University of Cape Town

Plagiarism declaration

1. Plagiarism is using another's work and to pretend that it is one's own. I know that plagiarism is wrong.

2. I have used the Harvard convention for citation and referencing. Each significant contribution to and quotation in this report from the work or works of the other people have been attributed and has been cited and referenced.

3. This report is my own work.

4. I have not allowed and will not allow anyone to copy my work with the intention of passing it off as his or her own work.

Signature: … Signed by candidate Date: 17/06/2019

Student Name: Monica Damane (DMNMON001)

Dedication

To my grandmother and late parents, for undoubtedly and always believing in me.

Acknowledgements

Deep appreciation to my supervisor, Assoc. Prof. Denis Kalumba, for his invaluable commitment, patience, constructive input and guidance throughout this endeavour. I am forever indebted to him. Further gratitude to my co-supervisor, Dr. Laxmee Sobhee-Beetul, for her intellectual expertise and indispensable contribution.

The staff at the University of Cape Town are greatly thanked for the outstanding assistance, particularly Mr. Noor Hassen, Mr. Christopher Ceasar, Mr. Elvino Witbooi, Mr. Tahir Mukaddam, and Ms. Lita Nolutshungu at the university's geotechnical laboratory, Mr. Charles Nicholas in the Workshop, Assoc. Prof. Kirsten Corin and Ms. Rachel Cupido in the Centre for Minerals Research and Mrs. Miranda Waldron in the Centre for Imaging Analysis.

The MasterCard Foundation Programme at the University of Cape Town is highly treasured for its financial support and for granting me the opportunity to pursue my dream. The program manager, Ms. Carol Ojwang, co-ordinator Mr. Xolani Mkoba, recruitment and peer mentor officer Ms. Insaaf Isaacs, administrator Mr. Riyaadh Fakier and advisor for careers, internships and opportunities Mrs. Jean, are all much appreciated for organising remarkable leadership activities during my time on the programme.

Sincere gratitude to my friends: Charles, Daniel, Edward, Emmanuelle, Jason, Katlego, Lisebo, Moshoeshoe, Motlatsi, Nandipha and Ruben for the constant moral support and encouragement throughout the research.

A special thank you goes to my family for unquestionably and always believing in me, even when I did not have faith in myself. Tlotliso is particularly acknowledged for his priceless assistance in the in-situ study. The Mount Moorosi community is also honoured for being co-operative during my field work.

You will all be endlessly cherished in my heart.

Monica Damane
(DMNMON001)

Abstract

The Mount Moorosi village is situated in the Senqu River Valley of southern Lesotho, within the Stormberg landform. The integrity and aesthetic appearance of nearly all the structures in this area are undermined by recurrent cracks. At present, no apparent institutionalised effort had been conducted to investigate the source of this problem. The crack patterns were associated with the possible volume change of the underlaying loess like soil. This soil has caused a disastrous failure to brittle civil engineering structures in various parts of the world. Its behaviour is attributed to sand and silt particles bonded by minerals, which become active upon saturation and induce hydrocollapse settlement. This study characterised the volume change properties of the underlaid deposits in Mount Moorosi. The research utilised representative samples from trial pits in the study region to perform laboratory experiments such as the Atterberg limits, wet sieving, sedimentation, free swell, x-ray diffraction, scanning electron microscope and slaking. The consolidated undrained tests and hydrocollapse potential were also determined from the GEOCOMP triaxial and Global Digital System oedometer, respectively.

Results revealed that Mount Moorosi is generally underlaid by a more than 3 m thickness of low plasticity (9 to 17 %) silty-sandy loess. The material had significant warping (up to 27 mm) in linear shrinkage that illustrated potential inducement of detrimental stresses to the superimposed structures during drying. The identification and quantification of the mineralogy composition clearly evidenced the passive minerals (quartz, feldspar and mica) to be predominant (86 %), while the active phases (kaolinite, carbonates, sulfates, halides, the oxides and hydroxides of aluminum and iron) were subordinate (14 %), which substantiated potential soil settlement upon wetting. Furthermore, the micrographs depicted structures that synergistically enhanced the collapse properties of the tested deposits. These included the porous clays, silts bonded by clay and silts coated with clay, which all rendered a metastable fabric. A comparison of the stress-strain graphical plots from the consolidated undrained tests at the field and saturated moisture contents indicated a drastic reduction (up to 73 %) in deviator stress at saturated water content. This was attributed to the augmentation of the interparticle spaces, caused by a rise of up to 337 kPa in pore water pressure. Shear strength parameters obtained from Mohr's failure envelopes were also decreased by up to 80 %. The hydrocollapse index measured from the oedometer tests ranged from 10 to 15 % at a vertical stress of 200 kPa. It indicated severe settlement problems for structures constructed on this soil. This was caused by the loss in shear strength of the soil under the saturated conditions and a high slaking mechanism that reached a maximum rating of 4. Generally, the mineralogy composition, morphology, saturated shear strength, slaking and hydrocollapse index collectively indicated the possibility of soil volume decrease. In fact, the check for serviceability limit state demonstrated a settlement that exceeded the tolerable value of 50 mm. The cracks observed on structures were, therefore, related to soil settlement. This study recommends further research on suitable ground techniques to minimise settlement, thereby improving the durability of structures. Moreover, investigations should be conducted to understand the pressure induced by warping during shrinkage.

Table of Contents

List of Figures

List of Tables

Notations and Abbreviations

AASHTO	American Associate of State Highway and Transportation
AMSL	Above Mean Sea Level
ASTM	American Standard Test Methods
BS	British Standard
CL	Clay of Low Plasticity
CH	Clay of High Plasticity
CU	Consolidated Undrained Test
E	East
ESP	Exchangeable Sodium Percentage
GDS	Global Digital System
Gs	Specific Gravity
LL	Liquid Limit
MH	Silt High Plasticity
ML	Silt of Low Plasticity
OL	Organic Soil of Low Plasticity
OH	Organic Soil of High plasticity
PI	Plasticity Index
PL	Plastic Limit
RSA	Republic of South Africa
S	South
SEM	Scanning Electron Microscope
SL	Shrinkage Limit
SLS	Serviceability Limit State
TP	Trial Pit
TLB	Tractor Loader Backhoe
UCT	University of Cape Town
ULS	Ultimate Limit State

USA		United States of America
USCS		Unified Soil Classification System
USDA		United States Department of Agriculture
XRD		X-Ray Diffraction
B	mm	Foundation Breadth
H	m	Height of Soil Stratum
Q	kN/m	Factored Load Applied to Strip Footing
Q_s	kN/m^2	Pressure Applied to Strip Footing
R	kN/m	Bearing Capacity Resistance
S	mm	Field Soil Settlement
D	m	Depth of footing,
c	kPa	Soil Cohesion
c_c	-	Compression Index
c_s	-	Swell Index
$\emptyset$	°	friction angle
τ	kPa	Shear Strength
σ	kPa	Normal Stress
σ_z	kPa	Soil Vertical Pressures
$\Delta\sigma$	kPa	Pressure Increment
i	-	Collapse Coefficient,
e_0	-	Initial Void Ratio prior
e_1	-	Void Ratio Prior to Wetting
Δe	-	Change in void ratio
I_c	%	Collapse Potential
I_e	%	Collapse Index
Δh	mm	Change in Height in Oedometer Test
h_o	mm	Initial Height in Oedometer test
m	g	Soil Mass
ρ	kg/m^3	Field Bulk Density

q	kPa	Overburden Pressure
sw	%	Soil Moisture Content
tw	%	Target Field Moisture Content
V	kN/m	Vertical Loads
v	cm^3	Volume of Oedometer Ring
w	%	Additional Moisture
γ	kN/m^3	Unit Weight
γ_{c_u}	-	Partial Factor Undrained Cohesion
γ_G	-	Partial Factor for Foundation Unfavourable Permanent Action
γ_{Gfev}	-	Partial Factor for Foundation Favourable Permanent Action
$\sigma p'$	kPa	Effective Pre-consolidation Pressure
γ_Q	-	Partial Factor for Foundation Unfavourable Variable Action
γ_{Qfev}	-	Partial Factor for Foundation Favourable Variable Action
$\gamma_\emptyset$	-	Coefficient of shearing Resistance
γ_{R_v}	-	Partial Factor for Bearing Resistance

1 Introduction

1.1 Background of the Study

Nearly all houses in the Mount Moorosi village have sustained cracks, which undermine both their aesthetic appearance and structural integrity. In civil engineering, a relatively thin breakage on the surface of masonry (that is, units of bricks or stones bonded with mortar) and concrete is termed a 'crack'. Cracks on structures in this village had various patterns, including the hairline, diagonal, vertical and stepped (Figure 1-1). They were observed above and below building windows, adjacent to the door frames, on concrete flooring and ceramic tiles. In some houses, they were followed by interior plaster spalling, slight wall leaning, and were recurrent. According to the South African Home Building Manual (2014), cracks less than 5 mm wide are characterised as minor damage, while the greater sizes indicate a significant structural failure. Accordingly, cracks noted were considered a mixture of minor and major deformations. Therefore, the serviceability limit state, one of the principle criteria to ensure the stability of structures, was affected.

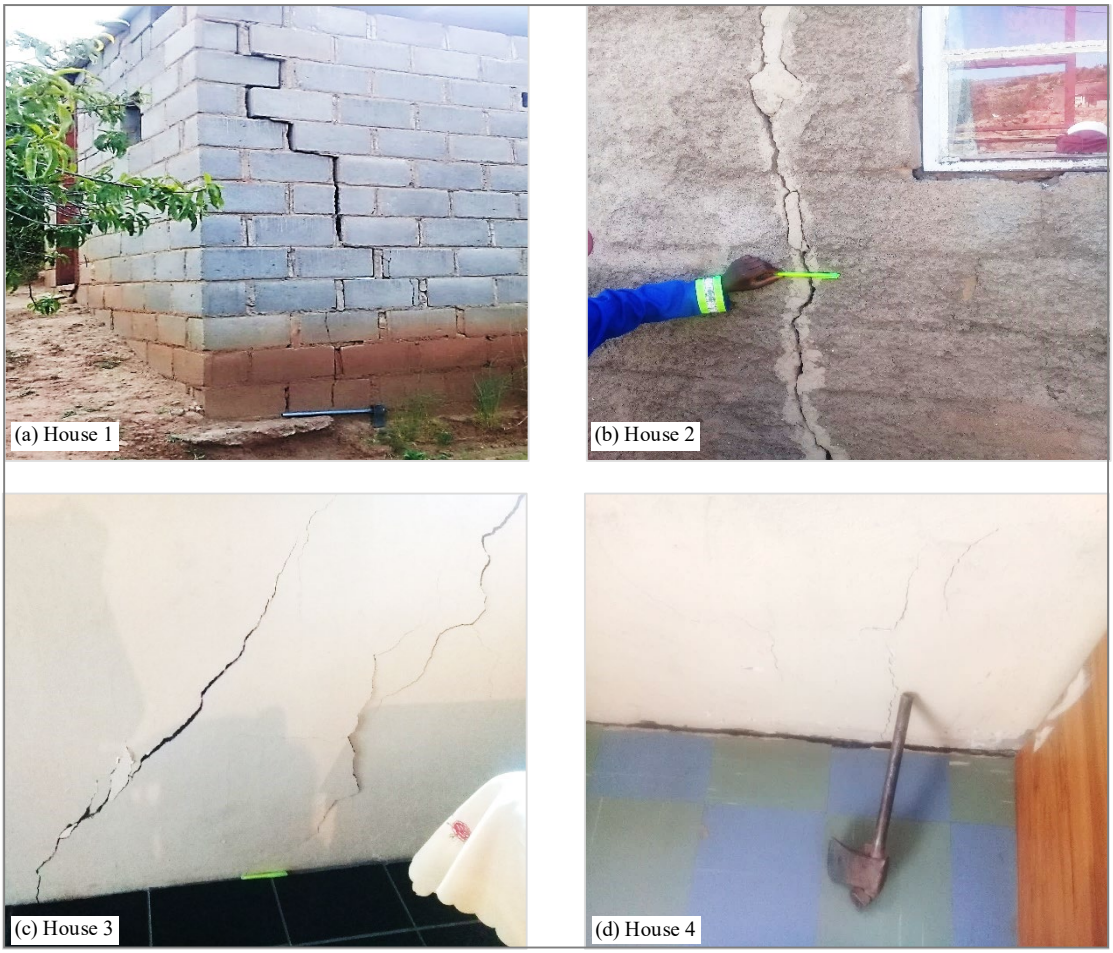

Figure 1-1, Cracks on some of the selected houses in the Mount Moorosi village

The Mount Moorosi village is situated within the Senqu River Valley at a latitude of 30°16'39.76" S and longitude of 27°52'14.98" E, at an average elevation of 1700 above mean sea level (AMSL). It is located 211.8 km south of Maseru, which is the capital city of a landlocked country, Lesotho. To date, no apparent institutionalised effort has been undertaken to investigate the source of structural cracks in this area. This renders it significantly difficult to design and construct durable houses. According to Page (2001), Thomaz et al. (2014) and Arvind (2017), the noted crack patterns are generally attributed to the volume change (swell and settlement) of the founding soil. Slight ground movements are unfavourable due to the exceedingly brittle nature and low tensile strength of building materials (Whitlow, 1995). Consequently, the observed cracks were possibly caused by displacement of the underlaying loess-like deposits.

Loess is the most well-known collapsible soil covering roughly 10 % of the world's land area (Howayek et al., 2012). It can sustain applied stresses with small settlements at low moisture content but undergoes a substantial reduction in volume upon wetting. Principally, its metastable property originates from the skeletal structure of individual core particles, particularly silt and sand, that are bonded by clay and carbonates (Pye, 1987). The formed fabric has high shear strength at a relatively low moisture content, but drastically loses it on saturation and triggers settlement of the loaded grains. Pertaining to this property, the loessal sediments induced catastrophic deformation to structures in various parts of the world (Grigoryan, 1991; Djogo & Milović, 2013; Yuan-Xun et al., 2013; Santrač et al., 2015; Kalpakci, 2017).

Watermeyer & Tromp (1992) reported that the cost incurred during rehabilitation in damage caused by ground movements can reach up to 50 % of the total initial price of the building construction. This shows that the identification and understanding of the soils susceptible to displacement is important for safe and long-lasting foundation designs. It was, thus, imperative to investigate the volume change characteristics of loess-like deposits in Mount Moorosi.

1.2 Research Objectives

The primary aim of the study was to experimentally determine the potential volume change characteristics of soil in Mount Moorosi. To understand the behaviour of the soil under different environments, the following specific objectives were developed:

- Establish the effect of field and saturated moisture contents on both shear stress and strength parameters,
- Compare the void ratio from tests at field and saturated moisture contents, and
- Assess the effect of magnitude of the applied effective stress on void ratio.

Tests were conducted in Global Digital System (GDS) double oedometer. In addition, the following tests were executed to achieve the main objective of the research:

- Index tests for particle size gradation and profiling the trial pits,
- Free swell test to establish the volume increase of the wetted and unconfined soil,
- X-Ray Diffraction (XRD) to identify and quantify minerals that made up the soil,

- Scanning Electron Microscope (SEM) to establish the microstructural arrangement of particles,
- Triaxial test to obtain the shear strength parameters, and
- Slaking test to determine the susceptibility of the soil to collapse.

1.3 Scope and Limitation of this Investigation

The scope of the dissertation was specifically limited to volume change investigation of soil samples collected from Mount Moorosi in Moeling. Additionally, tests were conducted on reconstituted, instead of undisturbed specimens, to avoid damage during a long haulage from the sampling site to the geotechnical laboratory at University of Cape Town (UCT). Furthermore, the practical application analysis of the research findings was solely done for shallow footings, as these were typical in the study region.

1.4 Thesis Overview

Chapter 1: The study is introduced, and the objectives of the research are presented.

Chapter 2: A review of the literature on the theoretical background of the problem soils is provided. The background of loess deposits and the documented problems on the superimposed structures are covered.

Chapter 3: The geography, regional geology and damage of structures in Mount Moorosi are highlighted.

Chapter 4: The field methodologies, laboratory experimental procedures and testing equipment are outlined.

Chapter 5: The research findings are reported and discussed. These include the data from fieldwork and laboratory investigation.

Chapter 6: A discussion of the practical application which is based on the research test results is provided.

Chapter 7: The outcomes of the study are summarised, conclusions are made and the recommendations for furthering the research are presented.

2 Literature Review

2.1 Introduction

In this chapter, an overview of soil genesis as well as particle size classification is highlighted, and problem soils are reviewed. This is followed by a discussion about the theoretical background available in current research on loess formation, distribution, mineralogy composition, physical characteristics and the potential problems on superimposed structures.

2.2 Soil Formation

To an engineer, soil is an unaggregated deposit of minerals and or organic particles covering a substantial portion of the earth's crust (Punmia et al., 2012). It is formed by the disintegration of rocks into smaller particles through chemical and physical actions. Physical weathering, also the main source of cohesionless soil, is caused by periodical temperature changes, and impact from water, ice, wind, plants and animals. Oxidation, hydration, carbonation, and leaching by organic silts and water are the processes that occur in chemical weathering to form clay minerals as well as other particles (Craig, 2004). The soil may remain nearby the parent rock as a residual or may be transported to a new location by water, wind or animals. Figure 2-1 illustrates the soil and rock cycle.

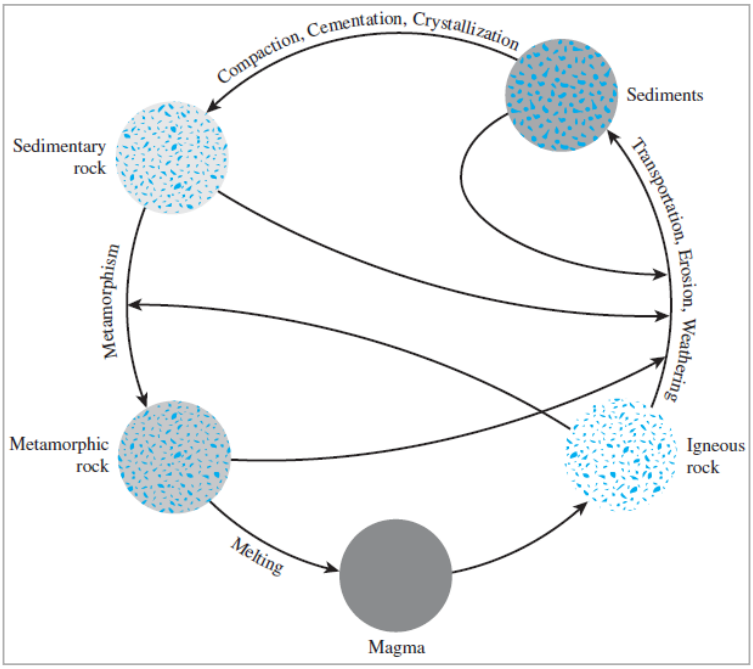

Figure 2-1, The rock and sediments cycle (Source: Das, 2013)

Rocks are mainly classified into igneous, sedimentary and metamorphic groups (Figure 2-1). The cooling and solidification processes transform the molten magma ejected from the earth's mantle by volcanic eruptions, into igneous rock. This resultant rock is broken into smaller sediments

that are sometimes relocated. In chemical weathering, these deposits have a different mineral composition from their parent material, whereas mineralogical composition remains unaltered in physical weathering (Craig, 2004). Grains such as gravel, silt, and clay are compacted by overburden pressure, and in the presence of cementing agents such as iron oxide, calcite, dolomite along with quartz, a sedimentary rock is formed (Das, 2013). Sedimentary and igneous rocks are metamorphosed into a metamorphic group by heat and pressure without melting them. At an intense heat, this rock is melted, and the rock cycle is repeated.

2.3 Soil Grain Classification

The various types of soils are generally classified for their arrangement into groups according to their agricultural and engineering properties (Punmia et al., 2012). However, the main objective in engineering is to investigate the soil's suitability for construction (Punmia et al., 2012). The United States Department of Agriculture (USDA), International Method, American Associate of Modified Wentworth Method, State Highway and Transportation (AASHTO), British Methods as well as the Unified Soil Classification System (USCS): are some of the numerous soil classification systems currently available (Table 2-1). Soils are mainly classified into granular/rock fragments or fine earth, based on particle size gradation. Granular particles include boulders, stones, cobles, gravel and sand, while silt and clay are the fine grains.

Table 2-1, Grain-size classification (Source: United States Department of Agriculture, 2017)

Classification systems	Particle sizes, mm						
	Fine earth		Rock fragments				
	Clay	Silt	Sand	Gravel	Cobless	Stones	Boulders
United States Department of Agriculture (USDA)	< 0.002	0.002 – 0.05	0.05 – 2	2 – 76	76 – 250	250 – 600	> 600
International Method		0.002 – 0.02	0.02 – 2	2 – 20	> 20		
Modified Wentworth Method	< 0.004	0.004 – 0.062	0.062 – 2	2 – 64	64 to 256	256 to 4092	
American Associate of State Highway and Transportation (AASHTO)	< 0.005	0.005 – 0.075	0.075 to 2	2 – 75			> 75
British Methods	< 0.002	0.002 – 0.06	0.062 – 2	2 – 60	60 – 200		> 200
Unified Soil Classification System (USCS)	< 0.075		0.075 – 4.75	4.75 – 75	75 – 300		> 300

In fine soils, systems such as the USDA and International Method classify clay as particles finer than 0.002 mm, while AASHTO regards clay as particles smaller than 0.005 mm. The Unified Method, contrarily, classifies clay collectively with silt, as particles with sizes less than 0.075

mm. Like clay, the size of silts and sand are inconsistent among grain classification methods. It has, however, been noticed that sand (0.075 and 2 mm), silt (0.063 to 0.002 mm) and clay (finer than 0.002 mm) are used in the literature to identify loessal deposits (Smalley, 1990; Dijkstra et al., 1994; Klukanova & Frankovska,1995; Nouaouria et al., 2008).

The USCS uses the Atterberg limits, in conjunction with soil particle distribution, for further classification of fine soils. In this system, soil is mainly divided into coarse-grained when more than 50 % is retained on the 0.075 mm sieve, and fine-grained when 50 % or more passes through. Silts, clay and organic soils are classified based on their plasticity, and may plot either above or below the A-line of USCS chart (Figure 2-2). The soils are classified as clay of low plasticity (CL) or high plasticity (CH), silt of low plasticity (ML) or high plasticity (MH) and organic soil of low plasticity (OL) or high plasticity (OH).

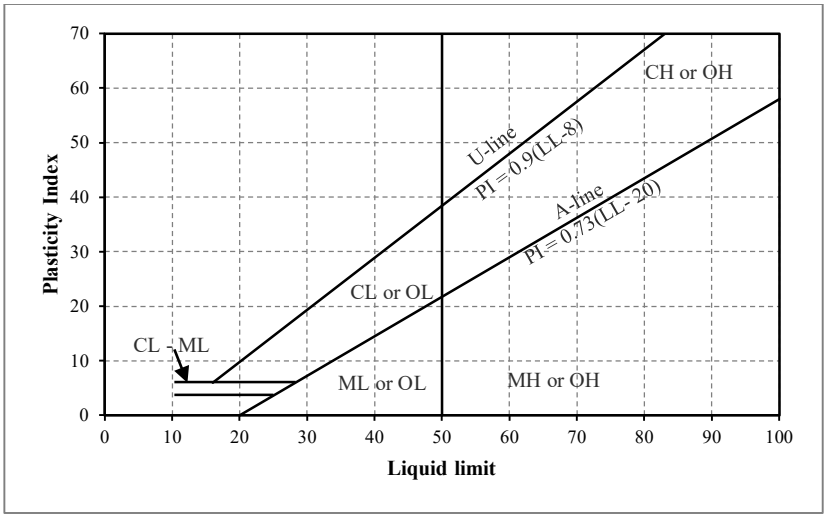

Figure 2-2, Plasticity chart as per USCS (Source: Das, 2007)

2.4 Problem Soils

Soils that induce detrimental stresses to structures are regarded problematic in civil engineering. Settlement, expansion, shrinkage, and low bearing capacity are some properties related to them. These sediments include expansive, soft clay, dolomitic residuals, dispersive, liquefiable, and collapsible soils (Byrne & Berry, 2008).

2.4.1 Expansive Soils

Expansive soils expand when wet and reduce in volume when dry. These properties are attributed to the type of clay mineral present in soil. Montmorillonite is the most problematic of all clay minerals because of its weak oxygen bonds between structural units, while kaolinite is the least harmful (Fredlund, 1975). During shrink and swell cycles, exerted stresses result in the formation of cracks on structures. Expansive soils can apply pressure as high as 263 kPa (Rogers et al., 2015). Figure 2-3 shows cracks on a concrete floor caused by expansive soil in Kibaha, Tanzania.

Figure 2-3, Concrete floor crack caused by expansive soil in Tanzania (Source: Lucian, 2006)

Kitcher (1980) put forward an estimate of R1000 million for the repair of houses built (or to be erected) on expansive clay from 1980 to 2000 in South Africa. This is an indication that the expansive soils pose a serious hazard to structures. It was established that the widespread igneous basalt within the Drakensberg mountain range in Lesotho disintegrated into such soils (Rooy & Schalkwyk, 1993; Bell & Haskins, 1997). It is, therefore, necessary to investigate the volume change magnitude of Lesotho soils.

2.4.2 Soft Clay

Soft clay is characterised as a soil that generally gives compressibility, shear strength and settlement time-related problems. Its significant consolidation is related to its high-water content. In fact, Jone & Davies (1985) pointed out that soft clays are normally consolidated. In this state, an increase in effective stress causes higher pore pressure and successive deformation rates. Figure 2-4 depicts a failed bridge abutment that occurred due to the excess pore pressure in the underlying soft soil.

Figure 2-4, A tilted bridge abutment in Indonesia (Source: Rahardjo, 2014)

In Malaysia, a settlement of 2.4 m in soft clay caused a failure of a road embankment (Huat, 1998). Jone & Davies (1985) reported that settlement of up to 30 % of the total height of embankments could occur in deep soft clay deposits.

2.4.3 Dolomite Residuals

Certain parts of the world are underlain by dolomite rocks, which undergo catastrophic collapse in the presence of water. These rocks consist of soluble carbonates that are leached by weakly acidic groundwater from the rain, as seen in Equation 2-1 (Blight & Leong, 2012).

$$CaMg(CO_3)_2 + 2\,H_2CO_3 \rightarrow Ca(HCO_3)_2 + Mg(HCO_3)_2 \qquad \textbf{Equation 2-1}$$

By-products of this are a very low shear strength, porous and permeable residuals, which can easily lose support on addition of water (Oosthuizen & Richardson, 2011). The resulting ground deformation may be in the form of either gradual caving settling (dolin), or rapid and disastrous collapse, termed as a 'sinkhole' (Jennings et al., 1965). This ground failure is a critical concern as it may result in a loss of life and/or structures. Wagener (1985) reported that a Driefontein mine crusher was suddenly swallowed by a 55 m diameter and 30 m deep sinkhole and killed 29 people in South Africa in 1962 (Figure 2-5). Furthermore, more than R1 billion of damages caused by sinkholes was estimated (Buttrick et al., 2001).

Figure 2-5, The sinkhole that swallowed a Driefontein mine crusher in South Africa (Source: Oosthuizen & Richardson, 2011)

2.4.4 Dispersive Soils

Dispersive soils deflocculate into the suspended colloids in the presence of relatively pure water. This property is attributed to high quantities of exchangeable sodium percentage, ESP (Elges, 1985). The soil dispersion is low at the ESP (Equation 2-2) of less than 6 %, but higher at the values past 15 % (Gerber & Harmse, 1987; Bell & Maud, 2015).

$$ESP = \frac{exchangeable\ sodium}{cation\ exchange\ capacity} \times 100 \qquad \textbf{Equation 2-2}$$

In a dispersed state, soil can easily be eroded by flowing water and thus initiate the formation of piping. This kind of failure has been observed in natural slopes, embankments and earth dams (Elges, 1985). Figure 2-6 depicts the eroded dispersive soil on an embankment.

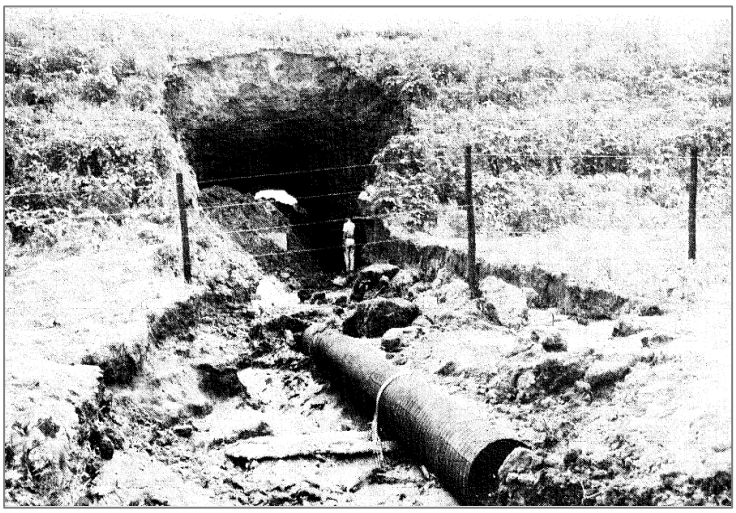

Figure 2-6, A damaged embankment constructed of dispersive soil (Source: Edgar, 1991)

2.4.5 Liquefiable Soils

Liquefiable soils are major problems in earthquake-prone zones, particularly in areas with high-water table. During earthquakes, cyclic pore pressure generated by seismic waves causes significant loss of strength and stiffness in the soil, resulting in disastrous destruction of superimposed objects (Seed et al., 2001). The types of soil that can be affected by this natural hazard remains a topic of controversy. Finn & Fujita (2002) reported that the phenomenon is induced in sands and silts. In contrast, Seed et al. (2001) mentioned the cases of liquefaction in gravelly and clayey soils. Figure 2-7 shows tilted buildings in Chile, due to liquefaction induced by earthquake.

Figure 2-7, Tilting of buildings induced by foundation soil liquefaction in Chile (Source: Bray et al. 2000)

2.4.6 Collapsible Soils

Collapsible soils can withstand relatively large imposed stresses with minor settlement at low moisture content, but display significant volume decrease at higher water content, under the same loading conditions (Schwartz, 1985). Vandanapu et al. (2016) reported a water-induced settlement of up to 260 mm on the boundary wall underlaying a collapsible soil (Figure 2-8).

Figure 2-8, Damage on boundary wall as a result of settlement induced by collapsible soils in Abu Dhabi (Source: Vandanapu et al., 2016)

Collapsible soils are mainly classified into natural and man-made compacted soils. Natural soil is further categorised into alluvium, aeolian, colluvium and residuals based on deposition method (Rust et al., 2010; Howayek et al., 2012; Rogers, 1995). These sediments are respectively deposited by water, air fall and gravity. Conversely, residuals remain at the place of formation.

The focus of this study is on loessal deposit, which is widely-known collapsible deposit, covering roughly 10 % of the world's land area (Egri, 1972; Howayek et al., 2012). Loess is an aeolian deposit with carbonate content varying from 0.2 to 30 % (Egri, 1972). However, Pye (1984), Glass (1986) and Konrad et al. (2004) recognised soils that are not transported by the wind but demonstrate comparable properties as aeolian loess. These include alluvial, colluvial, proluvial as well as lacustrine deposits, and are referred to as 'loess-like' deposits.

2.5 Loessal Deposits

Dijkstra et al. (1994) describe loess as a deposit mostly consisting of quartz in the silt range (0.020 to 0.060 mm). In addition, Pecsi (1990) suggested that grains ranging from 0.010 to 0.050 mm make up about 50 to 70 % by weight in loess. It is inferred from this literature that the distinct mineralogical composition and particle size distribution are used to distinguish loess from other sediments. Moreover, Gibbs & Holland (1960) made it clear that unless a cohesive matrix is developed, a soil cannot be considered as loess. Different types of loess sediments are classified in Table 2-2, based on deposition methods.

Table 2-2, Types of loessal deposits (Source: compiled from Pye, 1984)

Loess name	Description
Loess	A windblown silt deposit consisting primarily of quartz, feldspar, mica, clay minerals and carbonate grains in variable proportions.
Reworked loess	Consists of primary loess which has been translocated by running water and slope actions. Generally accumulates in valley bottoms, lakes and on river terraces.
Weathered loess	Its sedimentary characteristics have been distinctly changed by weathering, soil formation, and diagenesis. This is characterised by thick loess profiles with alternating sheets of unweathered and weathered loess.
Loess-like deposits	Deposits that have many of the sedimentological properties of aeolian loess, but have never been transported by wind.
Loessite	First proposed by J.B. Wood worth to define lithified loess rock in the sedimentary record.

2.5.1 Loess Deposits Formation

Smalley (1990) reported that glacial grinding remains the greatest source of loessal sediments. A glacier is a massive ice gradually formed by snow accumulation on high cold mountains. The freezing and thawing process during its development fractures the adjacent and beneath rocks into finer particles. When this ice has grown large, high pressure on its base results in the formation of water, which triggers basal sliding. Consequently, glaciers slowly move downhill under gravitational pull (Figure 2-9).

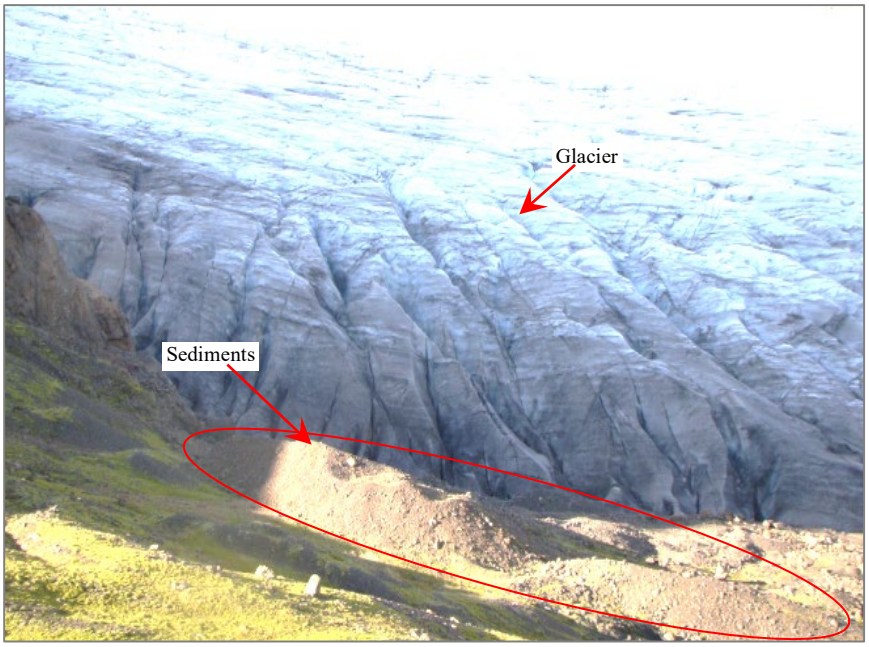

Figure 2-9, Soil produced by glacier movement (Source: British Society for Geomorphology, 2018)

The movement is also caused by the breaking of the rocks beneath, and deformation induced by crystal slippage within a glacier (British Society for Geomorphology, 2018). Throughout the downhill movement, abraded rocks are dragged along. The higher temperature at the foothill causes ice to melt and expose transported sediments (Figure 2-9). These sediments are constantly entrained in wind and translocated to accumulation planes during a blowy weather. However, glaciers are restricted to specific areas and cannot be accountable for all geographical deposits of loess. Smith et al. (2002) investigated the formation of non-glacial loess and concluded that any sufficient energies can generate silt during the geomorphic process (that is, the formation of landscapes). Other methods include weathering in a cold or hot environment (Smith et al., 2002). The Chinese loess plateau and loess within the locality of Mount Kenya were attributed to high cold regions (Zeuner, 1950; Sun, 2002). Table 2-3 summarises the various mechanisms capable to forming silt-sized particles.

Table 2-3, Possible mechanisms of silt particle formation suggested in the literature (Source: Pye, 1987)

Mechanism	Best reference	Description
Frost weathering	Zeuner (1949)	The importance of frost action in forming silt was observed on Mount Kenya.
Glacial grinding	Smalley (1966)	Virtually all great loess deposits around the world are located on the margins of areas that experienced Pleistocene glaciation.
Release from phyllosilicate parent rocks	Kuenen (1969)	The release of particles from fine-grained metamorphic rocks such as schists and phyllites could provide an important source of silt.
Fluvial comminution	Moss et al. (1973)	It was noted that coarse plutonic quartz in southeast Australia disintegrated rapidly during fluvial transport.
Biological origin	Wilding et al. (1977)	Biogenic opal is a minor but ubiquitous component of soils, ranging from < 0.1 to 3% by dry weight.
Salt weathering	Goudie et al. (1979)	Rectangular blocks of York Stone subjected to simulated capillary rise using a variety of salt solutions and in debris produced after 60 cycles, silt comprised an average of 43.7% and clay 3.5%.
Aeolian abrasion	Whalley et al. (1982)	Simple aeolian abrasion experiments revealed that chips knocked off during abrasion are predominantly of silt size and rather blocky in form.
Chemical weathering	Pye (1983b)	The disintegration of quartz can occur by a simple dissolution of silica along lines of crystal weakness in podzol profiles.
Clay pellet aggregation	Dare-Edwards (1984)	Larger clay pellets normally accumulate as low dunes (lunettes) close to the source, but finer pellets can be dispersed more widely.

2.5.2 Loess Distribution

Pye (1984) proposed a loess global geographical map, which indicated its occurrence in North America, South America, Europe and Asia, with the notable exception of Africa. Pecsi (1990) later developed another map (Figure 2-10) that exhibited the loess distribution around the world, including in North Africa, and concluded that these sediments form on plateaus, pediments, plains, and major river basins. Based on this map, only loess derivates (that is, secondary or reworked loess; refer to Table 2-2) and loess-like deposits occur in Africa. The prevalence of loessal deposits in Southern Africa (Namibia) was reported by Crouvi et al. (2010). This makes it imperative to explore the possibility of loess occurrence in other African countries.

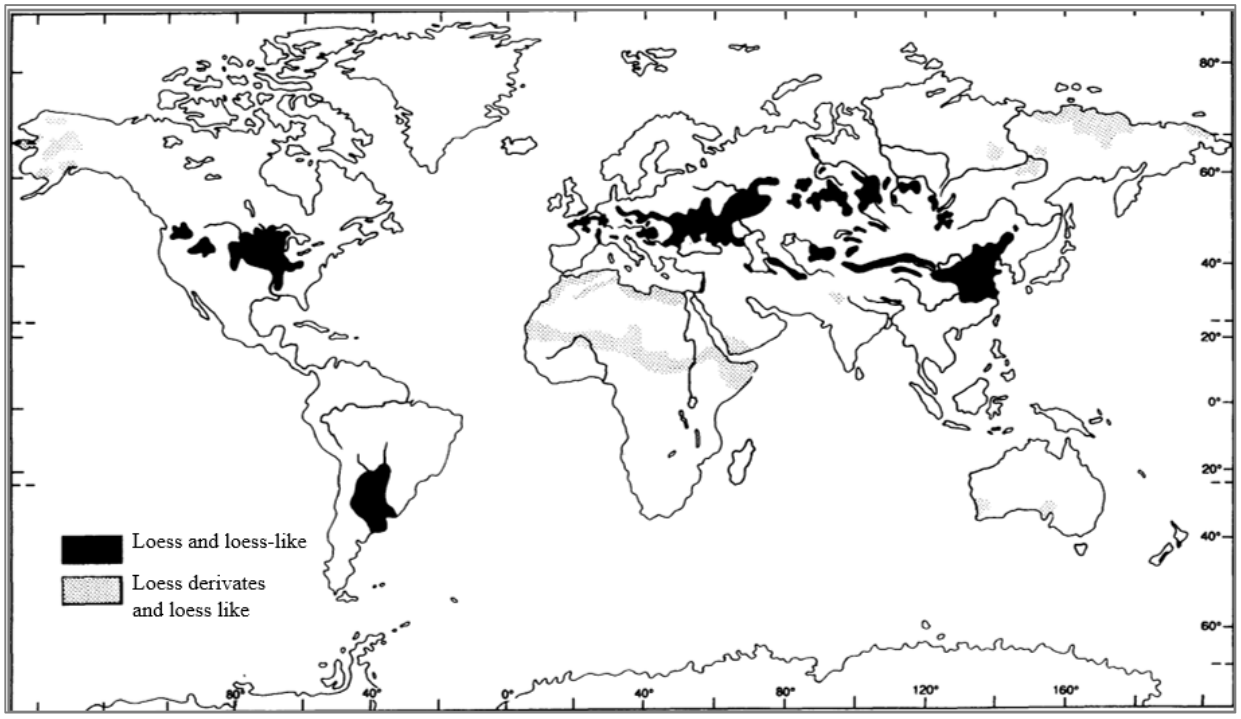

Figure 2-10, Global geographical distribution of loess and loess-like deposits (Source: Pecsi, 1990)

2.5.3 Loess Mineralogy and Structure

Aggregates in soil mass are made up of naturally occurring minerals; Osipov & Sokolov (1994) estimated over 50 traces in loess deposits. Soil grains are chemically and physically different depending on the mineralogical composition of the parent material and the environmental conditions that prevailed during their formation. In arid regions, loess formed frequently has more illite, chlorite, smectite and sepiolite, while kaolinite prevails in humid zone loess (Pye, 1984). These minerals and corresponding structural arrangement are essential determinative factors for soil properties such as volume change.

Table 2-4 presents the common minerals in loess, based on literature from various parts of the world. Quartz and feldspar are the most predominant minerals, followed by mica. Other minerals such as clay, carbonates and salts also occur, but in comparably smaller amounts.

Table 2-4, Typical minerals in loess deposits (Source: compiled from various literatures)

Location	Minerals	Reference
South Island	70 to 80 % of quartz and feldspar in proportions that are approximately equal; mica and chlorite amount to 7 % and other minerals are minor.	Raeside, 1964
General estimation	Carbonates (0.2 to 30 %), sulfates (gypsum 0.0 to 3 %), salt (0.0 to 2 %), quartz (20 to 85 %), feldspar (4 to 40 %) and mica (1 to 30 %), with various clay minerals.	Egri (1972)
General estimation	Quartz is predominant (40 to 80 %), feldspar has subordinate content, carbonates range from 1 to 20 % and clay minerals are from 5 to 20 %.	Pecsi (1990)
General estimation	Quartz, feldspar, mica, gypsum, carbonates, hydromica, kaolinite, montmorillonite; 4 to 10 % medium soluble mineral (gypsum); less than 2 % readily soluble salt (chlorides); less than 2.4 % half-soluble oxides and hydroxides.	Osipov and Sokolov, 1994
Algeria	Feldspar is dominant	Nouaouria et al, 2008
China	Quartz (29.6 to 38.5 %), feldspar (13 to 21.9 %), mica (8.7 to 20 %), expandable phyllosilicates (2.1 to 28.1%), kaolinite (0.6 to 3.7 %), chlorite (0.3 to 4.7 %), calcite (0.3 to 23.9 %), dolomite (0.5 to 3.1 %), amphibole (0.8 to 2.8%), hematite (0.4 to 1.0 %), goethite (0.9 to 2.3 %) and gypsum (0 to 1.4 %).	Jeong et al, 2011
The Rio Grande do Sul, Brazil	Quartz and plagioclase feldspar are coarser minerals; clay minerals comprised of illite, smectite, interstratified illite/smectite and kaolinite.	Lopes et al., 2016

Table 2-4 shows that loess consists of minerals that remain physically and chemically unchanged during saturation (quartz, feldspar and mica), water-soluble (carbonates and salts), and those that lose shear strength when saturated (clays). Minerals that remain unaltered are referred to as passive, while others are termed active (Egri, 1972). In loess structure, inactive minerals form the core, which is bonded by the active component (Figure 2-11). These bonds occupy the interparticle space to create an open fabric that becomes collapsible when loaded and wetted.

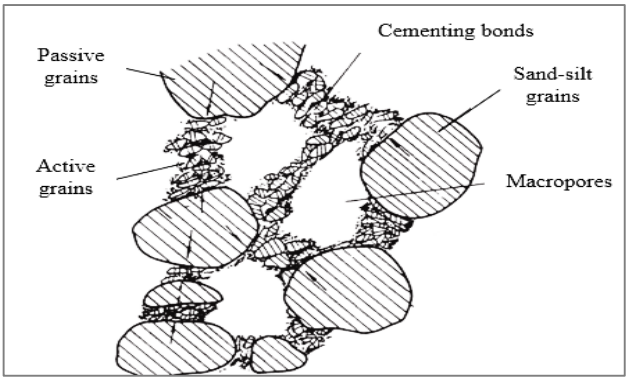

Figure 2-11, A structure of collapsible Loess (Source: Kie, 1986)

Various cementations formed in collapsible soils include capillary tension, silts and clay aggregates (Figure 2-12). Other cementing minerals are calcium carbonate, hydrous calcium sulfate, secondary zeolite, secondary mica, strong soluble salts, ferrous oxide and hydroxide (Yang, 1989). Binding oxides and hydroxides include goethite, hematite, and gibbsite (Karathanasis, 2009; Gao, 1996). These minerals cohabit with clay bonds and contribute to the rigidity of unsaturated loess. According to Knodel (1992), in the case of capillary forces, strength is quickly lost during collapse, while it is slow in chemical bonds and much slower in clay buttress type of bonding.

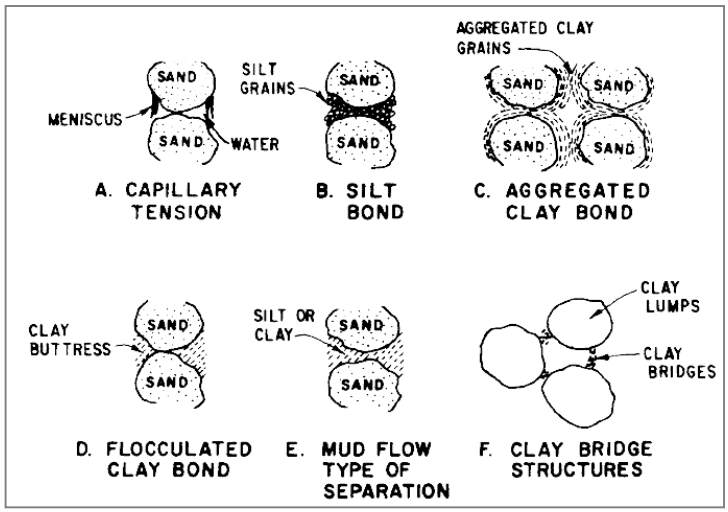

Figure 2-12, Bonding of primary minerals by active minerals in collapsible soils (Source: Rogers, 1995)

Aggregations of clay minerals provide major bonding for the larger grains in loess, and collapse is influenced by their ability to absorb water (Lobdell, 1981; Assallay, 2001). For this reason, a consideration of the clay minerals and respective water affinity is imperative in understanding the behaviour of saturated loess.

Clay minerals

According to Grim (1953), all the clay minerals are made from two main building blocks or structural units. The first block consists of a silicon equidistant from four atoms of oxygen, or hydroxyls arranged in the form of a tetrahedral. The second structural block is an octahedral comprising of aluminium atom at intermediate from six oxygen atoms or hydroxyls. These units join with others to form structural sheets, as shown in Figure 2-13 (Craig & Knappett, 2012). Kaolinite mineral (Figure 2-13 a) consists of one tetrahedral sheet and one octahedral sheet, at a ratio of 1:1. The combined sheets are joined by strong hydrogen bonds in the interlayers, making it hard for water to penetrate. The mineral is also chemically stable, with a limited isomorphous substitution (that is, the substitution of silicon and aluminium by other atoms resulting in imbalance).

Illite (Figure 2-13 b) is composed of 2 tetrahedral sheets and one octahedral sheet between them, at a ratio of 2:1. There is a limited switch of silicon by aluminium in the silica sheet and the

combined sheets are linked by weak bonding due to non-exchangeable potassium ions (Grim, 1953). The basic structure of montmorillonite (Figure 2-13 c) is similar to that of illite, with the only difference being that the interlayer of the combined sheets has exchangeable cations and water. The high susceptibility of montmorillonite to isomorphous substitution makes it the most active clay mineral (Fredlund, 1975).

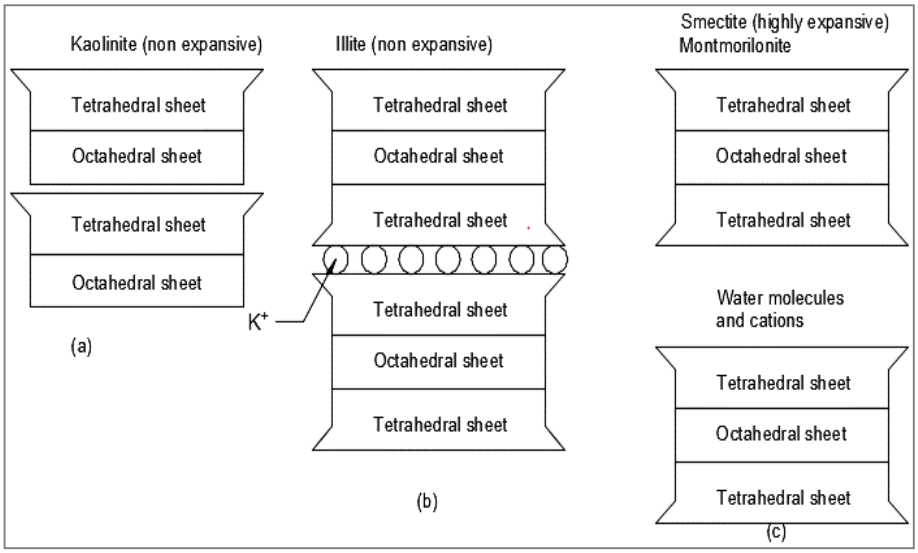

Figure 2-13, Clay minerals (Source: Craig & Knappett, 2012)

Clay particles are negatively charged due to the isomorphous substitution, and attraction forces exist between them and water. Furthermore, electric moments in soil molecules develop hydrogen bonds and Van der Walls forces (cohesive forces) that flocculate particles (Punmia et al., 2005). Figure 2-14 illustrates some attractive forces recognised by Lambe (1953) who conducted an intensive study on the interparticle forces. It is noted that grains are aggregated around water by water-dipole linkages, cations and dipole cation-dipole. The resulting clay aggregations act as connectors between larger sized-soil grains (sand and silt).

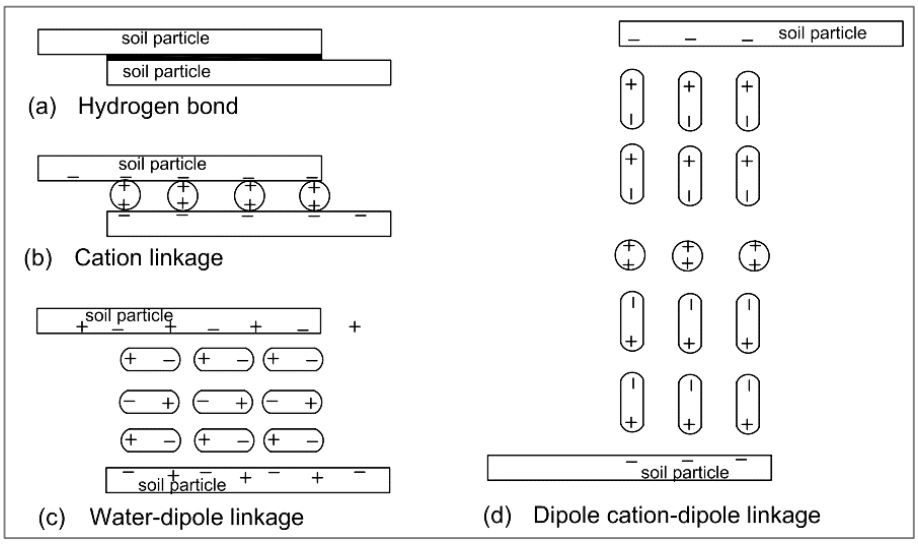

Figure 2-14, The attraction interparticle forces in soil (Source: Lambe, 1953)

2.6 Typical Physical Characteristics of Loessal Deposits

Knowledge of founding soil properties and behaviour is highly essential in designing durable civil engineering structures. Mostly, soil is identified through a visual inspection of its structure, colour, deposition pattern and textural feel (Guidelines for Soil and Rock Logging in South Africa, 2002). Loess deposits may be homogenous, calcareous silt, clayey or sandy silt, buff in colour, white, red, dark grey, brown or yellow (Pye, 1987). A loess thickness ranging from 1.83 to 7.62 m was reported in Vanderburgh, Indiana (Howayek et al., 2012). Conversely, over 300 m thick loess blankets were reported in China (Zhu et al., 2018). This shows that its thickness could be depending on the distance of the deposition basin from the soil source. Another unique feature is formation of the subsurface pipes or fissures as an indication of high erodibility (Bíl & Kubeèek, 2012). However, for construction projects, visual examination is not enough to predict the behaviour of the founding soil. Soil tests (that is, field and laboratory tests) are, therefore, conducted to determine soil classification, strength, volume change and other engineering properties.

2.6.1 Soil Size Distribution

Soil size particle distribution is determined by sieve and sedimentation analysis. Sheeler (1968) reported gradation envelops of loess in the United States of America (Figure 2-15). It was observed that it consisted of clayey loess, sandy loess and silty loess zones. Loess with clay and sand composition less than 20 % is regarded as silty loess; however, when either of these particles is more than 20 %, the soil is considered as clayey or sandy loess, respectively (Pye, 1987). Nevertheless, loess predominantly consists of silt particles ranging from 50 to 70 % by weight (Assallay, 2001; Nouaouria et al., 2008).

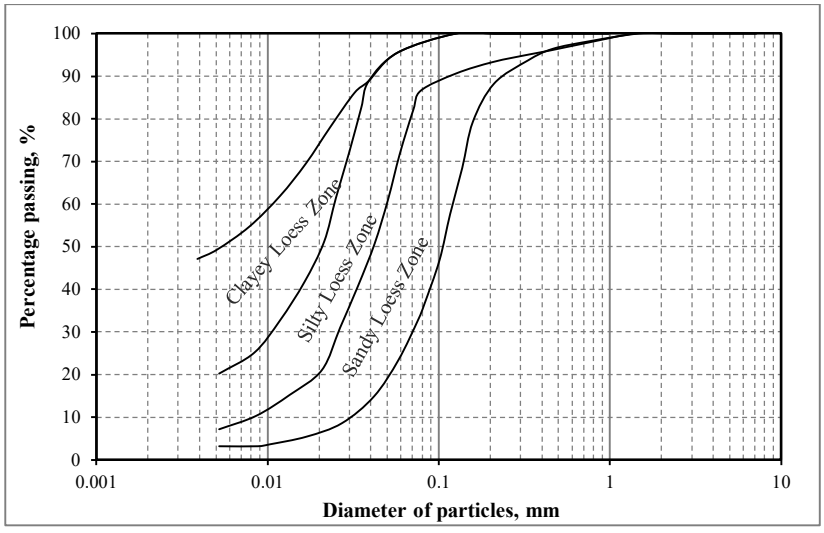

Figure 2-15, Particle size gradation curves for loess in the United States of America (Source: Sheeler, 1968)

Howayek et al., (2012) also compiled grain grading curves from literature (Figure 2-16). The established particle distribution pattern was similar to that presented in Figure 2-15. Furthermore,

it was noted that the maximum clay content in loess was approximately 40 % and a minimum value was around 1 % by weight.

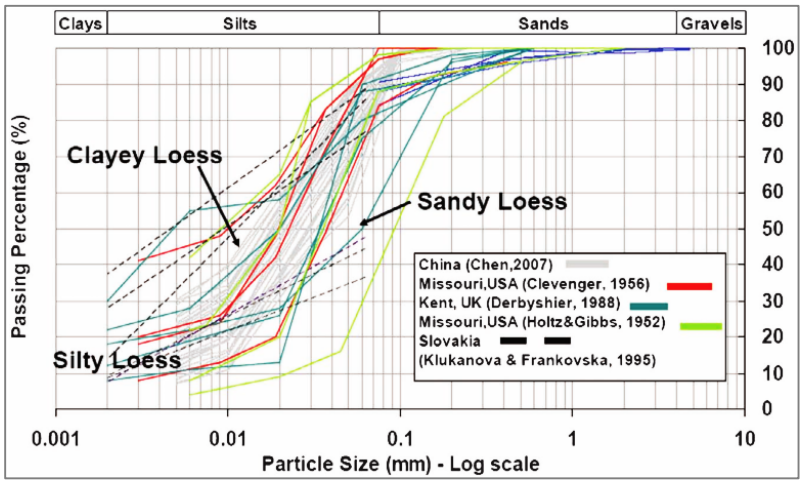

Figure 2-16, Particle size gradation (Source: Howayek et al., 2012)

2.6.2 The Consistency of Soil

Atterberg divided the behaviour of soil finer than 0.425 mm into solid, semi-solid, plastic and liquid states, in terms of moisture content measured at their boundaries (South African Pavement Engineering Manual, 2013). The minimum moisture content at which a solid soil transforms to semisolid is termed 'shrinkage limit', while it is referred to as 'plastic limit' when the soil changes from a semi-solid to a plastic state. The minimum moisture content at which the soil starts to flow is the 'liquid limit'. The difference between liquid and plastic limits indicates soil plasticity. This parameter is used along with the clay fraction to predict possible soil volume increase (Figure 2-17). Holtz & Gibbs (1956) also provided a quick soil swell potential, based on the Atterberg limits (Table 2-5).

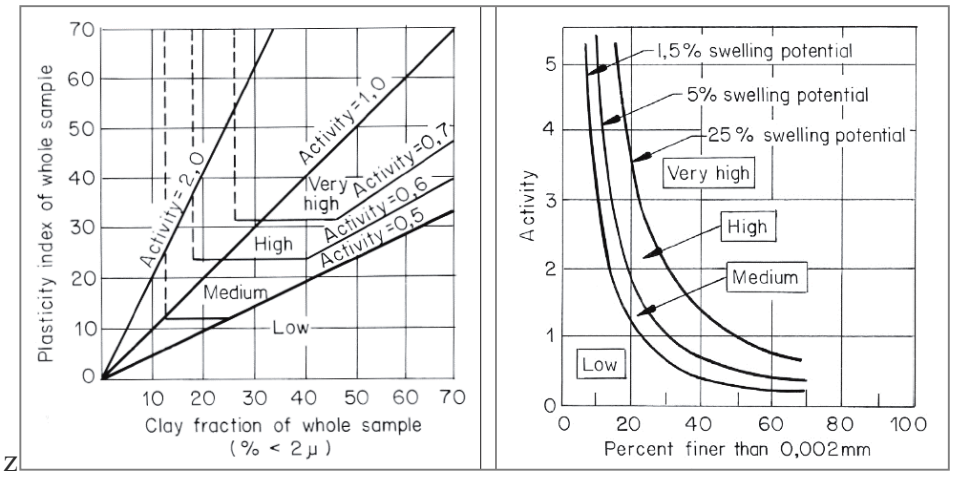

Figure 2-17, Activity of expansive soils given by Donaldson & Williams, 1973 and Seed, 1978. (Source: Byrne & Berry, 2008)

Table 2-5, Classification of soil potential based on Atterberg limits as per Holtz & Gibbs, 1956 (Source: Lucian, 2006)

Classification of potential swell	Liquid limit (LL), %	Plasticity index (PI), %	Shrinkage limit (SL), %
Low	20 – 35	< 18	> 15
Medium	35 – 50	15 – 28	10 – 15
High	50 – 70	25 – 41	7 – 12
Very high	> 70	> 35	< 11

Delage et al. (2005) reported a liquid limit (LL) ranging from 26 to 30 %, and plastic limit (PL) from 20 to 22 % in loess deposits from Northern France. This soil constituted kaolinite and illite-smectite as its clay minerals. Consistency limits are influenced by the type of clay mineral present in a soil mass; montmorillonite (with its high activity) has the highest PI. (Dijkstra et al., 1994) also observed a LL from 27 to 31 % and a PL of 16.6 to 17.8 % in North Central China. Nouaouri et al. (2008) reported the LL that rangeed from 30 to 33 %, and a PL from 22 to 23 % in loess of Algeria.

Figure 2-18 demonstrates plasticity index values reported in loessal soils from the literature. Based on this, the average liquid limit is 27.8 % and plastic limit is 19.44 %. However, these limits are only confined to the referenced literature and are inclined to change based on the clay minerals present in the soil.

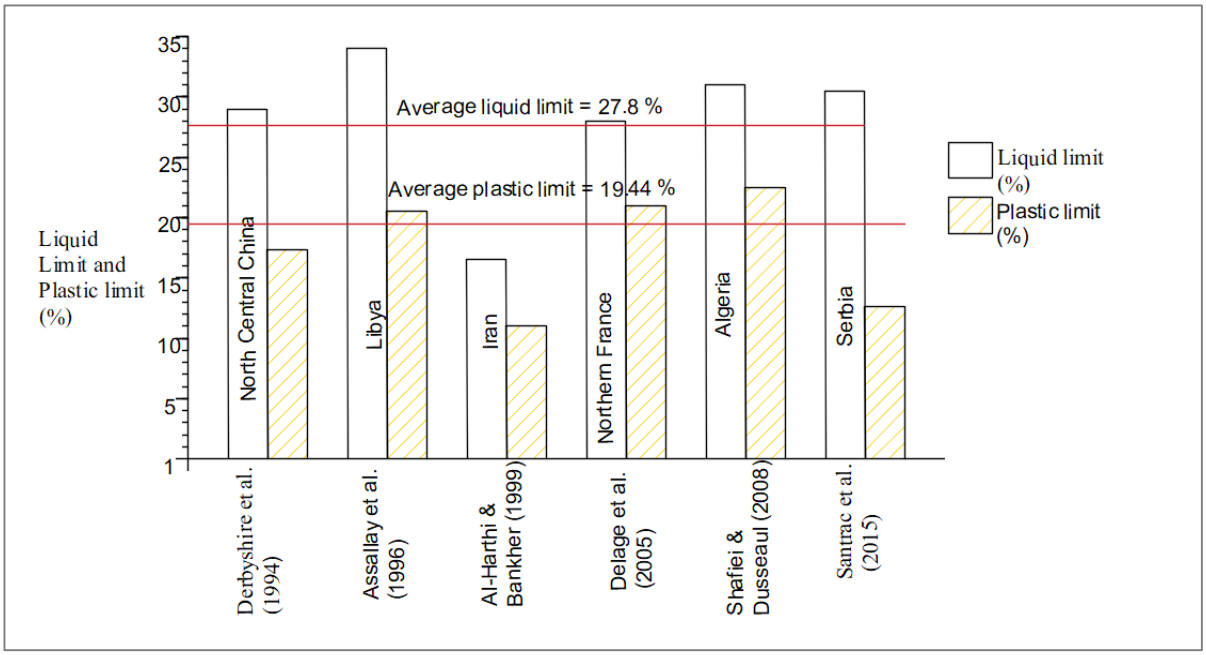

Figure 2-18, Plasticity index values in loess (Source: compiled from the literature)

2.6.3 Density

Soil density is a ratio of soil mass to the volume it occupies, and is generally used as a measure of particle packing or denseness. Shafiei & Dusseault (2015) reported densities that varied from

1270 to 1540 kg/m^3 in sandy loess of Iran. Nouaouri et al. (2008) established values from 1420 to 1430 kg/m^3 on silty loess in Algeria. Anagnosti (1973) reported densities from 1300 to 1800 kg/m^3 in Libya. In loess like sediments, Klukanova & Frankovska (1995) indicated densities from 1230 to 1700 kg/m^3, Al-Harthi & Bankher (1999) later established values varying from 980 to 1500 kg/m^3 in loess like deposits in western Saudi Arabia. Figure 2-19 presents the densities in loessal sediments from around the world with an average value of 1500 kg/m^3.

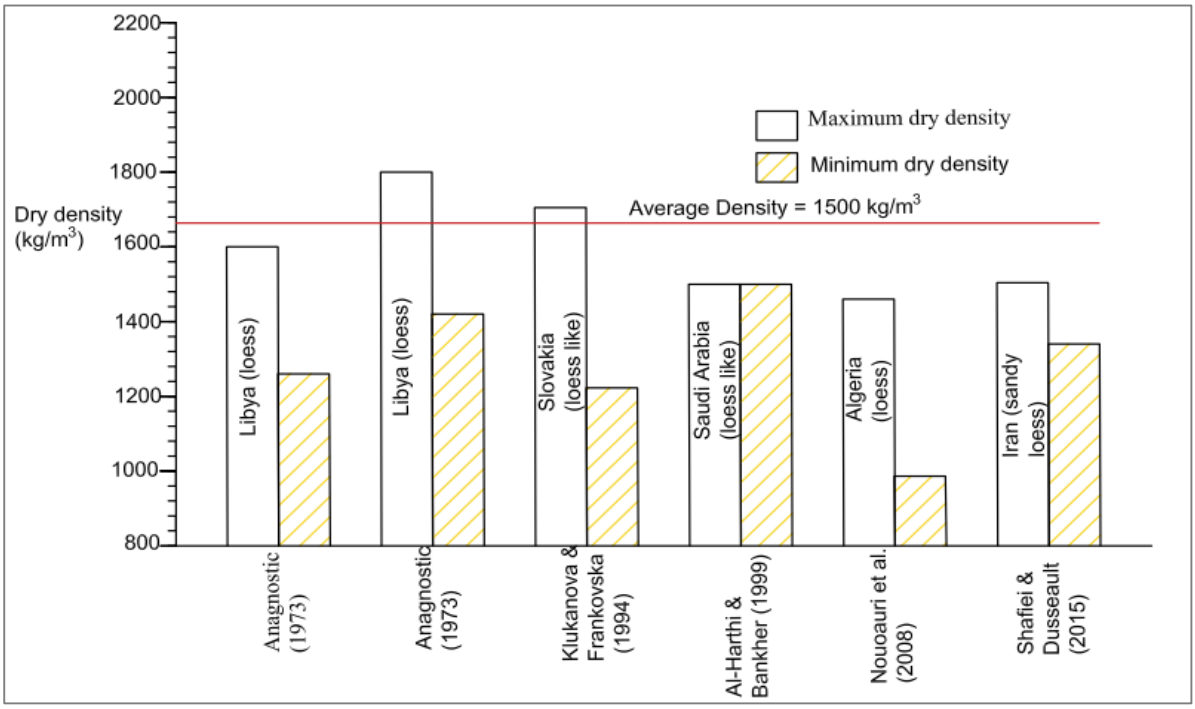

Figure 2-19, Density values in loess (Source: compiled from the literature)

2.6.4 Specific Gravity (Gs)

Specific gravity (Gs) is a ratio of soil mass to that of water at an equivalent volume and specific temperature (Craig & Knappett, 2012). This property is a critical parameter in the analysis of hydrometer test results and void ratio calculation in the oedometer consolidation test. In Libya, a silty loess with a Gs of 2.68 to 2.73 g/cm^3 and sandy loess with Gs from 2.66 to 2.67 g/cm^3 were reported by Assallay et al. (1994). Al-Harthi and Bankher (1999) noted a minimum specific gravity of 2.49 g/cm^3 and a maximum of 2.76 g/cm^3 in loess like-soils in western Saudi Arabia. In Iran, a loess with a Gs reaching 2.67 g/cm^3 was reported by Dusseault and Shafiei (2008). Figure 2-20 demonstrates the specific gravity in loess from different parts of the world, with an average value of 2.686 g/cm^3.

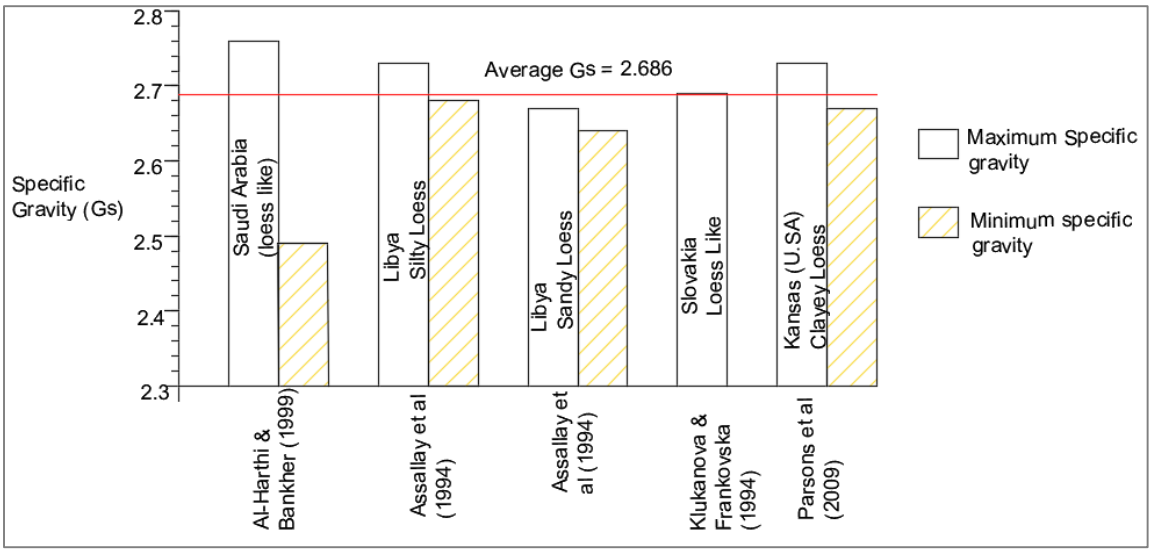

Figure 2-20, Specific gravity in different types of loess (Source: compiled from the literature)

2.6.5 Shear Strength

Shear strength, τ, is the ability of soil to resist shear stresses generated by applied loads. Components contributing to shearing resistance are particle interlocking, frictional resistance among individual soil grains and cohesion (Punmia et al., 2005). Essentially, the parameters contributing to shear strength are determined from Mohr's failure envelope (Figure 2-21). This envelope is a common tangent to Mohr's circles, drawn from peak stresses produced from different confining pressures in shear tests. The intercept of the envelope indicates soil cohesion, c, while the slope gives the friction angle, $\emptyset$.

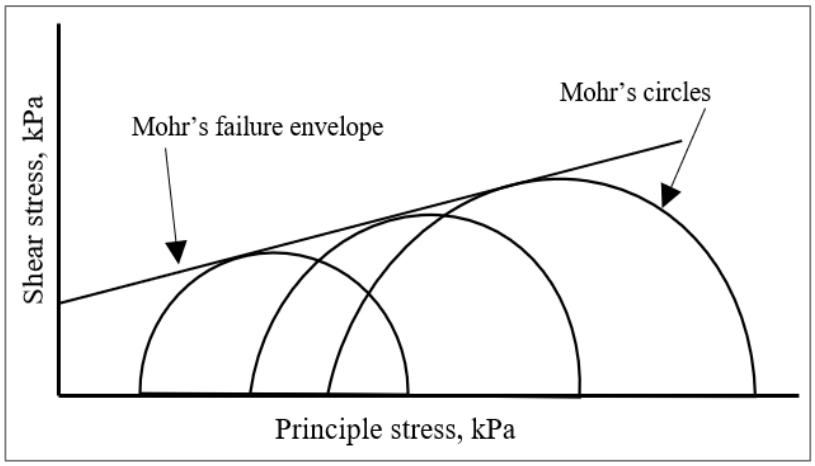

Figure 2-21, Typical Mohr's circles and failure envelope for shear strength determination

The shear strength due to a normal stress applied to soil, σ, is computed from Coulomb equation (Equation 2-3).

$$\tau = c + \sigma \tan\emptyset \qquad \textbf{Equation 2-3}$$

Li et al. (2014) investigated shear strength properties of loess in China with variation in water percentages (Figure 2-22). More strength was established at low water content (5 %) than at higher moisture (15 %). Furthermore, at a moisture content of 5 %, deviator stress formed pronounced peaks that approached residual stress with an increase in strain. Conversely, at higher moisture, under the same strain and test conditions, smooth curves were formed with drastically reduced deviator stress. This behaviour could be ascribed to the augmented pore pressures and spaces between individual soil particles, which reduced dilatancy during shearing.

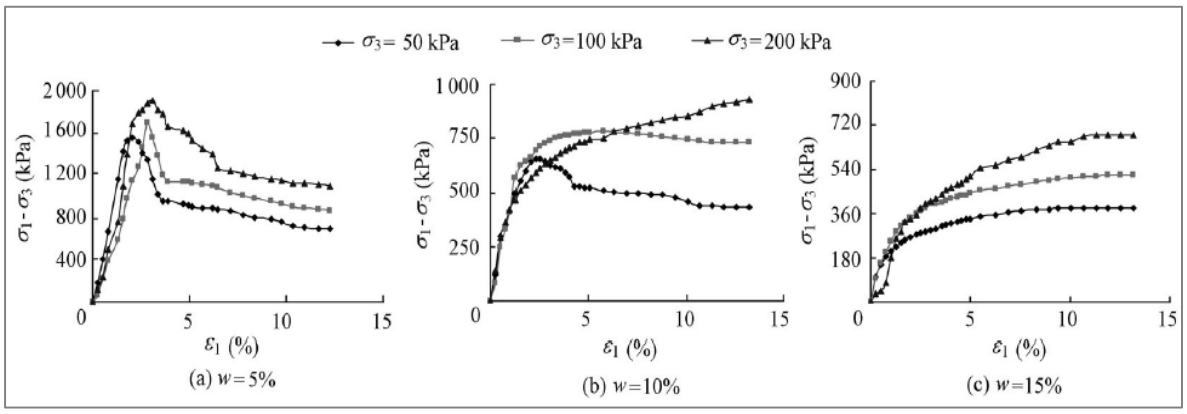

Figure 2-22, Triaxial shear stress-strain curves of reconstituted loess with variation in moisture contents (Source: Li et al., 2014)

Derbyshire et al. (1994) revealed a gradual increase in cohesion up to 20 kPa when moisture was raised from 0 to ±22 % in Malan silty loess. This threshold was also equivalent to the approximate plastic limit of the tested samples. Beyond this moisture content, a sudden decrease to 0 kPa was observed. A maximum friction angle of ± 38.7° occurred at moisture values from 5 to 7 %, and it was reduced at higher moisture content (Derbyshire et al., 1994). This change in shear strength parameters was associated with enlargement of the distance between soil grains by the increased pore water pressure. A study conducted by Sobhee-Beetul & Kalumba (2015) on clay of low plasticity, forms a good congruence to this observation. A friction angle of 0°, as well as a negligible cohesion, were observed in a clay of low plasticity when it was sheared at 1 and 1.2 times its liquid limit (Sobhee-Beetul & Kalumba, 2015).

2.6.6 Hydrocollapse Mechanism

A process in which water content of a saturated soil is reduced without substituting it by air is termed consolidation (Terzaghi, 1943). This causes a reduction in the void ratio and an increase in the settlement of the soil. Conversely, in hydroconsolidation/hydrocollapse, subsidence is brought by a change in bonds contacts (Rogers et al. 1994). An alteration of the cementing material compromises the stability of the primary grains and the soil structure undergoes a measurable volume decrease to regain it (Darwell & Denness, 1976). The mechanism of volume change of a loaded soil before and after soaking is illustrated in Figure 2-23. It is observed that cementing clay aggregates are consolidated by concentrated pressure before soaking, but the soil

structure remained intact. Contrarily, bonding clay collapsed along with core grains on soaking, and this resulted in an overall reduction in soil volume (that is, the soil settled).

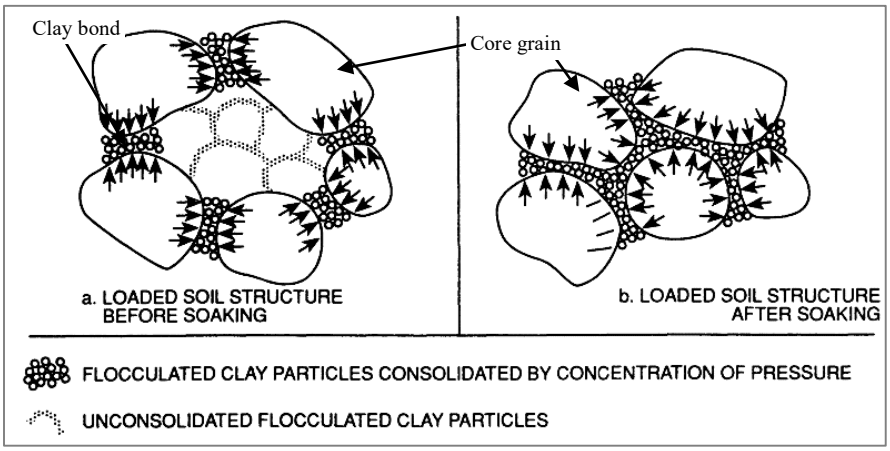

Figure 2-23, Structure of a collapsible soil (Source: Rogers, 1994)

The susceptibility of soil to collapse is normally estimated from one-dimensional oedometer tests. Lutenegger & Hallberg (1988) established a collapse coefficient, *i*, in loess deposits, which indicates collapse problems when it is greater than 0.02. This coefficient is determined from the oedometer test results (Equation 2-4).

$$i = \frac{\Delta e}{1+ e_1} \qquad \textbf{Equation 2-4}$$

Where, Δe is a change in void ratio caused by wetting, e_1 is a void ratio prior to wetting at an effective stress of 300 kPa.

The method recommended by the American Standard Test Methods (ASTM- D5333 – 03) is slightly different from the foregoing procedure. The collapse potential, I_c, is determined from Equation 2-5.

$$I_c = \frac{\Delta e}{1+ e_o} \times 100 \qquad \textbf{Equation 2-5}$$

Or

$$I_c = \frac{\Delta h}{h_o} \times 100 \qquad \textbf{Equation 2-6}$$

Where Δe is the change in void ratio caused by wetting, e_o is the initial void ratio, Δh is the change in height caused by inundation and h_o is the original height. When soil settlement, *S*, is to be determined, Equation 2-6 is multiplied by a ratio of a soil layer thickness, *H*, and 100 as indicated in Equation 2-7.

$$S = \frac{\Delta h}{h_o} \times 100 \times \frac{H}{100} \qquad \textbf{Equation 2-7}$$

This method can be used to determine collapse at any applied effective stress. However, the severity of the potential soil collapse is decided based on change in void ratio at the applied stress of 200 kPa (Table 2-6).

Table 2-6, Classification of collapse index (Source: D 5333 – 03)

Degree of collapse	Collapse index I_e, %
None	0
Slight	0.1 – 0.6
Moderate	2.1 – 6.0
Moderately severe	6.1 – 10.0
Severe	> 10

The magnitude of hydrocollapse is affected by the initial physical properties of soil and environmental conditions. These factors include dry density, moisture content, bond material and respective quantity, soil fabric and level of applied stress (Assallay, 2001). Basma (1992) confirmed that high initial density resulted in less settlement when the soil was inundated. This was related to the closely-packed particles, with a small spacing for further rearrangement. Contrarily, low density and large macropores provide enough room for grain repacking and collapse.

Clay mineralogy and its corresponding percentage content are important to predict the probable degree of hydrocollapse in loess. Minerals with active isomorphous substitution, such as montmorillonites, absorb water when inundated and increase in volume. Conversely, kaolinite is stable and only demonstrate minimal expansion. The swell in expansive minerals reduces the possibility of settlement in saturated loess while this is not the case in less active clays. This was confirmed by a study undertaken by Assallay (2001) in which a higher collapse was reported when kaolinite was used as a binder than in bentonite with higher expansiveness. Moreover, water acts as a lubricant between soil particles and its increase will accordingly reduce frictional resistance between soil grains. In this state, core particles are rearranged into a less volumetric denser packing.

To provide a clear demonstration that collapsibility varies as a function of clay content on loess, Assallay (2001) has reviewed previous literature that focused on the same topic. From this discussion, a synthesis was herein evoked to show the variation of loess collapsibility with a change in the amount of clay (Figure 2-25). It is noted that at a clay content of less than 5 % by weight, the collapsibility is little. When the content is between 5 and 10 %, a moderate to high collapse occurs. At a percentage ranging from 10 to 12 %, a maximum subsidence is probable, and a moderate value takes place when it increases from 13 to 30 %. Due to the formation of an undivided clay phase, which seals the pores of a soil fabric at higher clay values (>30 %), the soil is safe against collapse (Rogers et al., 1994). However, Assalay (2001) reported a maximum collapse in clay content of 40 % at a high pressure (≥400 kPa). This shows that the magnitude of the applied stress is also important.

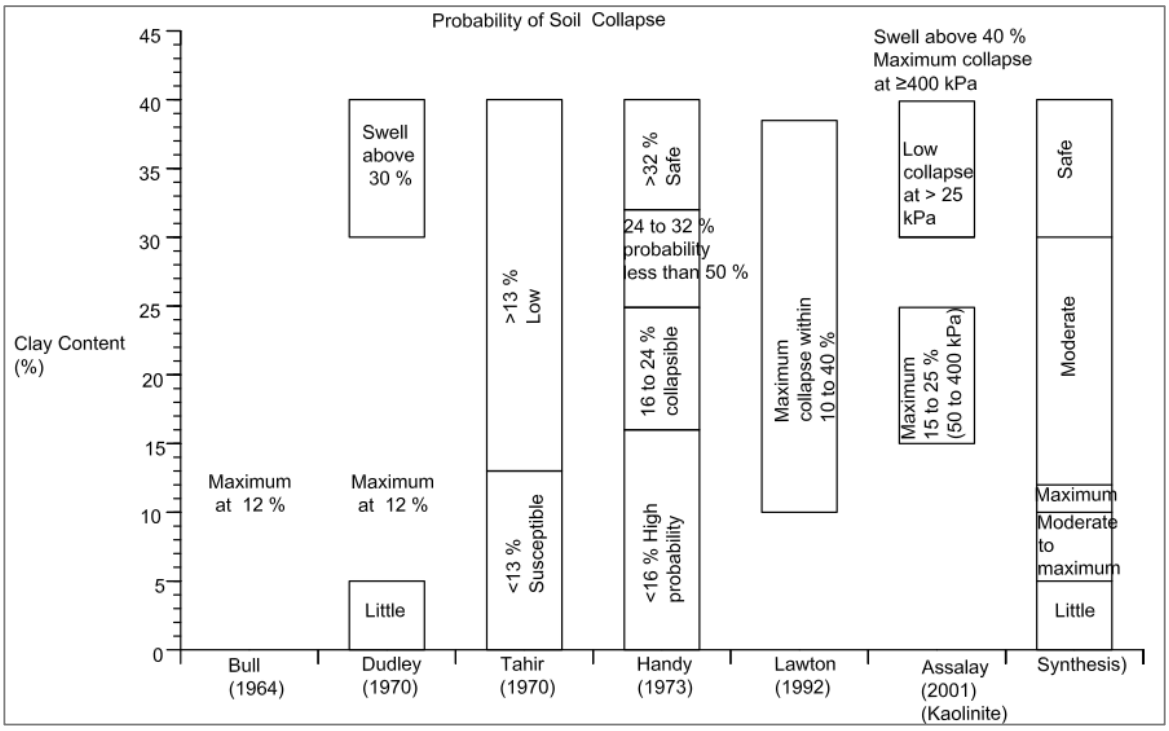

Figure 2-25, Probability of soil collapse based on the variation of clay content (Source: compiled from Assallay, 2001)

Like clay content, the carbonate amount is important in the collapsibility of loess. Bonds are in short range in smaller quantities of carbonates, thus causing a rapid and high shear strength drop during deformation (Rogers et al., 1994). Contrarily, a minor decrease occurs in larger quantities with long-range bonds that fill soil pores and produce wide-scale cementation (Rogers et al., 1994). This theory is important in understanding soil collapsibility, but the actual influence of large-scale cementation to carbonate dissolution is not explained. However, relating it to prolonged partial infiltration and the consequential reduced dissolution in higher quantities is a rather adequate concept. In low carbonate content, water easily permeates through soil pores causing enough leaching; nonetheless, in larger values, continuous carbonate bonds inhibit infiltration and water only moves to the interior after dissolving the exterior carbonates. The reduced dissolution rate will consequently decrease hydroconsolidation and the total collapse will depend on an inundation period.

The permeability leaching tests on gypseous soil were conducted for approximately 300 hours, and findings indicated the presence of dissolved gypsum in leachate water (Karkush et al, 2008). This shows that the presence of gypsum in loess enhances collapse due to high solubility. Furthermore, strong soluble salts also exacerbate the hydroconsolidation process. Nevertheless, a mineralogy analysis carried by Yang 1988, revealed that their contribution is unimportant since they exist as accessory minerals with content less than 0.1 % in loess.

All these factors in loess deposits make it susceptible to volume change which is detrimental to the structures. It is, therefore, necessary to identify loess and design foundations to withstand the movements without causing damage to masonry.

2.7 Review of Hydrocollapse Settlement Problems

Several literatures have documented settlement problems induced by loess hydrocollapse on structures (Grigoryan, 1991; Djogo & Milović, 2013; Yuan-Xun et al., 2013; Santrač et al., 2015). Grigoryan (1991) recorded a settlement of 800 mm and a tilt of 0.009° within a period of 10 months on two 9-story buildings in Volgodonsk, Russia. They were founded on reinforced concrete strips on 12 m thick collapsible loess; nonetheless, compaction was conducted only up to a depth of 3 m. Therefore, inundation from a leaking water pipe and subsequent settlement of deeper loess weakened the rest of the founding layer (Grigoryan, 1991). Due to the footing reinforcement, the structural components remained intact during settlement. However, an increase in tilting compromised the serviceability of the building and occupants had to be evacuated within a working life of seven years.

Djogo & Milović (2013) also reported settlement in twenty 12-story buildings on strip footings in Belgrade, Serbia, which was caused by loess hydrocollaspe. The thickness of the loessal deposits was over 20 m and the foundations penetrated to a depth of 2 m. Out of the twenty buildings, 5 had a settlement higher than the estimated values reaching a maximum of 550 mm. Buildings with differential settlement showed severe damage, while others remained intact. It was established that the predicted design settlement was based on the measured natural moisture content, which was later changed by intense rainfall. This uneven collapse also broke water pipes, which intensified the problem. It is ascertained from this report that any design against collapse should be in accordance with critical moisture, and not measured field water content. Figure 2-26 portrays non-uniform settlement in the four corners of one of the damaged houses. It is noted that the highest volume decrease occurred in the fourth year after construction.

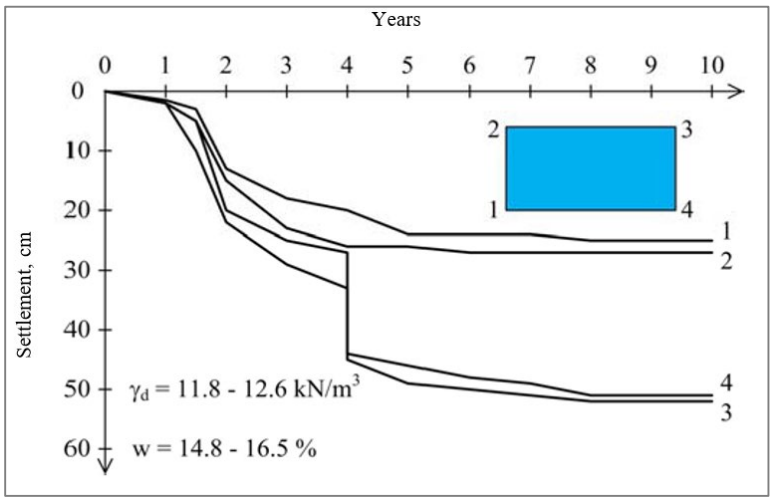

Figure 2-26, Hydrocollapse differential settlement on various corners of a building (Source: Djogo & Milović, 2013)

Yuan-Xun et al. (2013) provided a failure description of a 4-story house constructed at 2.5 m depth on loessal sediments in Fengxiang Shaanxi, China. Damage in the form of fissures was observed on the walls and aprons in just one year after construction. A repair implementation was immediately undertaken without any investigation of the source of the problem and the failure reoccurred. A spot examination conducted later, revealed inadequately compacted founding soil and ruptured subsurface water pipes (Figure 2-27). Both discrepancies triggered subsidence to a maximum value of 373 mm (Yuan-Xun et al., 2013). Yuan-Xun et al (2013) made it clear that the pipes were broken as a result of prior settlement, and their leakage exacerbated the severity of the problem. Furthermore, cracks formed on the apron also provided a passageway for infiltrating rainwater.

The site was located adjacent to Fengxiang Mountain on the Mesa slope, and a seasonal river also existed in the area (Yuan-Xun et al., 2013). Yuan-Xun et al. (2013) reported that the foundation was constructed on lime-treated soil of 2.5 m thickness, which was overlain by a 2.5 m thick fill. Below these, stratified layers including more than 6 m of loessal sediments were overlaying the cobles.

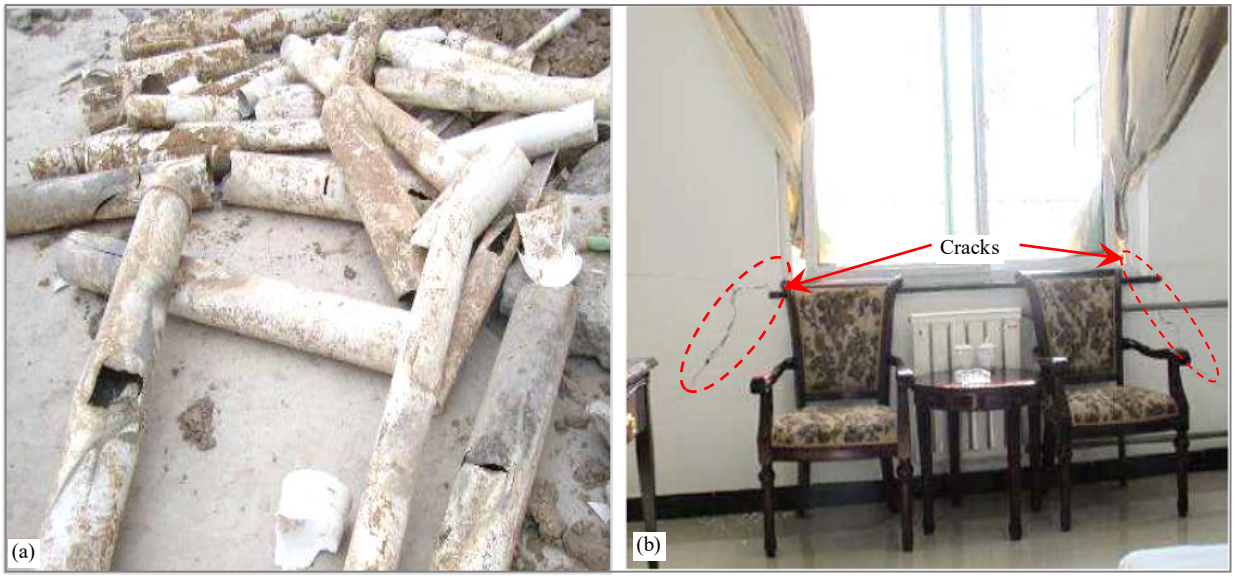

Figure 2-27, Hydrocollapse settlement triggered by heavy rainfall: (a) ruptured water pipes and (b) cracks below the window (Source: Yuan-xun et al., 2013)

During the construction stage of a silo in Feketić, Serbia, an intense rainfall partially saturated supporting soil and led to a sudden maximum differential subsidence of 239 mm with a minimum of 125 mm (Santrač et al., 2015). The investigation revealed that cracks (formed in the soil due to shrinkage) also provided the ingress of water. For this structure, settlement related damage was minimised by the reinforcement in the raft footing.

This site was situated on a plain terrain at altitude varying from 99.78 to 101.20 m on the 12 m thick layer of loess deposits. It was also established that this stratum was underlaid by medium

dense to dense, fine-grained sand (Santrač et al., 2015). Figure 2-28 depicts a flooded foundation pit and varying settlement at corners, respectively.

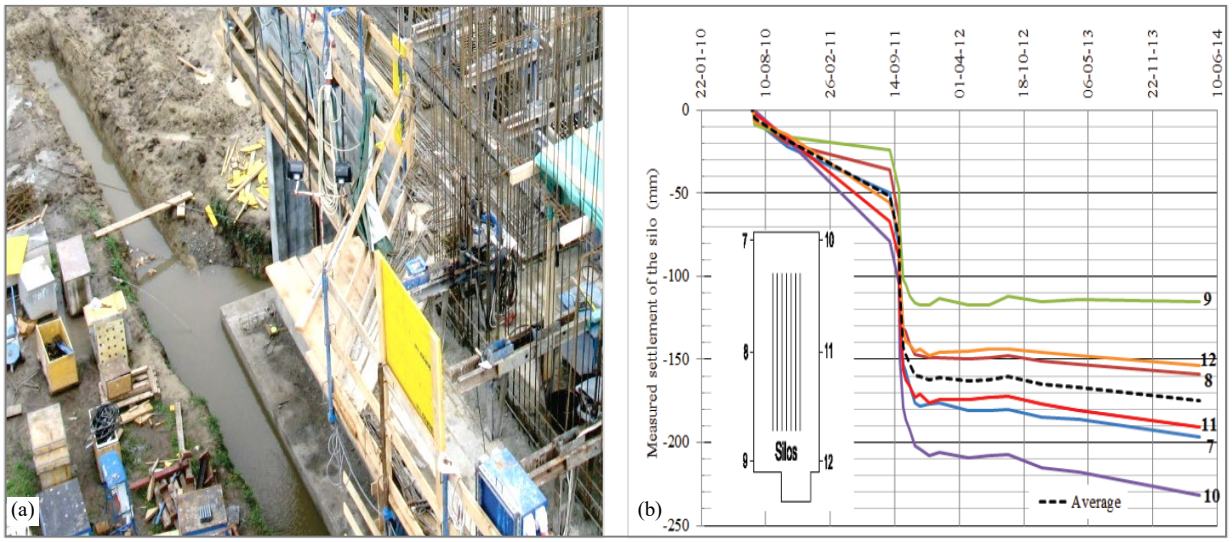

Figure 2-28, Hydrocollapse settlement triggered by heavy rainfall: (a) A flooded foundation pit and (b) Measured differential settlement at different corners of silos (Source: Santrač et al., 2015)

Kalpakci (2017) documented a settlement of up to 120 mm and a tilt of 4° during the construction of a cement plant in Azerbaijan (Figure 2-29). These movements resulted in formation of vertical cracks in concrete foundations. The settlement was monitored, and the maximum collapse triggered by rainfall was recorded within 20 months of construction. The plant was erected on 16 m long friction piles.

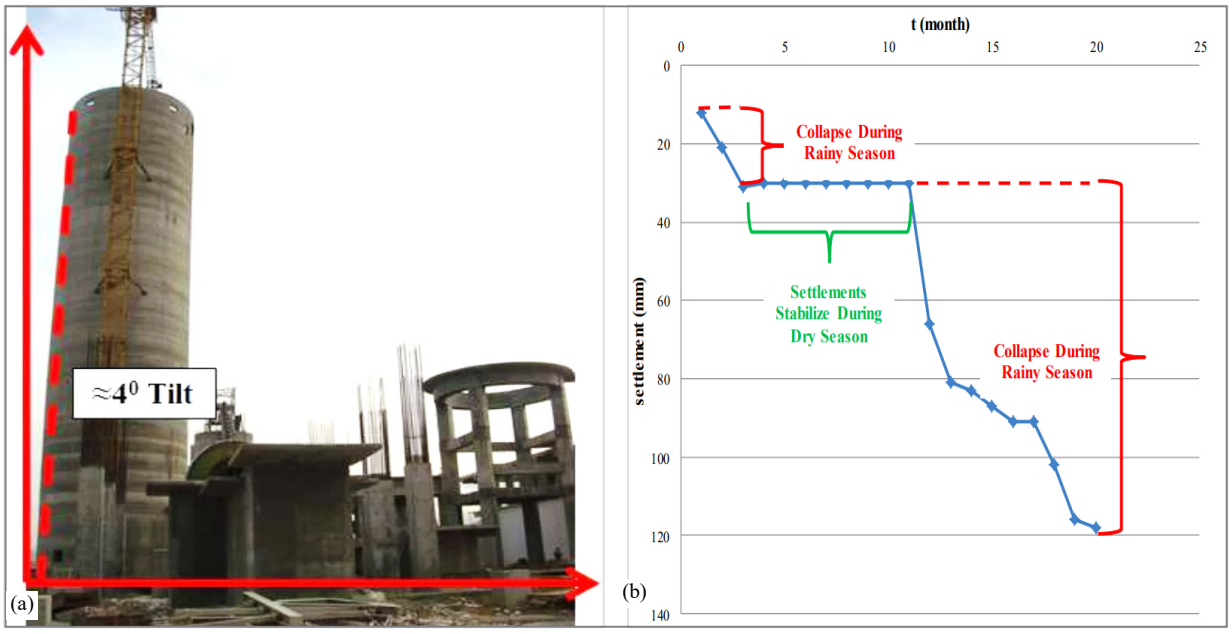

Figure 2-29, Hydrocollapse settlement induced by rainfall: (a) A tilted cement plant (b) Measured differential settlement (Source: Kalpakci, 2017)

An intense geotechnical investigation was conducted prior to the commencement of construction (that is, 184 exploration boreholes with length ranging from 15 to 25 m, and up to 16 to 24 m deep 7 cone penetration tests). However, potential hydrocollapse tests were not undertaken and the project was delayed by two years as a result of unforeseen volume change properties. The lithology of the site consisted of soft cohesive clayey soils with gypsum mixtures, different salts and micas. Soil was carbonated and sometimes loess-like, with coarse limestones at some depths.

The South African Home Building Manual (2014) suggested a minimum settlement of 10 mm in homes with basements, and 20 mm where there is no basement, to minimise masonry deformation. On the other hand, the Eurocode 7 (1994) allows for a uniform and differential settlement of 50 and 10 mm, respectively. In all the above case studies, observed settlement exceeded these permissible values. Thus, loessal deposits are detrimental for construction. It is also noted that the change in engineering properties is brought by contact between these sediments and water.

2.8 Summary of the Literature Review

It was established from the reviewed literature that wetting of loess induces volume change, which causes catastrophic deformation to civil engineering structures due to their brittle nature. As indicated in the review, loessal deposits are significantly problematic soils. However, no apparent study has been conducted on loess like soil in Mount Moorosi, Lesotho. This research was, therefore, considered necessary to generate new knowledge pertaining to volume change characteristics of soils in Mount Moorosi.

3 Geographical and Geological Background of Mount Moorosi Village

3.1 Introduction

This chapter presents the geographical location and climatology of the Mount Moorosi village in Lesotho. Furthermore, regional and site geological settings are discussed.

3.2 Geographical Site Location

Lesotho is a small country enclaved within South Africa with a total area of 30344 km^2. It is divided into four agroecological zones: the lowlands at an altitude ranging from 1400 to 1800 m AMSL, the Senqu River Valley at 1400 to 1800 m AMSL, foothills at 1800 to 2000 m AMSL and highlands from 2000 to 3482 m AMSL (Letsie & Grab, 2015). Mount Moorosi is situated at the southern part of Lesotho at an elevation of approximately 1700 m AMSL and 3 km from the Senqu River. Therefore, it forms part of the Senqu River Valley. Additionally, it is located 39.8 km northeast of Moyeni in the Quthing District, at a latitude of 30°16'39.76" S and longitude of 27°52'14.98" E. A series of mountains are adjacent to this residential area. The first of these mountains is Moorosi at 1834 m AMSL at 30°14'08.00" S and 27°52'55.69" E. The second one is Mokotjomela at 1943 m AMSL at 30°16'49.36" S and 27°52'58.04" E. Figures 3-1 and 3-2 illustrate the agroecological zones in southern Lesotho and the study area, respectively.

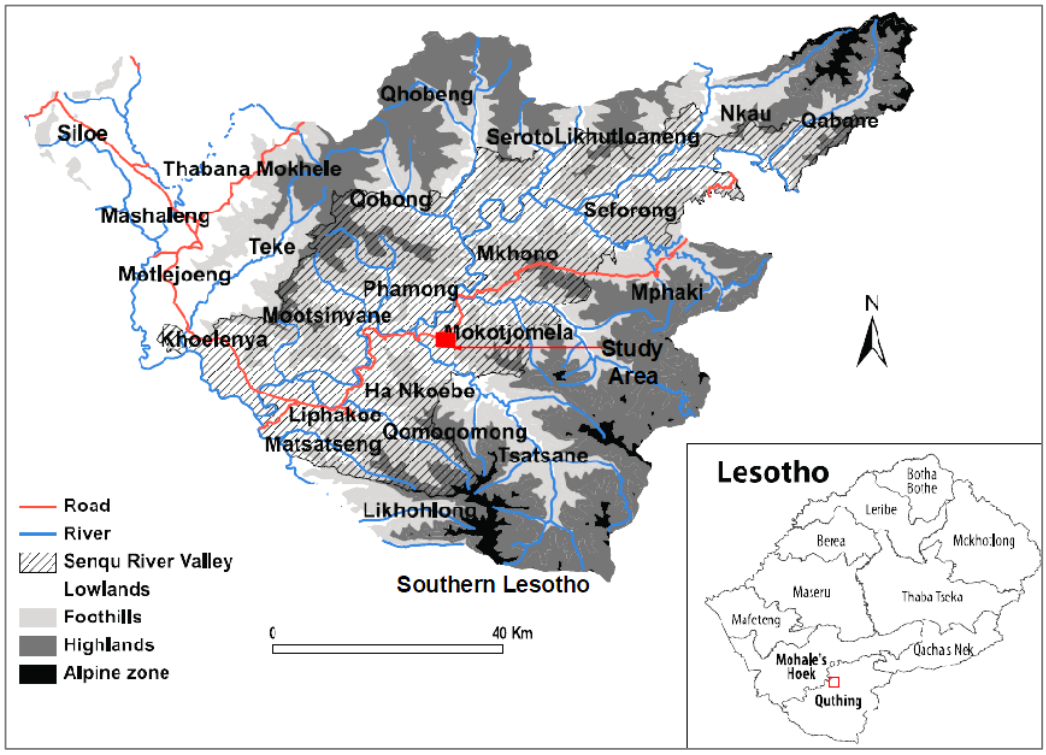

Figure 3-1, The study area within the agroecological zones in southern Lesotho (Source: Letsie, 2015)

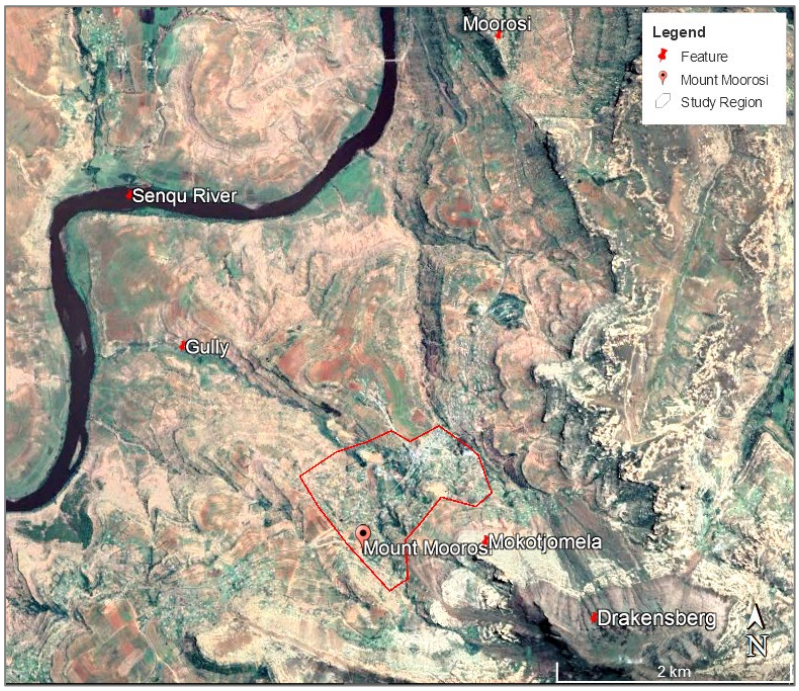

Figure 3-2, Mount Moorosi region (Source: Google earth, 2018)

3.3 Climatic Characterisation in Lesotho

Weather conditions play an important role in the disintegration of rocks, but limited information on the direct measurements of climatic parameters in Mount Moorosi exists. Letsie & Grab (2015) reported frequent occurrences of drought, strong winds, heavy snowfall, severe frost and floods in southern Lesotho, which includes Mount Moorosi. Furthermore, an AccuWeather forecast reported 37° C and -7° C as the highest and lowest temperatures in January and July 2018, respectively. An annual average of 11.5 snowfalls was observed from April to September, from 2003 to 2016, in Lesotho (Grab et al., 2017). Frost, on the other hand, occurs in 200 days per year (Sene et al., 1998; Stephanie et al., 2009). Moreover, an average annual rainfall of 780 mm was recorded from October to March in 1998 in Lesotho (Sene et al., 1998). Based on the weather conditions, the estimated Weinert *N* value between 2 and 5 in the Mount Moorosi Region indicates a moderate climatic region (Weinert, 1980).

3.4 Regional and Site Geology

Geographical coordinates indicate Mount Moorosi to be situated within the Karoo supergroup basin. This formation refers to the forefront land of Cape Fold Belt in southern Africa and is grouped into Dwyka, Ecca, Beaufort (Adelaide and Tarkastad), Stormberg and Drakensberg (Catuneanua & Elango, 2001). These formations were developed under several environmental phases that include the underfilled (deep water), followed by either filled (shallow marine) or overfilled (continental) (Sinclair & Allen, 1992). A top view map of the Karoo basin together with the location of the Mount Moorosi settlement are presented in Figure 3-3.

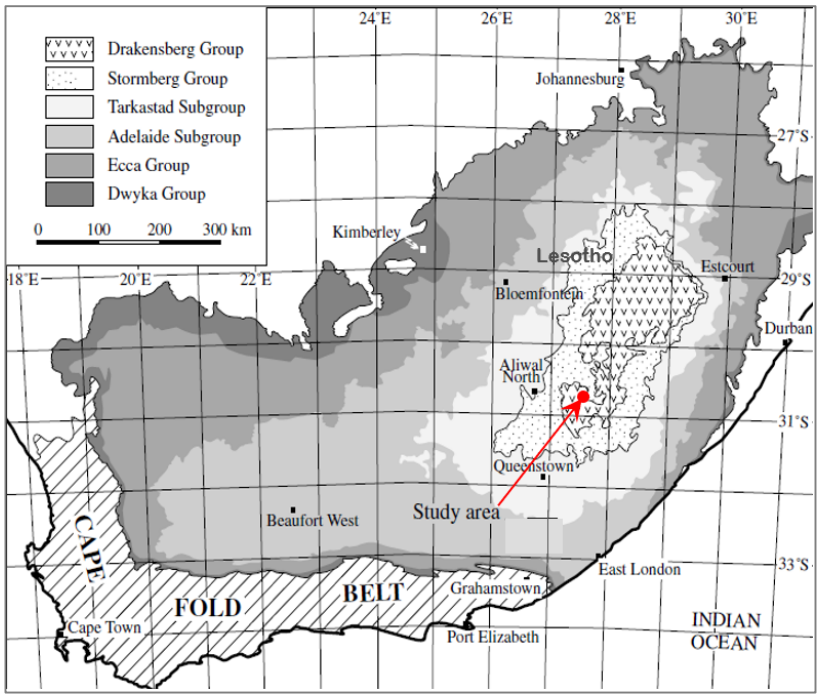

Figure 3-3, Karoo formation top view map (Source: Catuneanua & Elango, 2001)

As depicted on the cross section in Figure 3-4, the Karoo covers the whole of Lesotho, and the Drakensberg Mountains form its highest point. Furthermore, this uppermost ground covers two-third of Lesotho's total land area (Carroll & Bascomb , 1967). The Karoo's second topmost land is the Stormberg on the foothills of the Drakensberg, and it is followed by the Beaufort. The lithology of the Stormberg is of importance for this research given that the region under investigation is situated within it.

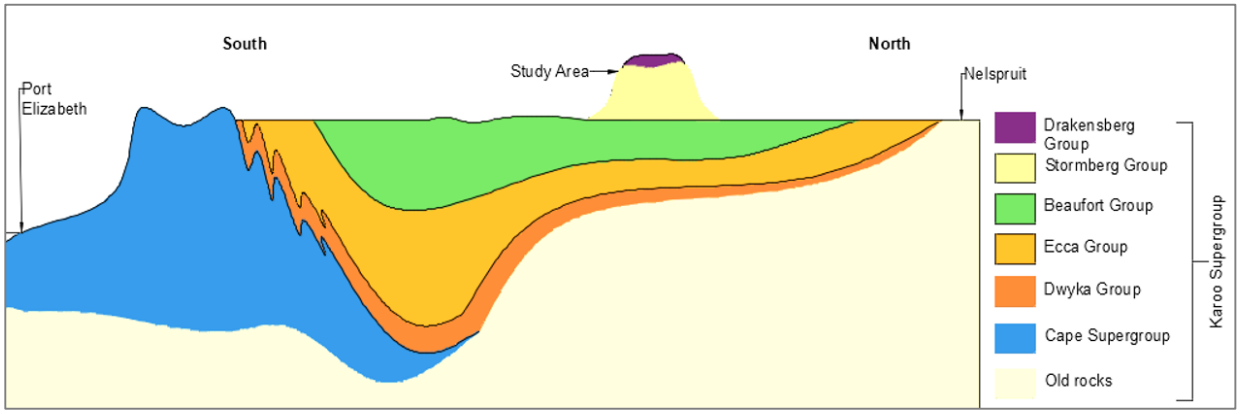

Figure 3-4, Karoo geological cross-section (Source: McCarthy & Rubidge, 2005)

Figure 3-5 illustrates a geological map of Lesotho, as extracted from the mineral map of the Republic of South Africa (RSA). It indicates that the Stormberg landform is further divided into three sub-formations, namely: the Molteno, Elliot and Clarens. These formations are of sedimentary origin (Catuneanua & Elango, 2001).

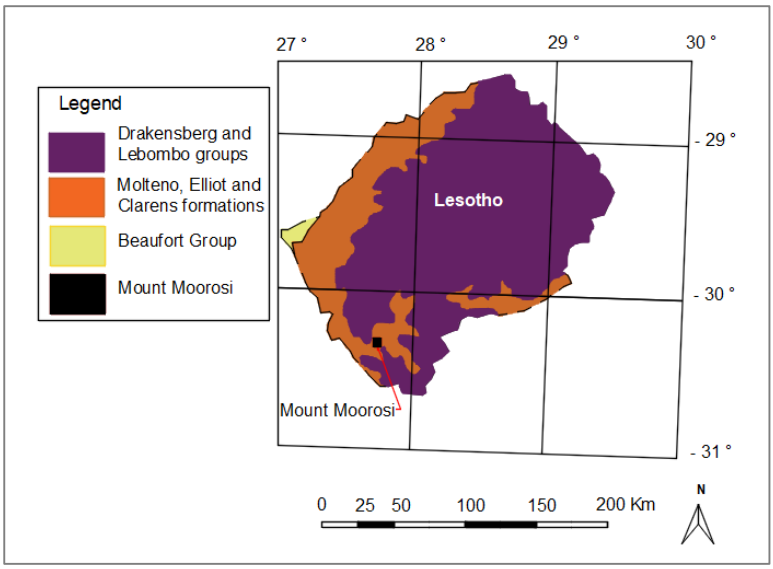

Figure 3-5, Geological map of Lesotho (Extracted from RSA mineral map, 2018)

The stratigraphy of the sub-lands in Stormberg and the environment in which they were formed are presented in Figure 3-6. It indicates that both the Molteno and Elliot were formed under fluvial conditions, while Clarens, also the youngest, was developed in the aeolian setting (Catuneanua & Elango, 2001). Additionally, during the deposition of the latter landform, a huge loess type deposits and cross-bedded dunes existed (Johnson et al., 1996). It is also the uppermost section of the Stormberg, and overlaid by the Drakensberg range (Brink, 1983). It is underlaid by the Elliot which is also superimposed on Molteno.

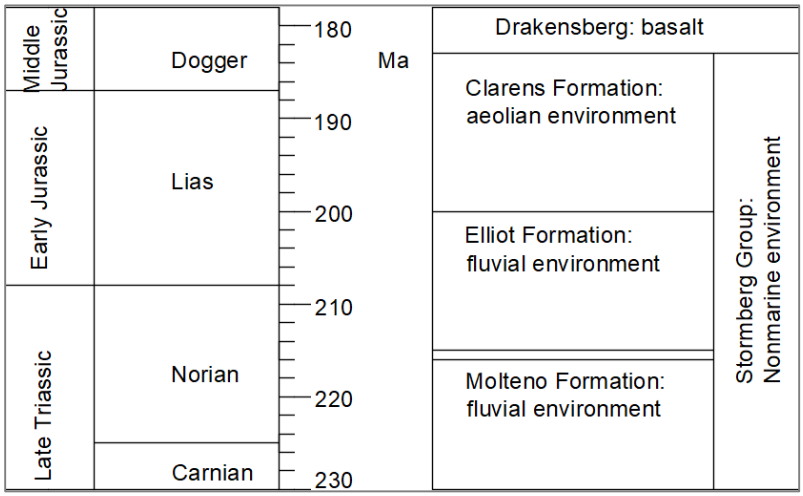

Figure 3-6, Stratigraphy of the Stormberg group (Extracted from Catuneanua & Elango, 2001)

Figures 3-2, 3-4, 3-5 and 3-6, presented earlier, were also used as complementary approaches to show that Mount Moorosi and Mokotjomela are positioned within the Clarens part of Stormberg, next to the Drakensberg. Dollman et al. (2017) also indicated the distribution of the upper Elliot formation within the study region.

Three distinct types of sedimentary rocks, which include sandstone, siltstone, and mudstones were highlighted in the Clarens (Rooy & Schalkwyk, 1993). Furthermore, the Elliot primarily consists of mudrocks interbedded with sandstones (Rooy & Schalkwyk, 1993). Brink (1983) reported that residuals of Karoo sandstone have a rapid collapse when saturated. Conversely, the Karoo mudrocks undergo rapid deterioration due to variation in temperature and humidity (Olivier, 1979) to form residuals with an expansiveness ranging from medium to occasionally high (Brink, 1983). Besides, the estimated Weinert *N* value between 2 and 5 in Mount Moorosi indicates the decomposition of rocks and the possibility of kaolinite clay formation (Guideline for Human Settlement Planning and Design, South Africa, 2005; Weinert, 1980). Table 3-1 provides the classification of the rocks within the Stormberg. These foregoing literatures show the possibility of volume change in soil in the study region.

Table 3-1, Classification of rocks within Stormberg (Source: Brink, 1983)

Formation	Thickness, m	Rocks	Reference
Clarens	Maximum of 300 and mean of 150	Red and green mudrocks, buff sandstone	Erikson (1981) Beukes (1970)
Elliot	500	Red and brown mudrocks, buff to yellow sandstone	Visser & Bothe (1980)
Molteno	460	Green and red mudrocks, buff sandstone	Turner (1980)

The buff sedimentary rocks are outcropping on Mountain Mokotjomela, which is situated on the uphill of Mount Moorosi (Figure 3-1 presented earlier). Other existing rocks, such as reddish to brown weathered mudrocks and sandstones, are depicted in Figure 3-7. This observation shows that the lithology from the literature is conforming with the images extracted from Google map.

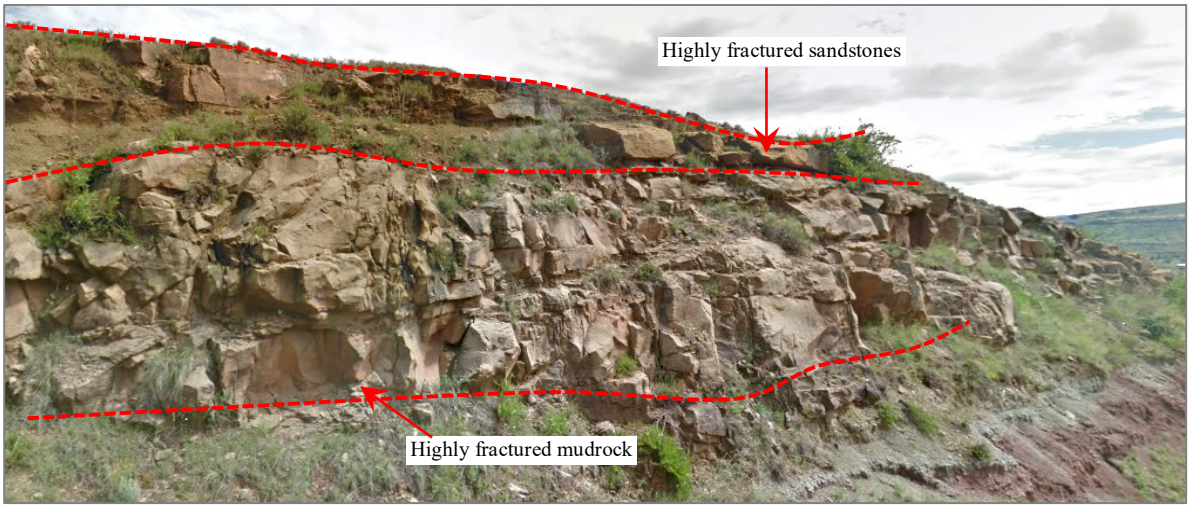

Figure 3-7, Tabular mudrock and sandstone beds (Source: Google map, 2018)

Figures 3-8 and 3-9 show 2 to 2.5 m thick soil with diverse colours, but reddish-brown sediments are predominant. Minor deposits include greyish and black cohesive residuals. The numerous gullies that occur on these soils are a clear indication of severe erodibility. In some areas, this soil is underlaid or overlaid by either highly weathered tubular mudrocks or sandstones.

Figure 3-8, Eroded standing soil wall (Source: Google map, 2018)

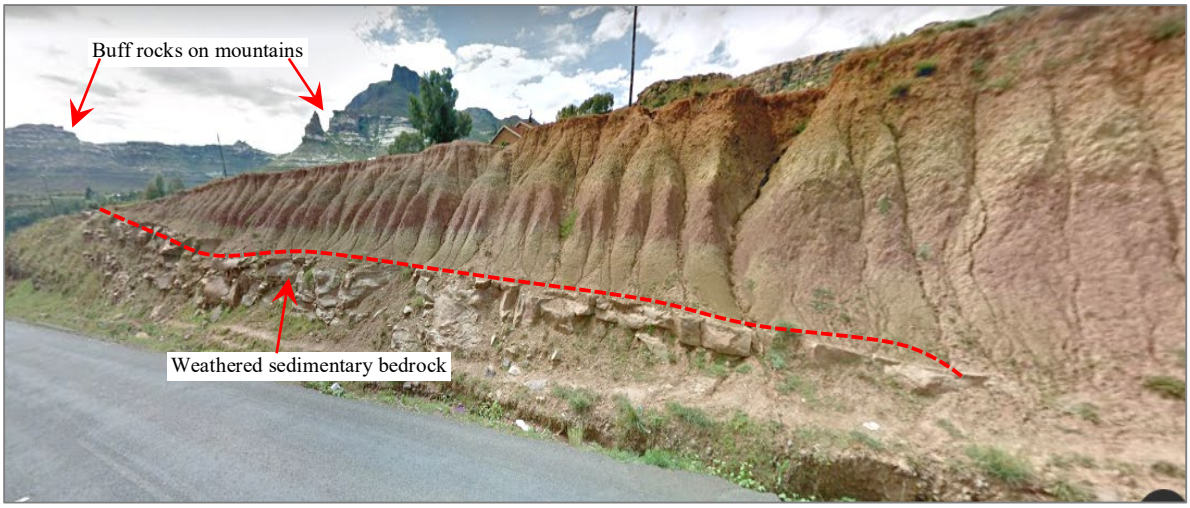

Figure 3-9, Soil sediments on highly fractured bedrock (Source: Google map, 2018)

During the construction of a bridge between Phamong and Mount Moorosi across the Senqu River in 2014, ten deep geotechnical exploration borehole logs were prepared by Enviro-geotech company that provides drilling services. These boreholes were located at altitude of 30°14'21.43" S and longitude of 27°52'26.22" E, approximately 3 km from the Mount Moorosi residential site. They extended to a mean depth of 30 m and were scattered within a length of 140 m. Similar to the reviewed literature regarding the lithology of the Stormberg (refer to Table 3-1), the logs showed the occurrence of both the mudrocks and sandstones. A ground profile developed herein, based on these logs is presented in Appendix A.

3.5 Cracks on Selected Houses in Mount Moorosi

It was important to visit the site to ensure a profound insight into the conditions of the existing houses in Mount Moorosi. Twelve houses scattered around the area were observed (Figure 3-10), and the extent of their damage was categorised based on recommendations suggested by Burland (1977).

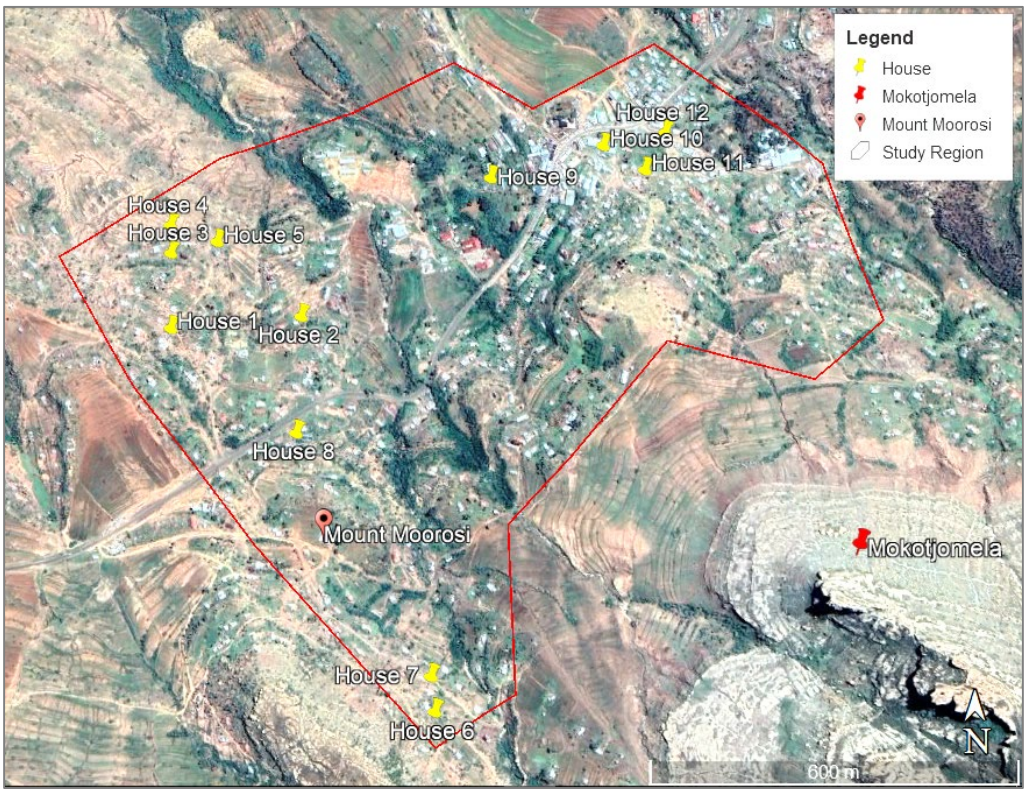

Figure 3-10, Map of the visited sites in Mount Moorosi (Source: Google Earth, 2018)

Table 3-2 summarises the cracks observed on selected buildings. Based on Burland (1977) guidelines, the noted degree of damage was generally slight (crack width ranging from 1 to 5 mm), slight to moderate (1 to 15 mm), moderate (between 5 and 15 mm) and severe (fissures with a width between 5 and 25 mm). The common extent of defects was moderate, which indicated that cracks on most houses were more than the allowable value of less than 5 mm (South African Home Building Manual, 2014). They, therefore, demonstrated a serious deformation and immediate need for deployment of the remedial measures. It was noted that cracked walls were slightly leaning in some of the houses, concrete plaster was spalling, concrete floor had separated from walls and the ceramic tiles were also broken along the fissure.

The crack patterns were vertical or diagonal and stepped. This failure trend on structures was related to the ground volume change in several documented literatures (Page, 2001; Ercio et al., 2014; Arvind, 2017). In fact, an excavation of the overburden soil below a crack on one of the houses also revealed that the opening originated from a strip footing. As a result, it was deduced from these observations that the properties of the underlaid soil could possibly be contributing to

the noted defects. It was thus necessary to investigate the volume change properties of the soil in Mount Moorosi.

Table 3-2, Classification of the damage on the selected houses in Mount Moorosi

House	Coordinates	Damage descriptions	Damage category
1	30°16'28.66" S 27°52'02.53" E	Vertical/shear and stair stepped cracks on walls Openings above window lintels and on concrete floor Cracked wall is slightly leaning	Moderate
2	30°16'27.74" S 27°52'12.26" E	Vertical and hairline cracks on walls Fissures next to door frames	Moderate
3	30°16'23.22" S 27°52'03.88" E	Stair stepped and vertical fractures on the walls Cracks above window lintels, on concrete floor and on ceramic tiles Spalling of concrete plaster	Moderate
4	30°16'21.80" S 27°52'02.54" E	Recurring diagonal and vertical fissures on walls Cracks above window lintels Concrete floor separating from wall	Moderate
5	30°16'23.10" S 27°52'05.85" E	Recurrent vertical and stair stepped cracks on walls Openings below windows and above lintels Fissures on the concrete floor Cracked wall is slightly leaning	Moderate
6	30°16'53.00" S 27°52'22.50" E	Hairline, vertical and diagonal openings on walls Cracks on the concrete floor	Moderate
7	30°16'50.88" S 27°52'22.25" E	Hairline and fine cracks	Slight
8	30°16'35.42" S 27°52'12.15" E	Shear and stair-stepped cracks on walls Cracks below window Cracked concrete floor	Moderate
9	30°16'18.51" S 27°52'27.03" E	Shear and diagonal cracks on wall	Moderate
10	30°16'16.42" S 27°52'35.56" E	Recurring vertical fissures on walls Slightly leaning walls	Severe
11	30°16'18.10" S 27°52'38.75" E	Diagonal and vertical cracks	Slight to moderate
12	30°16'15.56" S 27°52'40.40" E	Stair-stepped and vertical openings	Slight to moderate

Figure 3-11 depicts some cracks on walls, floor, below and above the windows. These fissures were recurrent in most houses and extended from the outer wall surface to the interior. They also occurred in older as well as newly constructed structures.

Figure 3-11, Cracks on some of the selected houses in the Mount Moorosi village

4 Field and Laboratory Methodologies

4.1 Introduction

This chapter discusses the procedures followed during field work in Mount Moorosi and execution of the laboratory experiments. The in-situ work involved density measurements and excavation of the exploration trial pits for soil profiling. Conversely, laboratory methods were performed to classify the soil, determine its mineral composition, microstructural arrangement, soil strength and volume change.

4.2 Field Works

4.2.1 Trial Pits

Three trial pits (TP01, TP02 and TP03), less than 1 km apart, were excavated to establish the general properties and variation of soils underlying the study region. This was undertaken during the dry period in January 2018. Digging locations were selected based on the severity of the structural damage and a number of buildings affected within a locality. Their corresponding geographical coordinates are provided in Table 4-1 and are depicted in Appendix B. Excavation was extended to depths ranging from 2.1 to 3.0 m below the ground surface by a Tractor Loader Backhoe (TLB). These depths were selected due to a typical shallow zone of influence (that is, three times the base of the footing) below the centre of the strip foundations (Craig, 2004). Furthermore, resistance offered by the hard strata to TLB also influenced the exploration depths. Pits were dug to a width of 1.5 m and breadth of 0.6 m.

Table 4-1, The location of the trial pits

Trial pit ID	Coordinates	Final depth, m
TP01	30°16'29.66" S 27°52'03.05" E	3.0
TP02	30°16'55.31" S 27°52'24.54" E	2.1
TP03	30°16'22.39" S 27°52'03.28" E	3.0

The soil sampling was conducted based on the procedures recommended by Rowell (2014), while field profiling was based on the recommendations proposed by Jennings et al. (1973). Samples from various depths were prised from the four faces of the pit, into a labelled polyethylene plastic bag using a trowel, pick and spade. This disturbed soil was retrieved from several depths for classification purposes. The packaged samples were transferred into a wooden box, which was sealed with plastic to prevent exposure and possible contamination. A total of 400 kg of parcelled soil was loaded on a truck and couriered to the geotechnical laboratory at the University of Cape Town (UCT). Figure 4-1 depicts this soil in wooden boxes wrapped in plastic.

Figure 4-1, Packaged soil samples

The samples recovered at 0.6 m below ground surface were used for volume change, shear strength tests as well as soil mineralogy and morphology identification. This depth was within the zone of influence of typical foundations in the area.

4.2.2 Troxler Test

TMH-A10b procedures were followed to conduct the field density tests using a troxler equipment. These tests were performed in early April 2018, roughly three weeks after rain was experienced in the area. This period was selected to ascertain the change in moisture between dry and wet seasons.

Due to disturbed backfilled material in the original trial pits (TP01, TP02 and TP03), excavation for the density tests was conducted at approximately 1.5 m away. These pits had a width of 0.7 m, a breadth of 0.4 and a depth of 0.3 m. The bottom was levelled and a Troxler was gently lowered to measure bulk density along with moisture content at a depth from 0.3 to 0.6 m. The Troxler's direction was adjusted to approximately 120° within the same pit, and the second readings were taken. It was again changed by roughly 120°, and a final bulk density reading was logged. The density of the pit was determined from the average value of the recorded readings. The same technique was repeated in all new trial pits and findings were used in the laboratory during preparation of the reconstituted specimens. Table 4-2 and Figure 4-2 presents the density test locations and demonstrates a Troxler in one of the pits, respectively.

Table 4-2, The location of the Troxler Tests

Trial pit ID	Coordinates	Final depth, m	Location
TR01	30°16'29.66" S 27°52'03.05" E	0.3	Adjacent to TP01
TR02	30°16'55.31" S 27°52'24.54" E	0.3	Adjacent to TP02
TR03	30°16'22.39" S 27°52'03.28" E	0.3	Adjacent TP03

Figure 4-2, Troxler test on site

4.3 Laboratory Tests

To characterise the soil and determine its volume change properties, laboratory tests were executed on disturbed samples. These included index tests, phase and morphological identification, shear strength and volume change determination. Some tests procedures are briefly described as they are clearly stipulated in BS 1377-2-1990. However, detailed methods for triaxial and oedometer are provided due to a change in the determination of the predefined densities.

4.3.1 Index Tests (Foundation Indicators)

Index tests primarily consisted of sieve analysis and Atterberg limits determination. These were used to estimate the volume change properties of the soil and for profiling excavated trial pits. Table 4-3 provides the tests and the corresponding standard methods that were followed.

Table 4-3, Test methods for soil classification

Property	Test method	Standard method
Particle size distribution	Wet sieving	BS 1377-2-1990
Fine particle size distribution	Hydrometer	BS 1377-2-1990
Specific gravity	Small pycnometer	BS1377-2-1990
Liquid limit	Casagrande	BS 1377-2-1990
Plastic limit	Plastic limit	BS 1377-2-1990
Shrinkage limit	Linear shrinkage	BS 1377-2-1990

In particle size distribution, the investigation involved wet sieving, to deflocculate aggregated particles. Generally, more than 65 % of soil passed through a 0.063 mm sieve. Consequently, a hydrometer analysis had to be performed for further classification of fine grains (that is silt and clay). Additionally, a specific gravity was required for processing data obtained from the hydrometer test.

The Atterberg limits were determined for the identification of soil plasticity. This parameter was used along with clay fraction as an indirect measurement of potential soil swell. Furthermore, soil was categorised based on the Unified Soil Classification System (USCS) to indicate the possibility of expansiveness.

4.3.2 Phase and Morphoscopic Analysis

The X-Ray Diffraction (XRD) and Scanning Electron Microscope (SEM) are complementary approaches conducted on soils for mineralogical or phase quantification and morphological identification, correspondingly.

4.3.2.1 X-ray Diffraction

Quantification of minerals is essential in the evaluation and prediction of the overall behaviour of soil. The XRD analysis in this study was conducted at the Centre for Minerals Research, based at UCT. This investigation was performed for the phase (chemistry and atomic arrangement) quantification of samples finer than 0.063 mm. Particle size selection was prompted by the fact that most of the grains passed a 0.063 mm sieve (65 to 92 %). The incident x-ray waves were diffracted by atomic planes to develop a diffraction pattern that had information about the atomic arrangement within the crystal producing them (Figure 4-3). The diffracted intensities at 2θ from 10 to 120° (diffraction angle) were recorded by a detector. A wider range of 2θ was selected to detect diffraction in any possible orientation of the atomic planes. Intensities were directly proportional to the concentrations of the minerals bending them. Therefore, the Bruker Topas 4.1 software and Rietveld Method were used for mineral identification, as well as quantification of the relative amounts (weight percentage) from the measured intensities.

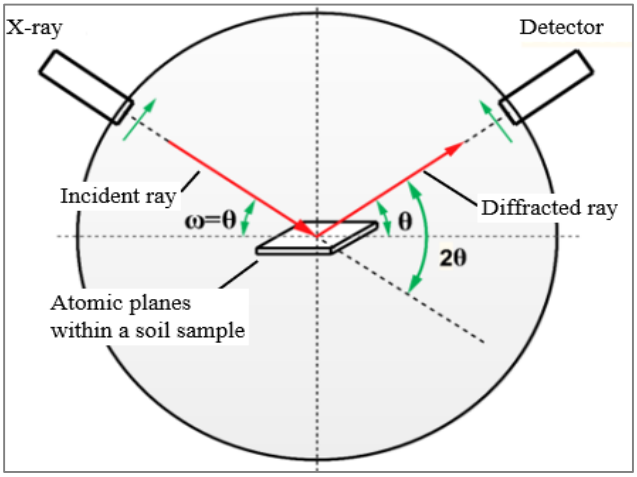

Figure 4-3, Schematic of Bragg-Brentano for XRD (Source: Raza, 2017)

4.3.2.2 Scanning Electron Microscope (SEM)

Structural arrangements of identified minerals were observed under SEM instrument. This analysis was executed for particle aggregates and disturbed grains, at the Centre for Imaging Analysis at UCT. The intact soil lumps and disturbed grains provided an opportunity to view the wider range cementation as well as bonding between individual grains, respectively. Soil samples were sprinkled on SEM stubs covered with carbon glue to secure them during examination. These were then transferred to a Nova nanoSEM instrument for viewing. The respective images were generated by focusing a beam of electrons on a soil sample (scanning). Selected micrographs were observed at a magnification ranging from 100x to 100000x.

4.3.3 Volume Change Tests

The potential volume change was determined based on both free swell and double oedometer tests. The oedometer was mainly used to investigate potential water induced settlement, while free swell measured the soil expansivneness. A slaking test was also used as a quick way to predict the susceptibility of the soil to collapse.

4.3.3.1 Free Swell Test

The free swell test aimed to determine the percentage increase in a volume of submerged soil when confinement was not provided. It was determined based on the procedure proposed by Gibbs & Holz (1956). A soil sample passing a 0.425 mm sieve was placed in a metal dish which was then dried in an oven at 105 °C for 24 hours. The selected temperature and duration of drying were recommended by the BS 1377-2-1990 to achieve the appreciable dryness of the soil. The dried sample was placed in a desiccator for 30 minutes to cool. 50 g of this soil was obtained by weighing it in a glass dish on a 0.01 g accuracy balance. This soil was then loosely placed to 10 ml mark in a 25 ml glass measuring cylinder. 50 ml of distilled water was poured into a 50 ml measuring cylinder placed on a glass plate. The dry soil in a 25 ml measuring cylinder, was then slowly and gently poured into the cylinder containing water and allowed to freely swell for 24 hours. The new volume of the soil was then recorded. Figure 4-4 depicts the submerged soil in the measuring cylinders.

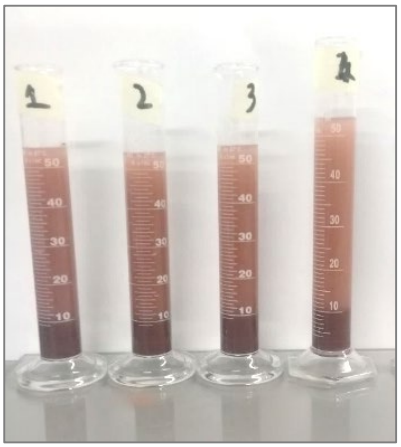

Figure 4-4, Submerged soil during a free swell test

4.3.3.2 Slaking Test

A quick slaking test was conducted based on the procedure proposed by McGarry (2004). The susceptibility of the wetted samples to collapse was determined from this test. It is a type of soil collapse in which the inundated and unconfined aggregates are disaggregated as a result of the removal and separation of clay cementation from silt (Moriwaki et al., 1977; McGarry, 2004; Liu et at., 2015). The test involved gently placing an air-dried soil crumb at the bottom of a transparent dish in 250 ml of distilled water. After 10 minutes of inundation, the degree of disaggregation was visually evaluated and rated. In this test, the standard rating ranges from 0 to 4, with 0 indicating the lowest potential and 4 the highest (McMullen, 2000). At a 0 rating, the lump remains intact, while it gets deflocculated into single grains at 4 (McMullen, 2000).

4.3.3.3 Double Oedometer Test

A double oedometer test was undertaken to determine the hydrocollapse potential of the sediments. Several pairs of tests were performed on specimens at the respective in-situ moisture contents and densities, while other identical samples were tested under saturated conditions. This assisted in determining the collapse or expansion triggered by water (hydrocollapse). The specimens preparation involved sieving, prewetting, curing, compaction and assembling the oedometer. The BS 1377-5-1990 test methods were followed. The initial stage involved sieving soil through a 5 mm sieve, in accordance with the BS 1377-2-1990, to remove larger particle aggregations. Soil representatives were taken from the sieved material and put in three tins of known mass for moisture determination. A total mass was measured on a balance with an accuracy of 0.001 g and the tins were placed in a 105 °C oven. This temperature was considered enough to dry soil within a duration of 24 hours (BS 1377-2-1990). When this time had elapsed, tins were transferred to a desiccator to cool for 30 minutes, and the final mass was measured. A moisture percentage of the soil was attained from the change in mass.

Soil sample prewetting

A clean, dry metal dish was placed and zeroed on a weighing balance with a capacity of 16.1 kg. The same balance was used for all samples with masses exceeding 700 g. Soil passing a 5 mm sieve was placed into a dish and a mass of 1 kg was recorded. From this sample, the additional water content required to bring the specimen to in-situ moisture percentage was calculated from Equation 4-1.

$$w = m \times (tw - sw) \qquad \textbf{Equation 4-1}$$

Where w is the additional moisture required, m is the total mass of the soil, tw is the target field moisture and sw is the soil moisture.

The final water required was then measured in a 100 ml bottle and gently sprayed over the soil. Mixing was thorough through the use of a spatula until a uniform water distribution was achieved. The mixture was transferred to an airtight plastic bag, which was sealed and stored for 24 hours at a temperature maintained by the air-conditioner at 23 °C.

Specimen Compaction for Oedometer Test

The compaction was initially conducted in a mould, as recommended by BS 1377- 4 -1990, but the sample crumbled when extruded, and cut with a wire-saw to fit the oedometer ring. This was caused by a low moisture content, which reduced the cohesive attraction between the individual aggregates. A similar problem was reported in loess soil of Indiana by Howayek et al. (2012). To avoid damage to specimens, the compaction was conducted in a consolidation ring instead.

The volume of the compaction consolidation ring was determined from its height (20.4 mm) and diameter (63 mm), which were measured with vernier caliper. From this volume, the required soil mass for compaction in the ring was calculated using Equation 4-2.

$$m = \rho \times v \qquad \textbf{Equation 4-2}$$

Where, m is the mass of soil, ρ is the field bulk density and v is the volume of the oedometer ring.

A consolidation ring was lightly oiled with silicon grease to reduce friction between the mould and a specimen to be compacted. This ring, with a known mass, was secured on a flat compaction platform on a level concrete floor. Figures 4-4 (a) and 4-4 (b) show the apparatus for oedometer specimen preparation and the compaction in progress.

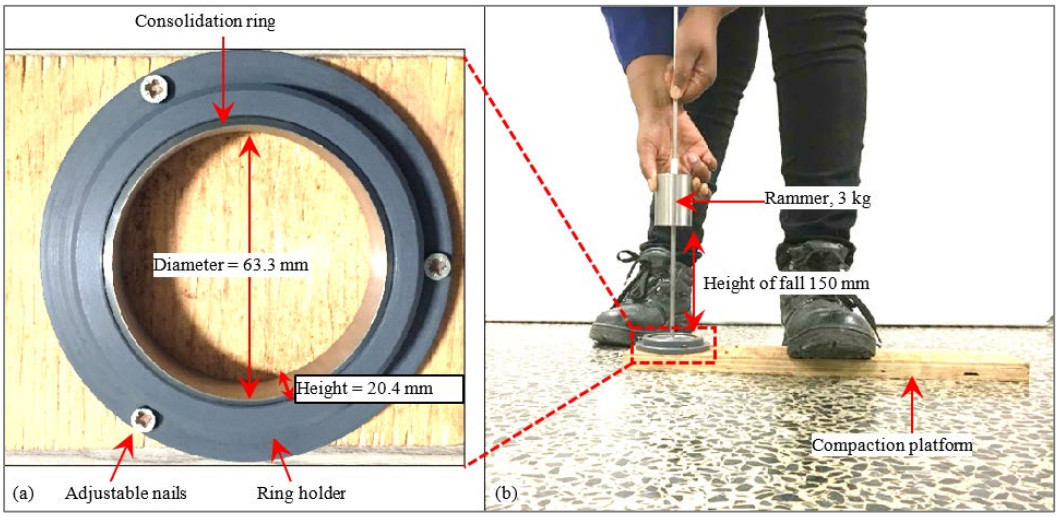

Figure 4-4, The apparatus for preparation of oedometer test specimen

It is important to point out that many trials that involved changing the number of layers, drops and the height of fall were performed to establish the predefined field density. Therefore, the calculated mass of a prewetted soil was divided by three, as per the number of soil layers. The mass of the first layer was measured in a small bowl on a balance with a sensitivity of 0.001 g. This soil was then evenly spread in the ring using a small scoop. One foot of the operator was placed on the platform plank to hold the ring down (Figure 4-4 (b)). The soil was compacted by applying nine uniform blows by an oiled metal rammer, freely falling at a height of 150 mm. This rammer was weighing 3 kg and had a 60 mm diameter surface. The same compaction

procedure was repeated on the second and third layers. To improve blending with the successive soil, each layer was slightly scratched. The ring was then detached from the platform and thoroughly wiped with a clean dry cloth. Finally, excess soil was trimmed off, while cavities were filled with soil and gently pressed with a metallic file. The mass of the ring with soil was recorded to determine the density of the specimen.

Setting-up of the Oedometer Cell

Figure 4-5 illustrates the components of an automated GDS oedometer, used to conduct a series of consolidation tests. It had a maximum applied load of 10 kN and readability up to 0.001 kPa. The transducer had a displacement of 10 mm and could record vertical movements up to 0.001 mm.

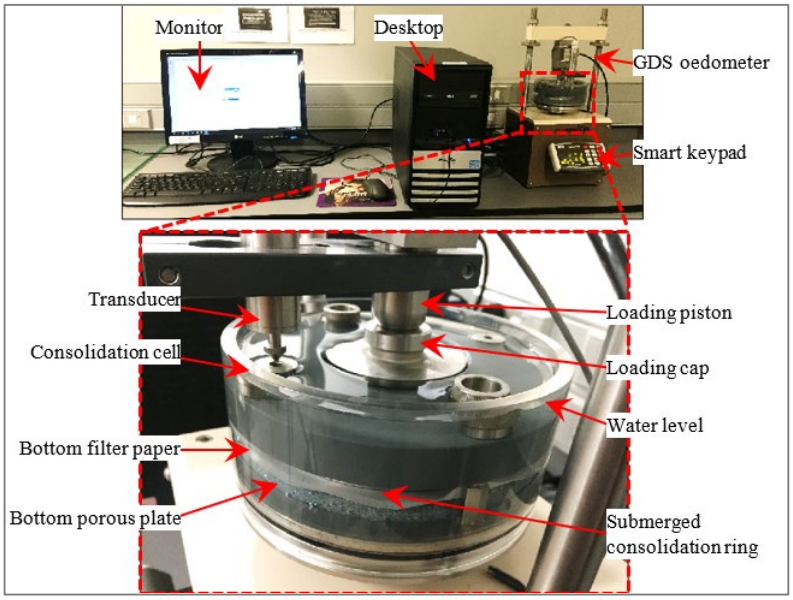

Figure 4-5, Oedomete apparatus and a submerged specimen

The initial step in setting up the consolidation cell was cleaning the corrosion resistant porous plates with a nylon brush. They were thereafter immersed in boiling water for 15 minutes, to saturate the pores. These plates were then cooled in cold water for 10 minutes. The bottom porous plate (95 mm diameter and 9.5 mm thickness) was placed within a consolidation cell. A filter paper that had been soaked in distilled water for 15 minutes was gently aligned on this disc to prevent the intrusion of soil particles into the pores. A compacted specimen in a metal ring was then centrally positioned on the bottom plate and covered with a filter paper prepared, in the same way as the previous one. Another porous plate (diameter of 60.5 mm and 10 mm thickness) was placed on the top surface. It was provided with a corrosion resistant metallic cap which formed the base of the loading piston. The cell components were correctly assembled and bolted in place to achieve the right alignment and a lateral confinement of the consolidation ring. A loading frame was lowered with the help of the two side tie rods to apply a seating load of 2 kPa on the loading cap. The low stress was selected to minimise settlement during the saturation phase. Water was added from the bottom to the brim of the consolidation cell using a washer

bottle, after the transducer reading had attained a constant value. The specimen was inundated for 24 hours to ensure adequate soil saturation.

Configuration and Running of GDS automated oedometer

A GDS Automatic Oedometer System was used for the final test setup. This included inputting specimen dimensions, setting test conditions, displaying real-time data and automatically recording the information. The applied pressure sequence was 6, 12, 25, 50, 100, 200, 400, 800 and 1600 kPa, each held constant for 24 hours on a specimen. This duration was regarded adequate to complete the primary consolidation triggered by the external loadings (BS 1377-5-1990). The light pressures (< 25 kPa) were similar to stresses from the typical buildings in the study area, while higher values simulated heavy loadings from structures that could possibly be constructed in future. Besides, the degree of hydrocollapse was quantified under high stresses (200 and 300 kPa), and some consolidation parameters are determined under stresses higher than the pre-consolidation pressure. The data (displacement, applied stress, applied force and strain) was recorded at close time interval (5 seconds) to reflect even the slightest specimen deformation. The test was started and the live data at different automated increments of pressures was displayed.

At the end of the test, an unlock button on the oedometer smart keypad (refer to Figure 4-5) was pressed to allow for external monitoring of the loading piston. The consolidation cell was removed from the load frame by pressing button three on the keypad, and manually unscrewing the side tie rods. The consolidation cell was then carefully removed, and the water was drained for 15 minutes. This was followed by dismantling of the cell, and determination of the mass of saturated specimen. Samples were taken at the top, centre and bottom of the ring for moisture determination. The same procedure was repeated for an identical specimen, but water was not added to the consolidation cell. This was done to determine the potential settlement due to increase of water. Table 4-4 summarises the compaction in several specimens.

Table 4-4, Summary of Odometer samples compaction

Pit	Dry/wet	No. of drops	No. of layers	Moisture	Height of fall, mm	Bulk density, g/cm³
1	Dry	7	3	7.8%	150	1.812
	Wet	7	3	7.8%	150	1.812
2	Dry	9	4	7.5%	150	2.001
	Wet	9	4	7.5%	150	2.001
3	Dry	8	3	6.6%	150	1.952
	Wet	8	3	6.6%	150	1.953

4.3.4 Strength Test: Consolidated Undrained Triaxial (CU)

A triaxial test was undertaken to establish the shear strength parameters of soil samples. Both saturated and unsaturated consolidated undrained shear tests were executed at confining

pressures of 250, 100 and 50 kPa on GEOCOMP triaxial. The consolidation phase was selected to simulate the prior consolidation initiated by the overburden and superimposed structures at the field. Conversely, undrained phases were prompted by the cohesive nature of tested samples, which rendered low permeability and longer inundation period. These confining pressures provided an opportunity to assess the shear stress-strain behaviour under diverse applied pressures. The sample preparation was similar to that of oedometer, with the only variation being the mould used for specimen compaction. It was a lightly oiled split mould with a known mass and mean internal diameter of 52.3 mm. For accurate shearing, the specimen's height had to be twice the diameter. These dimensions were used along with the field bulk density to determine the required mass of the cured soil.

Specimen Compaction for Triaxial Test

Figures 4-6 (a) and 4-6 (b) show the apparatus for a triaxial sample preparation and a specimen being compacted. Like in oedometer tests, many trials that involved changing the number of layers, drops and height of fall had to be performed to get the predefined field density. The soil was, therefore, divided by six based on the predetermined compaction layers. A lightly oiled metallic pad was fitted at the base of a split mould, and both were transferred to a flat metallic platform. The mass of the first soil layer was measured in a dish placed on a balance with an accuracy of up to 0.001 g. This soil was transferred to split mould and uniformly levelled. A greased rammer of 2.5 kg mass and freely dropping at a height of 200 mm was used to compact it. The mass of other layers was similarly measured and compacted. A total of 35 blows was made in all six layers, and each was scratched before the addition of the successive one. The final mass of the split mould together with a specimen was recorded to ensure that the targeted density was attained. The compaction data for all specimens is summarised in Table 4-5.

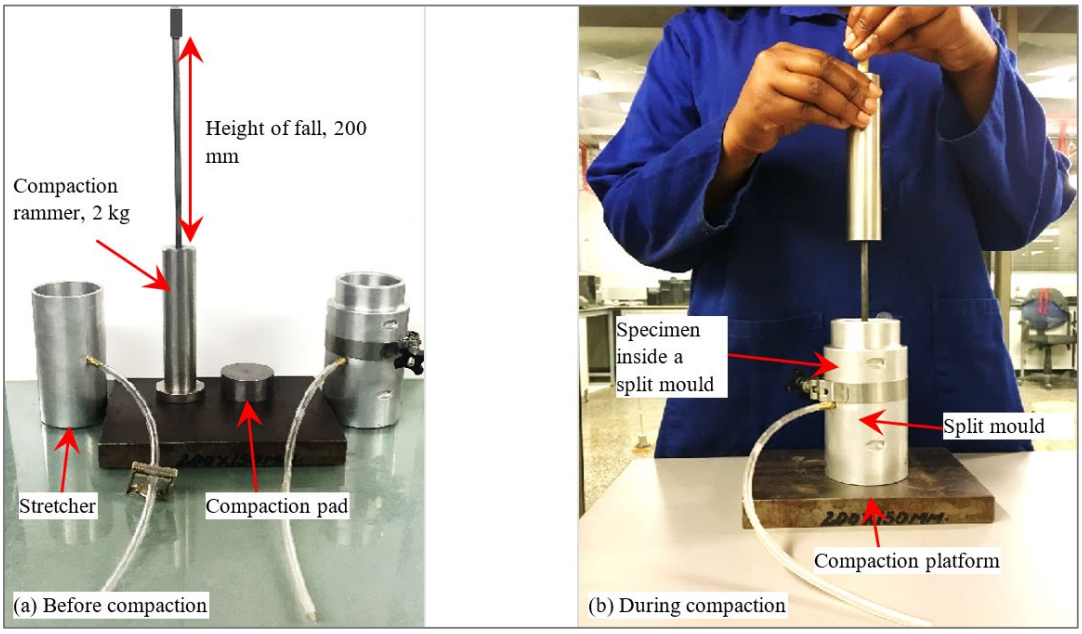

Figure 4-1. Apparatus for triaxial test specimen preparation

Table 4-5, Compaction summary of triaxial tests

Pit ID	Dry/wet	Confining pressure, kPa	No. of drops	Height of fall, mm	Moisture, %	Bulk density, g/cm³
PT01	Dry	50	25	200	7.8	1.810
		100	25	200	7.7	1.812
		250	25	200	7.8	1.811
	Wet	50	25	200	7.9	1.812
		100	25	200	7.8	1.810
		250	25	200	7.7	1.812
PT02	Dry	50	38	200	7.5	2.036
		100	38	200	7.4	2.036
		250	38	200	7.5	2.027
	Wet	50	38	200	7.4	2.027
		100	38	200	7.4	2.036
		250	38	200	7.5	1.901
PT03	Dry	50	35	200	6.4	1.964
		100	35	200	6.5	1.955
		250	35	200	6.4	1.960
	Wet	50	35	200	6.7	1.964
		100	35	200	6.4	1.960
		250	35	200	6.5	1.964

Setting-up of the Triaxial Cell

For an unsaturated test, 5 mm thick corrosion-resistant solid plates with diameters of 52 mm were used instead of porous ones. The first plate was placed on the base cap of the base pedestal. A split mould was lifted, and the metal pad was left behind. The mould was then centrally mounted on the bottom metal disc. The two halves of the mould were gently split and removed (Figure 4-7 (a)). The diameter and height of the specimen were quickly measured to avoid loss of moisture. The second solid plate, along with the top cap were sequentially placed at the top of the specimen. A high density impervious latex membrane (0.2 mm thick) was evenly fitted to a stretcher and air was sucked out. This membrane was then gently encapsulated around a specimen. It had an adequate length to extended on both the bottom and top caps of the cell. O-rings were also slowly attached over this membrane with the help of a stretcher. Two o-rings were provided on the base cap, while two more were on the top cap. They prevented the permeation of the pressurised water into specimen at the ends of a membrane. The loading piston was clamped to the cell body with three tie rods.

The triaxial cell was filled with water and the air was allowed to escape through the air vent. The cell was transferred to the triaxial machine and adjusted to bring the piston just in contact with the loading frame. This piston was screwed in place and the two flow tracks were connected to the base pedestal. The specimen encapsulated in a membrane inside a triaxial cell and the final setup are depicted in Figure 4-7 (b).

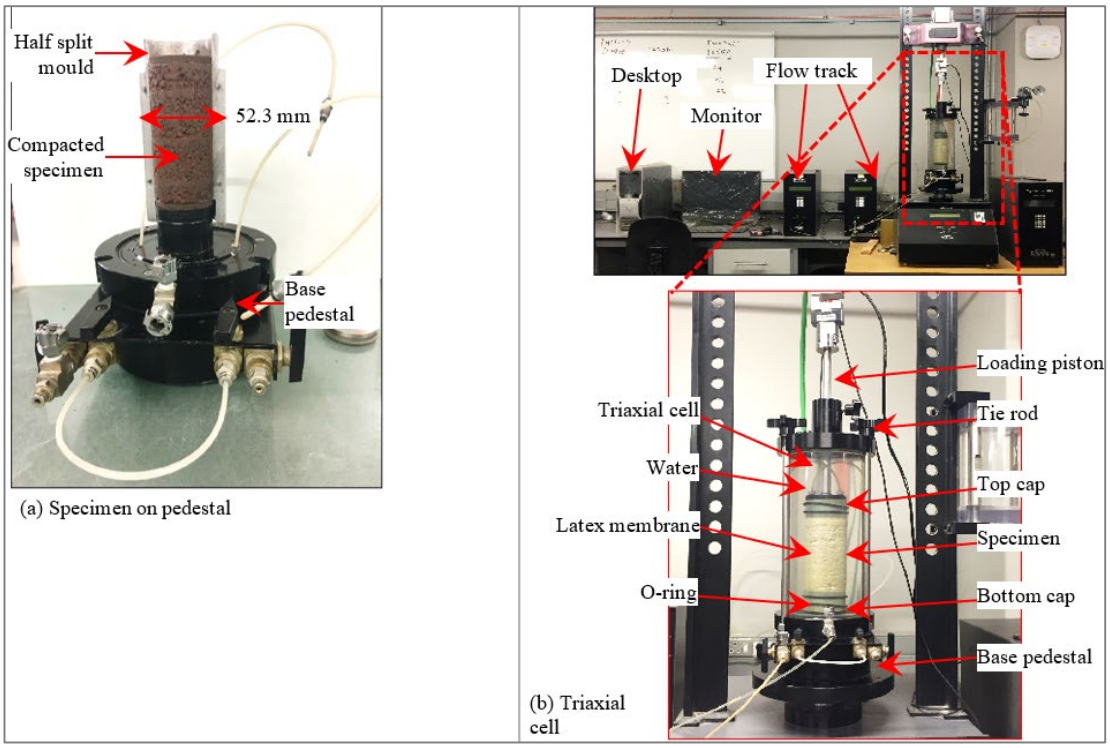

Figure 4-2. Triaxial cell components

Setting Up of GEOCOMP Triaxial Test

Final setting up was done on a triaxial GECOMP computer programme. Inputted information included the specimen dimensions and the test conditions (that is, saturation, consolidated undrained and shear phases). Saturation conditions were set to zero as the first test was unsaturated and the consolidated undrained phases were activated. For a confining pressure of 250 kPa, the consolidation stress was applied at a rate of 13.7895 kPa/min at a maximum duration of 720 minutes with a minimum value of 60 minutes. A shearing rate of 0.02 mm/per min and a maximum strain of 22 % were entered. These parameters were selected based on the recommendations of ASTM D4767-11 and BS 1377-4-1990 for various soil types. When the set-up was completed the test was started and the programme automatically recorded the measured data (loadings, strains, deviator stresses and pore pressures). At the end of the test, the triaxial was dismantled and representatives were taken at the top, centre and bottom of the specimen for moisture content determination. The same procedures and setting up were repeated for all the specimens under different confining pressures (100 and 50 kPa).

In the case of the saturated consolidated undrained tests, the similar procedures and equipment were adopted under the equal set of confining pressures (250, 100 and 50 kPa). However, the porous instead of solid plates were adopted. These plates were prepared in the same way as those in oedometer test presented earlier. In addition, a maximum saturation ratio of 0.9 with a highest wetting duration of 1440 minutes was inputted. The ratio was selected based on the findings of Black & Lee (1973), who investigated the saturation of samples by back pressure for different

soil types. A maximum and minimum cell pressure of 250 kPa and 50 kPa respectively were entered for the application of back pressure under a confining stress of 250 kPa. ASTM D4767-11 reported that the minimum back pressure should be more than 35 kPa and maximum value should not exceed a confining stress. This was to allow the flow of water into a specimen and to avoid repressing it before the commencement of the consolidation phase. The other inputted data remained unchanged as in unsaturated specimens.

4.3.5 Quality Assurance

In oedometer and triaxial, the sets of tests were conducted on specimens with similar density and moisture contents. Therefore, it was imperative to strictly adhere to certain sample preparation measures to eliminate possible errors. This involved the use of the standard methods and calibrated equipment. In addition to this, the following procedures were adopted in both the oedometer and triaxial tests:

- For a group of specimens prepared at equal moisture and density, the same compaction apparatus was used.
- Soil mass per layer was determined by the same calibrated balance.
- Fall height, number of blows and soil layers were also maintained constant, to avoid variation in density.
- Specimens heights and diameters were measured before testing to reject whatever was falling outside the range.
- For triaxial tests, a membrane was thoroughly checked for the presence of perforations, which could lead to uncontrolled entry of water into the sample. The damaged membranes (that is, perforated) were discarded.

The data provided in both Tables 4-4 and 4-5 indicate the height of fall and number of drops that could be used to reproduce the executed tests.

5 Results and Discussion

5.1 Introduction

This chapter presents and discusses both the field work and laboratory test findings. These include profiling of three excavated trial pits (TP01, TP02 and TP03) in Mount Moorosi, field densities, analysis of the results from X-Ray Diffraction (XRS), Scanning Electron Microscope (SEM), free swell, Unconsolidated Undrained Triaxial (CU), slaking and oedometer tests.

5.2 Field Test Results

5.2.1 Trial Pits Observation

Soil profiles were developed based on the field observation and particle size gradation of samples from three excavated trial pits in Mount Moorosi. Profiling was sequentially started from the ground level down to the final depths of pits. The soil description was in accordance with the recommendations of Jennings et al. (1973) which focused on soil moisture condition, colour, consistency, structure, type and origin. It was established that the soil stratification mainly consisted of clayey sandy silt. In addition, no groundwater table was encountered as the excavation was undertaken during a dry period. The profiling of the soil in TP01 is presented in Figure 5-1.

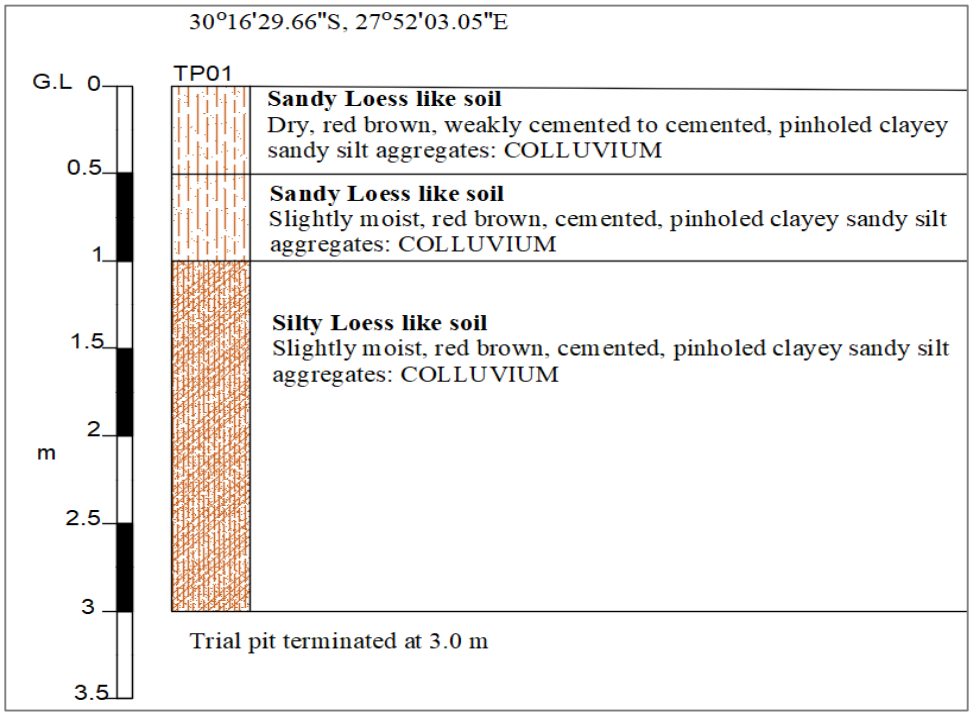

Figure 5-1, A representative soil profile in Mount Moorosi around TP01 locality

At a shallow depth (Figure 5-1), the soil was dry reddish-brown, weakly cemented to cemented, clayey sandy silt (sandy loess) with pinholes. This profile remained homogenous to a depth of 1

m, with variation only in consistency and moisture content. At a deeper level, the slightly moist red-brown cemented pin-holed, clayey sandy silt (silty loess) extended to a depth of 3 m, where the digging was ended with no Tractor Loader Backhoe (TLB) refusal or slower advance. It was observed that the pinholes, visible to a naked eye, generally reduced in number at a deeper depth in all the pits. The South African Pavement Engineering Manual (2014) reported that the pin-holed soil structure is an indication of potentially collapsible soil. Based on the topography and climatic conditions of Mount Moorosi, the noted soil was possibly colluvium deposited by gravity and runoff from the nearby mountain range (Figure 3-2). In fact, Brink (1985) refers to these sediments as transported sandy soils of mixed origin and attributes their deposition predominantly to colluvial processes.

TP02 (Figure 5-2) consisted of dry red-brown, weakly cemented to cemented pin-holed, silty loess from the ground level down to a depth of 0.5 m. It was underlaid by a slightly moist red-brown cemented silty loess, which extended to 2 m depth. This soil overlaid a very dense green to grey intact mudrock; the digging was terminated at this level due to TLB refusal.

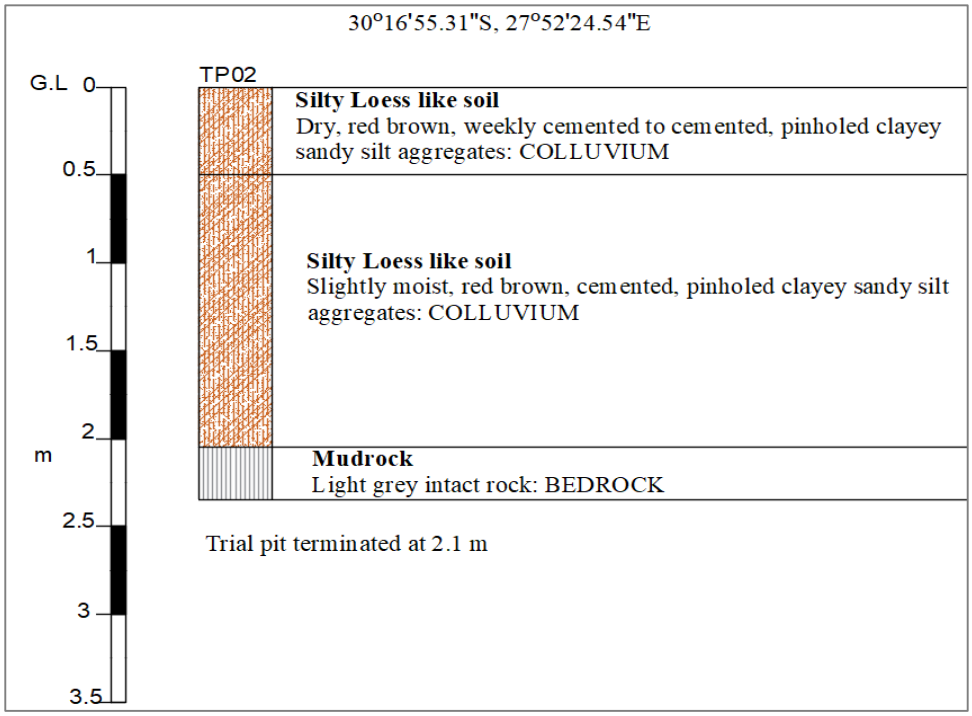

Figure 5-2, A representative soil profile in Mount Moorosi around TP02 locality

In TP03 (Figure 5-3), the dry reddish brown, weakly cemented pin-holed silty loess aggregates were prevalent at a shallow depth. The soil underlaid a slightly moist cemented pin-holed sandy loess that extended to a depth of 2 m. A thin layer of mudrock boulders (0.1 m thick) interbedded both soils at a depth of 0.7 m on one of the four faces of a pit. At a deeper level, the profile changed to slightly moist reddish-brown, cemented pin-holed, silty loess, which continued until the excavation was stopped at 3 m with no TLB refusal.

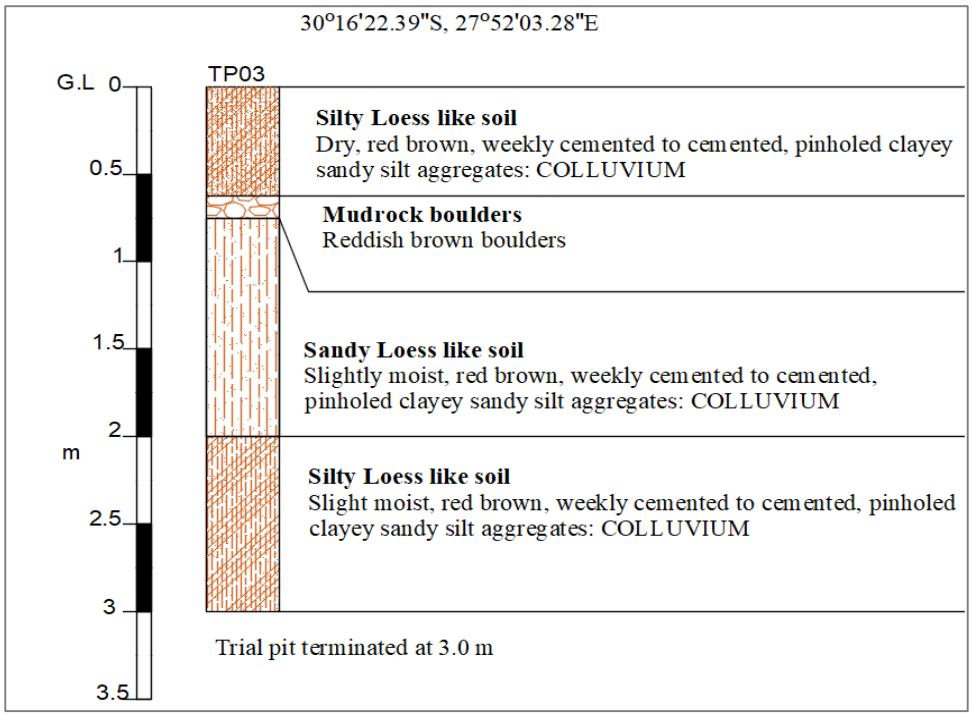

Figure 5-3, A representative soil profile in Mount Moorosi around TP03 locality

5.2.2 Troxler Test Results

Both field and laboratory density tests were conducted by the Civil Engineering Laboratory (PTY) Ltd company in Lesotho. The findings of these tests are summarised in Table 5-1.

Table 5-1, Density test results summary

Troxler test ID	Coordinates	Location	Depth, m	Field properties		Laboratory Tests		Relative compaction, %
				Dry density, kg/m^3	Moisture content, %	Maximum dry density, kg/m^3	Optimum moisture content, %	
TR01	30°16'29.66" S 27°52'03.05" E	Adjacent to TP01	0.3	1681	8.2	1971	9.4	85
TR02	30°16'55.31" S 27°52'24.54" E	Adjacent to TP02	0.3	1878	7.6	2049	8.3	92
TR03	30°16'22.39" S 27°52'03.28" E	Adjacent to TP03	0.3	1833	6.8	2134	8.5	87

The field density and moisture contents were determined specifically for the reconstitution of the disturbed samples in triaxial as well as oedometer tests. It was established that the field dry density ranged from 1681 to 1878 kg/m^3, while the moisture content was from 6.8 to 8.2 % (Table 5-2). Additionally, tests for soil maximum dry density and optimum moisture contents were performed for computation of the soil relative compaction. This is a ratio of the field dry density to the optimum dry density, and was used to assess the degree of soil denseness. Values that varied from 85 to 92 % were obtained. This indicated that the soil was not fully compacted, hence the possibility of settlement under loads. Severe (refer to Table 2-6) water induced settlement was reported by Howayek et al. (2012) in loess deposits of Indiana at a relative compaction of 81 %.

The field densities were similar to those reported in Libya by Anagnostic (1973), and slightly higher than the values noted by Klukanova & Frankovska (1995) in Slovakia (Figure 5-4). The loess from other parts of the world (Saudi Arabia, Iran and Algeria) also demonstrated lower densities. Based on the selected literature, the average in-situ dry density was found to be 1697 kg/m^3.

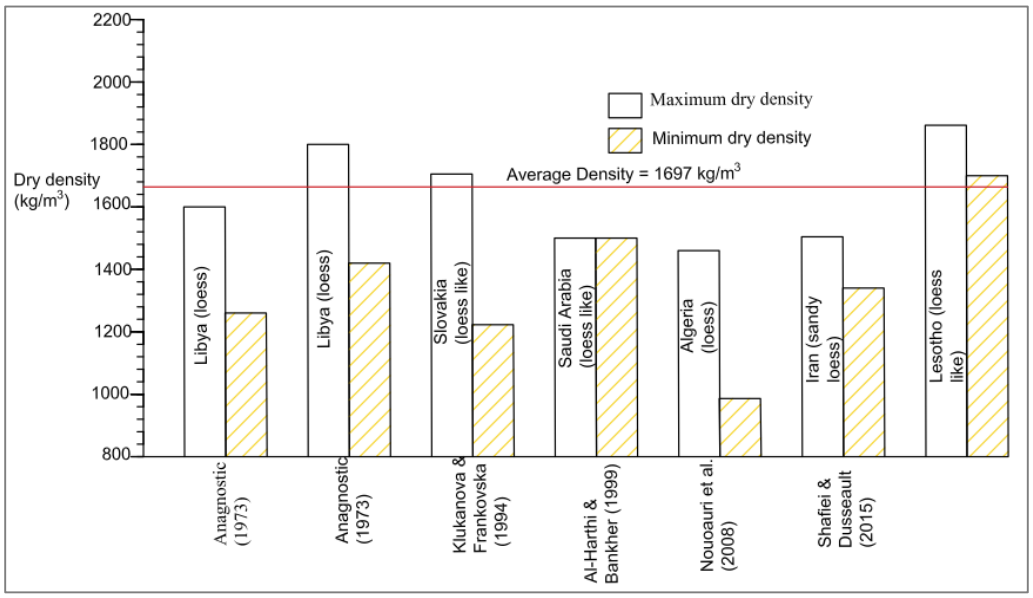

Figure 5-4, Comparison of dry density of loess from different parts of the world (Source: compiled from the literature)

5.3 Laboratory Test Results

5.3.1 Index Tests

Index tests were used to classify and establish the variation of the basic engineering properties of the soil with depth. These included particle size gradation, specific gravity, plasticity limits and free swell index. The potential expansiveness from the ground level down to a depth of 3 m is also estimated and discussed from these properties.

5.3.1.1 Particle Size Gradation

Figure 5-5 demonstrates the measured particle size distribution from different trial pits. In all the tested samples, more than 50 % of the particles passed through a 0.063 mm sieve. The soil was, therefore, generally categorised as fine. The grading envelopes flattened towards the finer particles (end of the spectrum), which consisted of silt and clay in varying proportions. Based on this grading, silt percentage by weight was the predominant grain size (49 to 87 %). The second highest was sand (6 to 32 %), whereas clay had the least composition (5 to 16 %). Owing to this particle gradation, the soil was classified as clayey sandy silt. Similar distributions were reported in loess deposits of Libya as well as Algeria by Assallay et al. (1994) and Nouaouria et al. (2008), respectively. This particle size distribution was used in profiling of excavated trial pits, presented earlier in section 5.2.1.

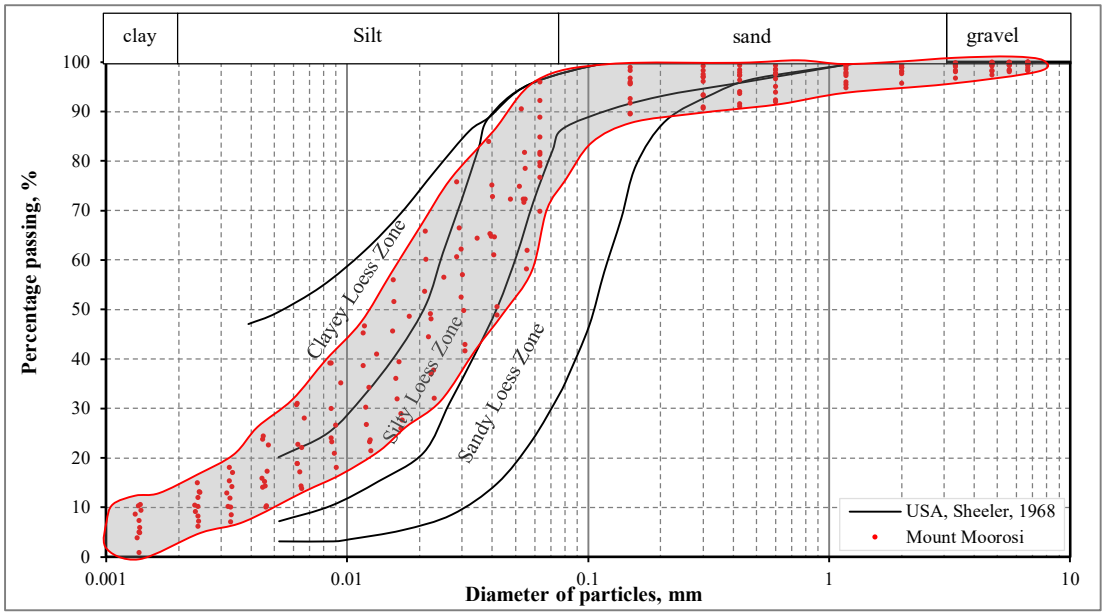

Figure 5-5, Comparison of particle size distribution of Mount Moorosi loess-like soil and USA loess (After Sheeler, 1968)

A comparison of these grading envelopes with particle size gradation curves of loess deposit in the United States of America (USA) (Figure 5-5) showed that the tested soil mostly plotted within the silty zone. However, sand content in some samples was greater than 20 % and this indicated sandy loess (Table 5-2). It should be noted that sand was coarser than that reported by Sheeler (1968). This difference could be ascribed to factors like the mode of weathering, means of particle transportation, or the procedure followed during testing.

According to Pye (1987), a soil can only be regarded as clayey loess when the clay content is more than 20 %, which was not the case in the tested soil. This showed that the soil consisted only of silty and sandy loess like deposits. All determined index properties, including the particle size grading, are summarised in Table 5-2.

Table 5-2, Summary of index tests results from various depths in excavated pits

Trial pit ID	Test no.	Depth, m	< 0.020, mm	0.020 – 0.0630, mm	> 0.075, mm	Specific gravity, g/cm³	Liquid limit, %	Plastic limit, %	Plasticity index, %	Shrink-age limit, %	Free swell, %	UCSC category	Potential expan-siveness, %
TP01	TP01A1	0.00–0.40	16	49	32	2.62	31	16	15	4.60	3	CL	< 2 % Low
	TP01A11	0.40–0.60	10	63	23	2.6	33	16	17	5.04	8		
	TP01A2	0.60–1.00	5	65	26	2.62	27	14	13	3.04	7		
	TP01A3	1.00–2.00	10	81	6	2.61	30	15	15	6.35	0		
	TP01A4	2.00–3.00	10	72	13	2.57	28	13	15	6.01	1		
TP02	TP02B1	0.00–0.40	8	74	16	2.64	27	13	14	5.48	12		
	TP02B11	0.40–0.60	8	78	12	2.65	29	15	14	5.8	10		
	TP02B2	0.60–1.40	14	80	4	2.58	26	15	11	5.41	5		
	TP02B3	1.40–2.10	5	87	8	2.59	25	12	13	4.47	8		
TP03	TP03C1	0.00–0.40	12	65	20	2.56	26	17	9	5.00	3		
	TP03C11	0.40–0.60	12	68	18	2.59	26	14	12	5.66	10		
	TP03C2	0.60–1.00	9	63	25	5.57	27	15	12	4.02	8		
	TP03C3	0.00–0.40	16	49	32	2.62	31	16	15	4.60	3		
	TP03C4	0.40–0.60	10	63	23	2.6	33	16	17	5.04	8		

5.3.1.2 Plasticity Limits

In all tested samples, the plasticity index ranged from 9 to 17 % (Table 5-2), and this indicated low swell potential (Holts & Gibbs, 1956). This indirectly revealed the absence of active minerals like montmorillonite, with a plasticity of over 500 (White, 1942). Figure 5-6 presents the plots of plasticity index versus liquid limit, as per the USCS. Likewise, the categorisation showed that the soil had a low plasticity clay (CL). The recorded liquid and plastic limits were in congruence with the values reported in loessal deposits from the various parts of the world (Figure 5-7).

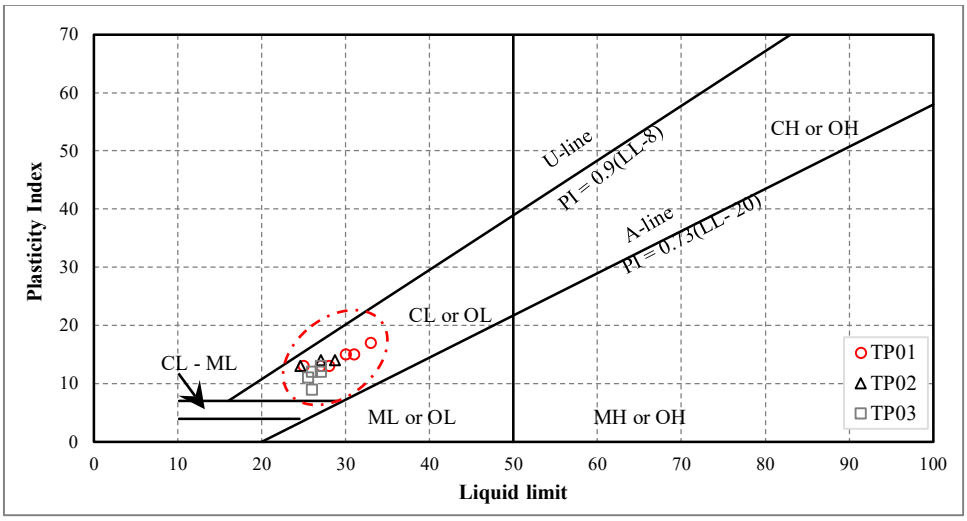

Figure 5-6 Plasticity chart as per USCS (Source: After Das, 2007)

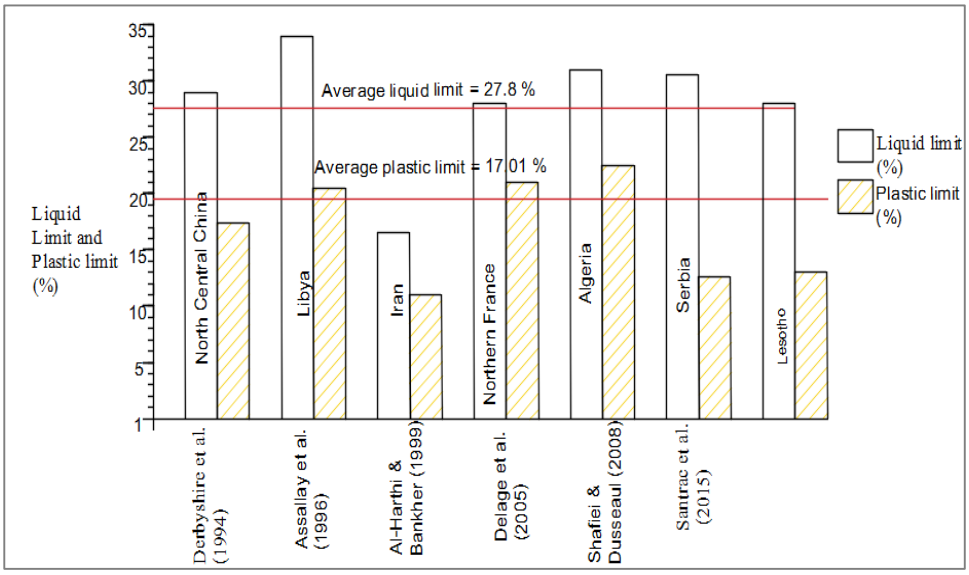

Figure 5-7, Liquid and plastic limits of loessal deposits from different parts of the world (Souce: compiled from different sources)

Figure 5-8 illustrated that clay fraction and plasticity index plotted on the low swell zone of the expansiveness potential chart. This indicated that the volume increase in tested samples was less likely to cause problems to structures. In fact, the measured free swell (Table 5-3) was between

0 and 12 %, which represented low to moderate swell potential (Gibbs and Holz, 1956). The only exception was one outlier from TP01 which plotted on the medium swell potential.

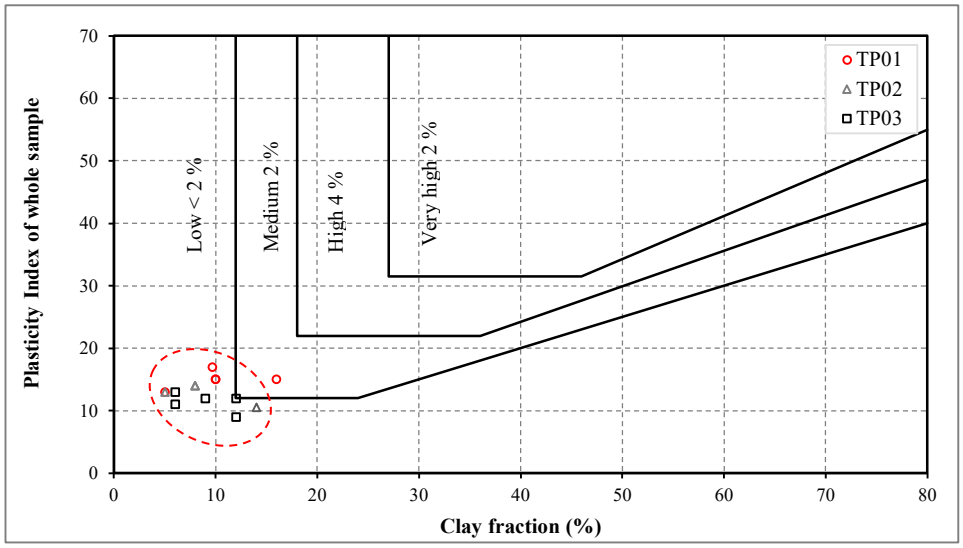

Figure 5-8, Prediction of potential swell in clay soils (Modified from South African Pavement Manual, 2014)

5.3.1.3 Linear Shrinkage

Linear shrinkage varied from 3 to 7 %, that showed non-critical to marginal problems to superimposed structures (Altmeyer, 1955). However, samples demonstrated warping (that is, lifting off at the middle) on drying (Figure 5-9). In specimens that remained intact during shrinkage, the lifting was the highest and ranged from 9.8 to 27.4 mm. Conversely, it was between 1.5 and 8.4 mm for samples that broke into 2 or 3 unequal parts. Similar behaviour was extensively studied by Kodikara et al. (2004) and Puppala et al. (2012), who concluded that the phenomenon was due to differential drying at the top and bottom of tested soil. Puppala et al. (2012) experimental investigation revealed that this type of shrinkage induces pressures that form cracks on the residential buildings and pavements.

Figure 5-9, Warping during linear shrinkage: (a) intact specimen and (b) broken specimen

5.3.2 X-Ray Diffraction

Mineralogy composition is important in the identification of loessal deposits and soil properties such as volume change potential. Minerals were, therefore, determined in samples under investigation. The graphical plots of the measured peak intensities, and the corresponding diffraction angles (2θ) are presented in Figure 5-10. In all samples from various pits, the spectrum showed intensities diffracted by quartz, albite, anorthite, kaolinite, mica, carbonates, sulfate, halide, the oxides and hydroxides of aluminium and iron. The highest diffraction was observed at 2θ ranging from 25 to 35°; this was facilitated by the orientation of the diffracting atomic planes. Certainly, these angles (25 to 35°) corresponded to the orientation of most atomic planes, hence the highest peaks within their range. The peaks became less pronounced with an increase in 2θ until the tests were terminated at 120°. All presented plots in samples from various pits retained a similar pattern, indicating slight variations in the mineralogy composition.

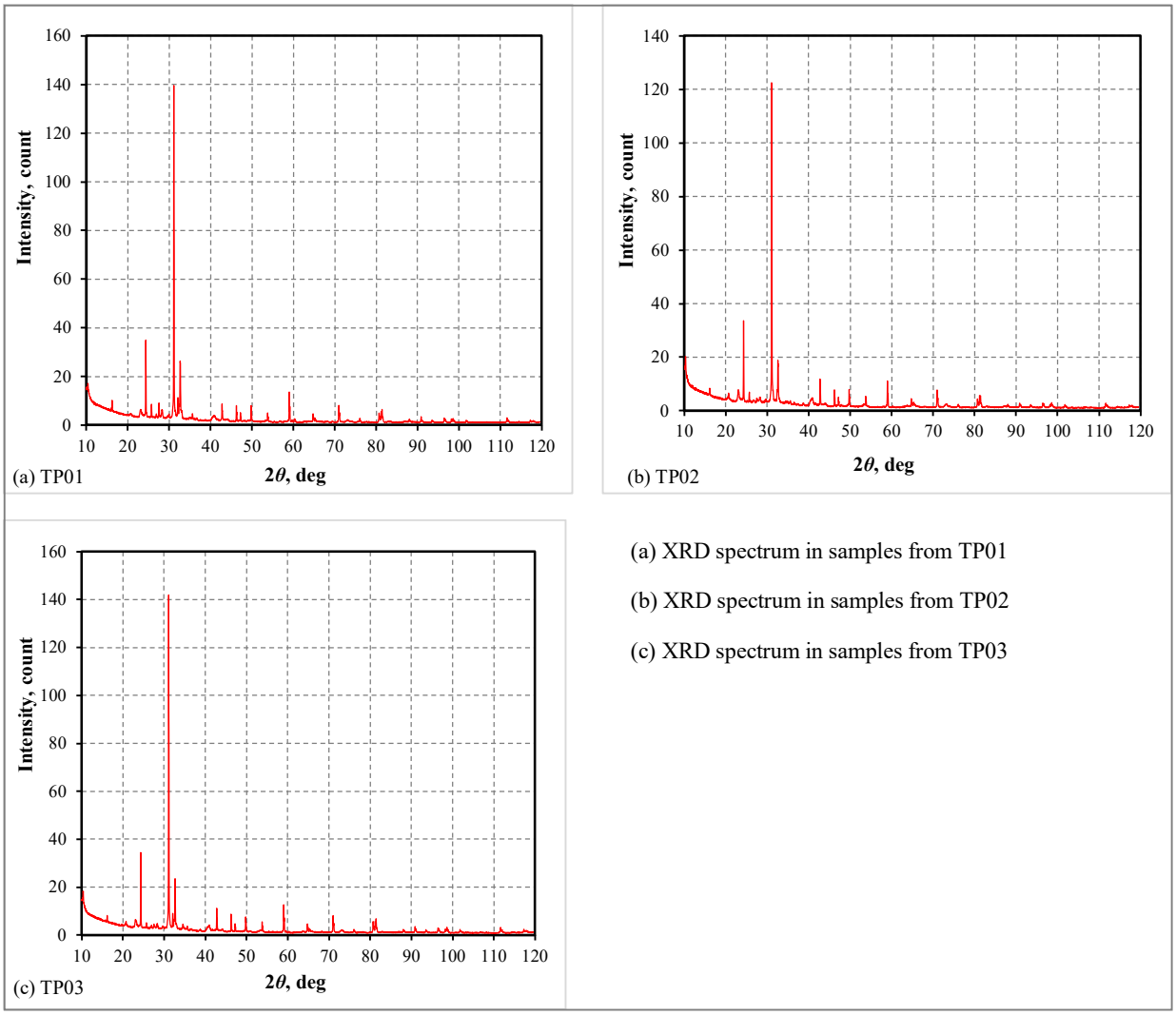

Figure 5-10, XRD intensity against 2θ in samples from the various pits

Table 5-3 indicated that quartz (42.2 %) and feldspar (32.2 %) crystals were the most abundant with a combined total of approximately 75 %. Mica was the third-most prevalent, with a mean value of 12.4 %, followed by kaolinite with an average of 8.0 %. Gibbsite, also a clay mineral building block, inclusive of other soluble minerals (carbonates, sulfate, halide, the oxides and hydroxides of aluminium and iron) made an average of approximately 5.1 %. Although common in loessal deposits, illite was not detected in analysed samples, and this could be associated with the composition of the parent material or the fact that clay minerals are formed under different environments (Grim, 1953). It was clear from this mineral quantification that the Mount Moorosi deposits were sourced from the local outcropping rocks in the Clarens formation, which also consists of quartz, feldspar, calcite and the clay minerals (Rooy & Schalkwyk, 1993). Besides, Johnson et al. (1996) reported that massive loess type deposits were present during the formation of the Clarens landform. The overall quantified percentage of the phase composition conformed with the general estimation made by Engri (1972); Jeong et al, 2011 in loess deposits (Table 2-4).

Table 5-3, Summary of the identified minerals

Trial pit ID	Mineralogy composition, %												
	Quartz	Felspar			Biotite (1M Mica)	Kaolinite (clay)	Soluble minerals						
							Gibbsite (aluminium oxides and hydroxides)	Goethite (iron oxides and hydroxides	Carbonates			Gypsum (sulfate)	Halite (halide)
		Albite	Anorthite	Total					Calcite	Dolomite	Total		
TP01	40.0	14.3	20.2	34.5	12.6	7.7	2.7	0.1	0.8	0.3	1.1	0.6	0.7
TP02	45.7	11.3	19.7	31.0	11.0	7.2	2.1	0.3	1.4	0.1	1.5	0.6	0.6
TP03	40.8	14.0	17.1	31.1	13.7	9.1	3.0	0.1	0.6	0.2	0.8	0.6	0.6

The quantified mineralogy composition was comparable with that of leached loess proposed by Pye (1984) (Table 5-4). In fact, Muggler et al., 2007 and Marcelino et al., 2010 showed that gibbsite (up to 3.0 % in the analysed samples) is formed in highly weathered and leached soils. It precipitates during the dissolution of the primary kaolinite and formation of the secondary kaolinite (Muggler et al., 2007). Krinitzsky & Turnbull (1967) established that the leached loess in Mississippi had higher density than unleached deposits. Similarly, the high densities in the investigated soil could perhaps be attributed to this fractional removal of minerals and subsequent partial collapse.

Table 5-4, Summary of mineralogy composition in loess (Source: Pye, 1984)

Quartz	Feldspar	Calcite	Dolomite	Illite	Kaolinite	Smectite	Chlorite	Gibbsite	Biotite	Other	Location
x	x	x	x	x	x	x	–	–	–	–	Vicksburg, Mississippi
x	x	x	x	x	x	x	x	–	–	–	Nureck, Tajikistan
x	x	x	x	x	x	x	x	–	–	–	Mingtepe, Uzbekistan
x	x	x	–	x	x	–	–	–	–	–	Karhlich, West Germany
x	x	x	–	x	–	–	–	–	–	–	Timaru, New Zealand
x	x	x	x	x	x	–	–	–	–	–	Pegwell Bay, Kent, UK
x	x	x	x	x	x	–	–	–	–	–	Tyszowce, Poland
x	x	x	x	x	x	–	–	–	–	–	Wallertheim, West Germany
x	x	–	–	x	–	–	x	–	x	–	Richardson, Alaska
x	x	x	–	x	x	–	x	–	–	–	Meng Xiang, China (Derbysheri, 1983c)
x	x	x	–	x	–	–	x	–	–	–	Jiuzhoutai, China, (Derbysheri, 1983c)
Leached											
x	x	–	x	x	x	x	–	–	–	–	Vicksburg, Mississippi
x	x	–	x	x	x	x	–	–	–	–	Natchez, Mississippi
x	x	x	–	x	x	–	x	–	–	–	Karamaiden, Tajikistan
x	x	–	–	x	x	–	–	–	–	–	Karhlich, West Germany
x	x	–	–	x	x	–	–	–	–	–	Warneton, Belgium
x	x	–	x	x	x	–	–	–	–	–	Tongrinne, Belgium
x	x	–	x	x	x	–	–	–	–	–	Barton, Hempshire, UK
x	x	–	–	–	x	–	–	x	–	x	Nueva Braunau, Chile
x	x	–	–	–	x	–	–	–	x	–	Mount Moorosi, Lesotho

Halite, a strong soluble salt, had an average of 0.6 %, which was slightly higher than a content of 0.1 % as documented by Yang (1988) in loess deposits. Osipov and Sokolov (1994) estimated that its composition can reach up to 2 %. This shows that loess mineralogical composition varies from one place to another. A study conducted by Raeside (1964) on the loess of South Island, New Zealand, established variation in minerals even from one layer to another, and it was concluded that the difference was enabled by factors such as soil provenance.

Generally, the major active minerals in the tested soil was kaolinite, which coexisted with other soluble trace crystals. However, the composition of the clay content in particle size distribution (5.3.1) was higher than the measured mean quantity of kaolinite (≈ 8 %) in the XRD quantification. This, certainly, showed the presence of other clay-sized particles that were not particularly clay minerals. From this observation, it was inferred that the estimation of the soil swell based on the clay fraction from sieve analysis, could be used for quick swell predictions,

and should be accompanied by the XRD for accuracy. Moreover, a lack of active clays such as montmorillonite can be associated with the low swell potential reported in section 5.3.1. The passive minerals were quartz, feldspar and mica.

5.3.3 Scanning Electron Microscope

The microstructural arrangement of particles within a soil mass has an important influence on the strength, mechanical behaviour and other geotechnical properties of soil (Li et al., 2018). For this reason, the morphology of the identified minerals was crucial. Figures 5-10 through 5-17 depict selected micrographs from evaluated samples. The others are provided in Appendix C. They revealed that the primary grains were a mixture of angular, subangular and platy shaped silt particles, which were cemented by aggregations to form a cohesive fabric. Figure 5-10 demonstrates the sand and silt particles that were bonded to form a structure with both the macropores and micropores.

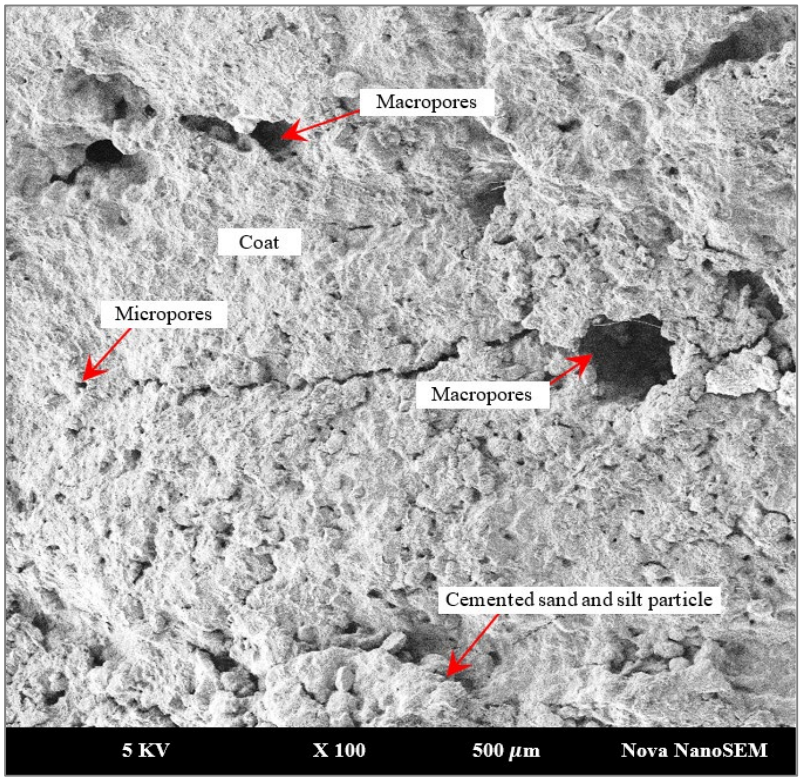

Figure 5-10, SEM-Micrograph showing soil bonding and pores in an intact specimen, TP02

The pores in collapsible soils are referred to as pinholes in the South African Pavement Engineering Manual (2014) and provide a space in which the wetted core grains can settle when loaded. Zhu (1963) attributed the similar pores in Melan loess to plant roots, while Ng et al. (2017) associated them with the accumulation of clay around silt and sand particles. Brink (1985), on the other hand, reported that a porous fabric in transported sandy soils of mixed origin is created by leaching of clay minerals.

Figure 5-11 illustrates a micrograph of two subangular silt particles, bonded and coated by the finer particles. The structure is also analogous to the conceptual model of collapsible loess, proposed by Kie (1986). The platy sharp-edged and randomly orientated quartz particles, also aggregated by finer grains, are demonstrated in Figure 5-12.

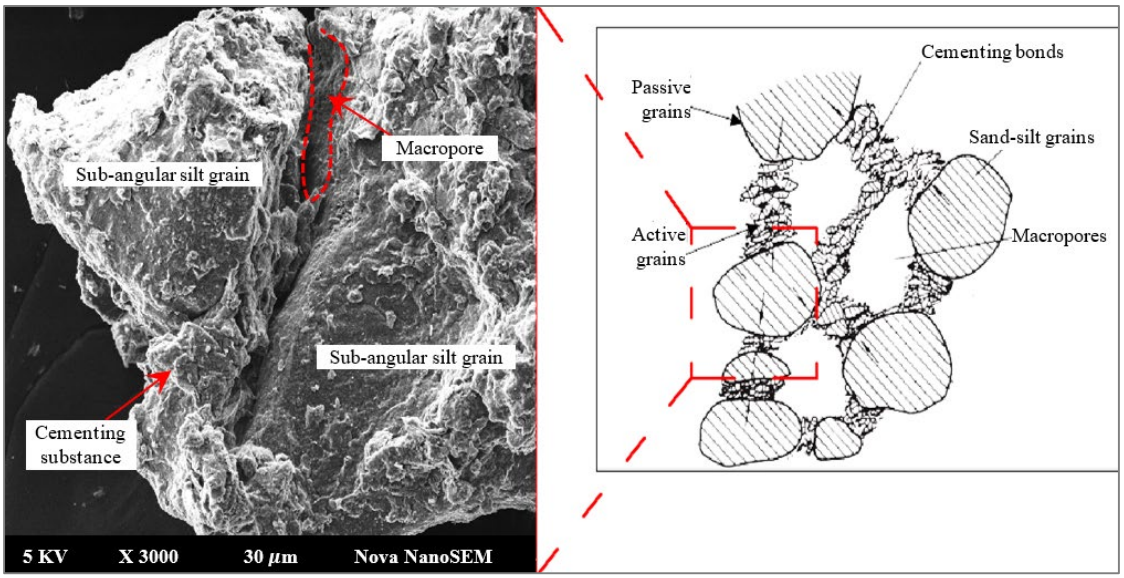

Figure 5-11, SEM-Micrograph showing soil bonding TP01 (Modified from Kie, 1986)

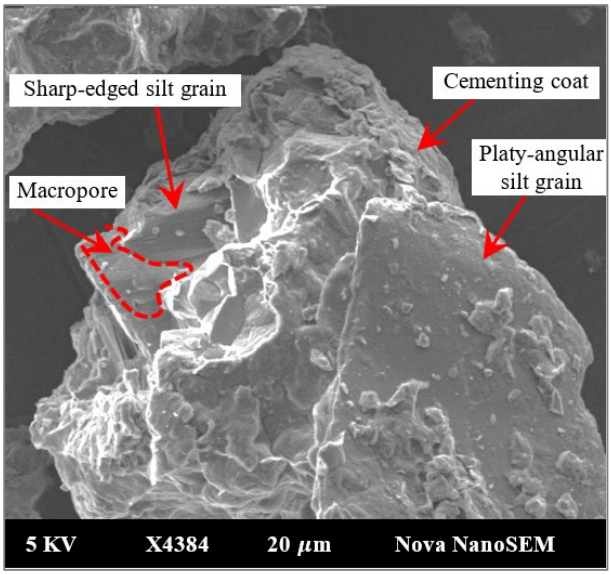

Figure 5-12, SEM-Micrograph of coated quartz particles, TP01

Figure 5-13 demonstrates a micrograph of soil grains that were almost completely submerged by the clay aggregations. It conformed with the idealised structure given in Figure 2-7 (c). The coating and bonding of silt particles was brought about by kaolinite flakes. This relatively thick clothing made direct contact between the primary grains almost impossible. Such a coating is referred to as clay onion skin, and is formed by the authigenesis process in which minerals are

made at the same place where they are found (Barden et al., 1973). The analysed samples were clearly sourced locally.

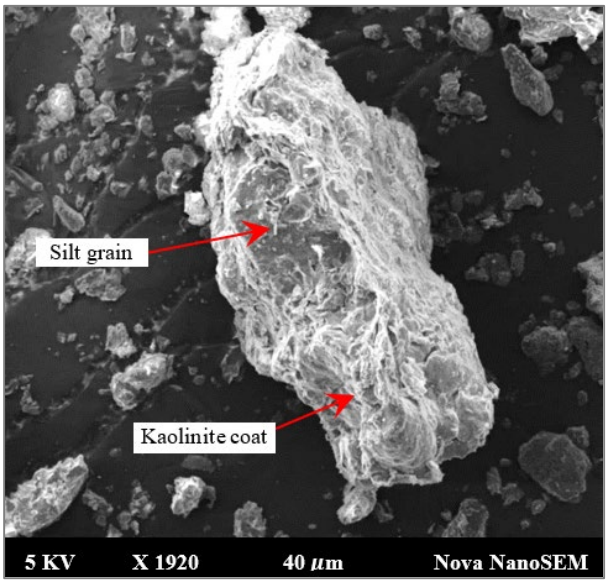

Figure 5-13, SEM-Micrograph of clay onion skin, TP02

Figure 5-14 is a micrograph of silt particles flocculated by kaolinite bridges and other unidentified minerals. Some grains showed intergranular contact, and this could possibly be attributed to an initial partial collapse. Moreover, this structure demonstrated densely packed grains which could be associated with the high measured in-situ densities.

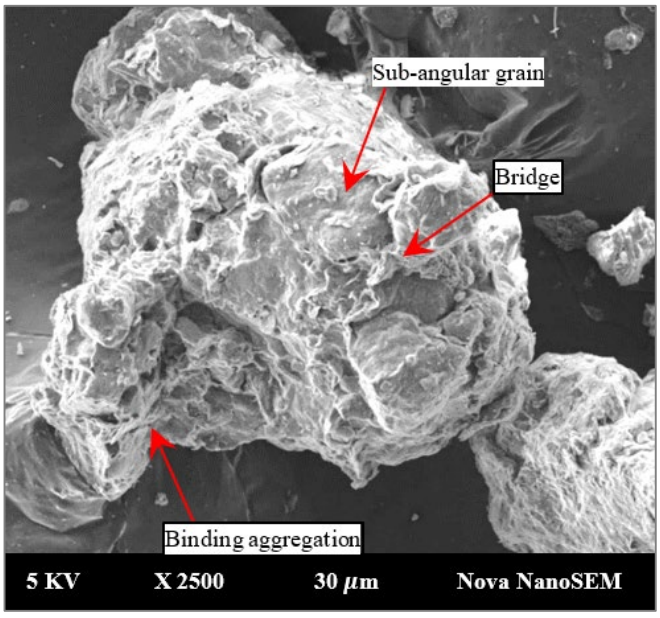

Figure 5-14, SEM-Micrograph of aggregated particles, TP02

Figure 5-15 illustrates the microstructure of the needle fibre calcite crystals and a zoomed section with higher resolution. They coexisted with other minerals, but did not appear to bond the silt

particles. Furthermore, they were randomly distributed as infilling of a pore formed by grains. This type of secondary carbonate is restricted to only loessal and chernozemic soils, that is fertile deposits (Barta, 2011).

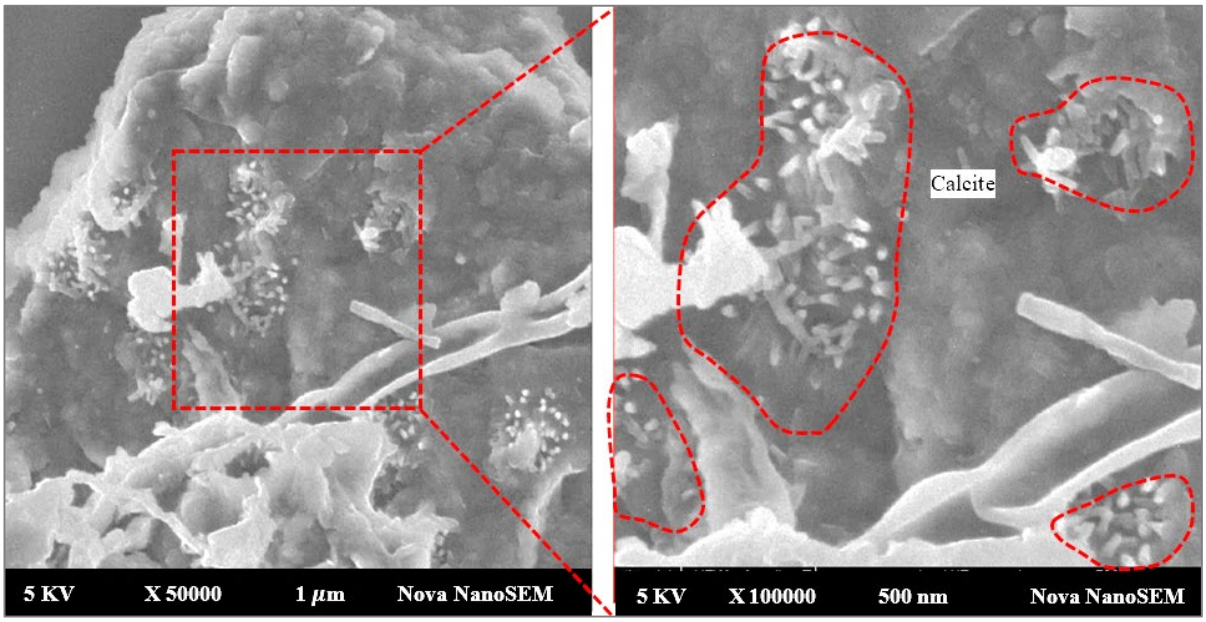

Figure 5-15, SEM-Micrograph of needle fibre calcite, TP01

Figure 5-16 presents the micrographs of the agglomerated kaolinite flakes, which had formed a macropore. These clay flocs cohabited with larger core particles as a filling to inter grain pores. When such a structure is loaded and saturated, the structural collapse of particles into a preformed pore is likely to occur. Figure 5-17 also shows another flocculation of platy particles around a macropore.

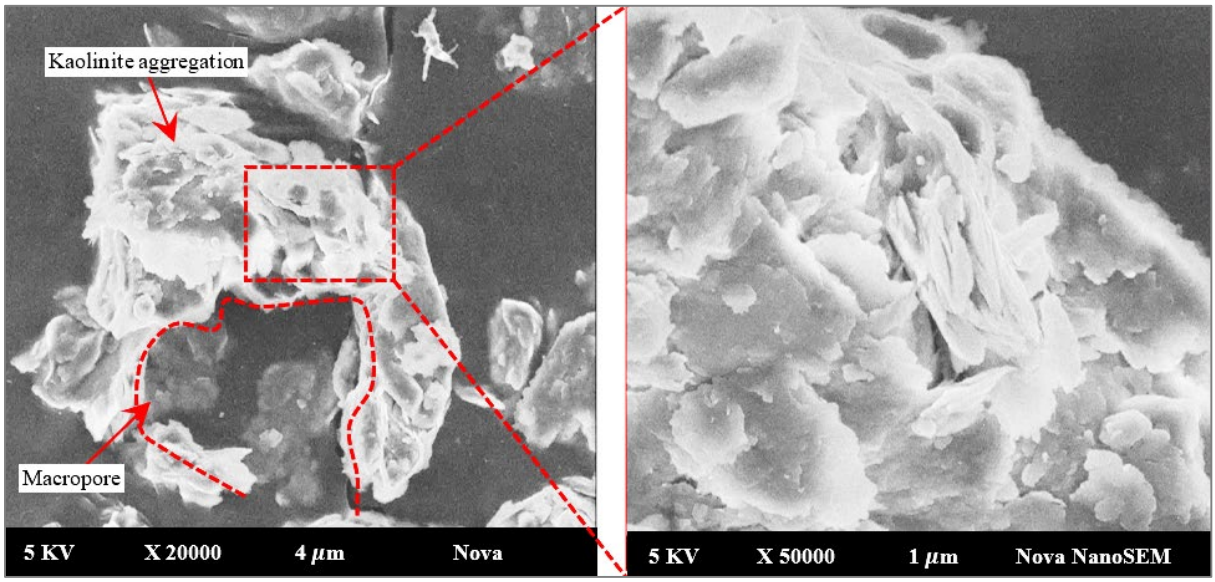

Figure 5-16, SEM-Micrograph of kaolinite aggregation, TP03

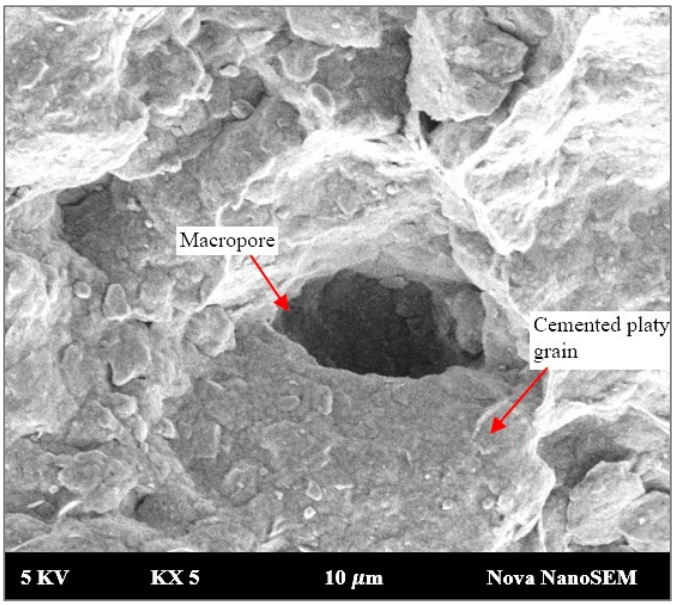

Figure 5-17, SEM-Micrograph of the particles aggregation around a macropore, TP02

A morphological analysis has demonstrated three types of structures that could synergistically enhance the collapse properties of the tested deposits. These included porous clays, silts bonded by clay, and the silts coated with clay, which all render a metastable structure to a soil mass.

5.3.4 Consolidated Undrained Triaxial

The shear strength of clayey sandy silt samples from various pits (TP01, TP02 and TP03) was examined through the execution of a series of consolidated undrained (CU) triaxial tests. The corresponding shear/deviator stress-axial strain graphical plots are presented and discussed. This is followed by an analysis of the respective failure envelopes plotted on Mohr's circles.

5.3.4.1 Deviator Stress-strain Relationship

The soil from each location was compacted at the respective field moisture content and density (Table 5-1) to form several sets of specimens. Some of these specimens were sheared at in-situ moisture content, while the other identical samples were sheared under saturated conditions. Saturated tests were conducted to reflect typical critical state of soil during the rainy period in the field. Understanding this variation in the strength of partly saturated and wet specimens is essential in the design of durable foundations. Figure 5-18 presents the plot of shear stress-strain curves obtained from the CU tests conducted under a series of several confining pressures (50, 100 and 250 kPa). Various stresses provided an important opportunity to assess the behaviour of the soil under diverse applied pressures. All the tests were ended at a maximum strain of 22 %, which was considered adequate to reach the yielding points in triaxial shear testing (BS 1377- 4 -1990).

Shear stress-strain at a natural moisture content

Figures 5-18 (a), 5-18 (c) and 5-18 (e) show the deviator stress-strain graphical plots of specimens from the different pits that were sheared at in-situ moisture content.

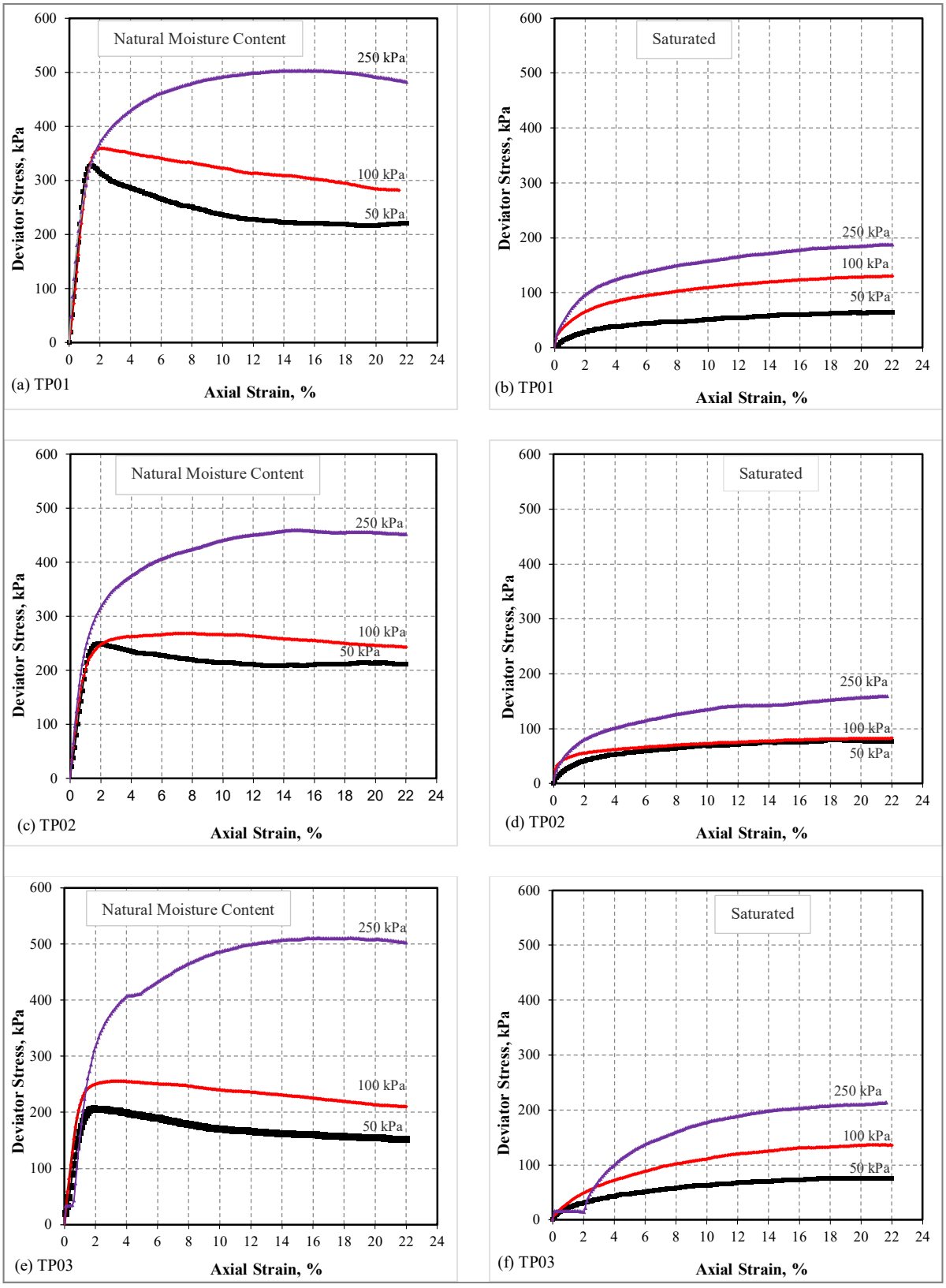

Figure 5-18, Consolidated undrained triaxial plot of deviator stress against axial strain at natural and saturated moisture contents

Generally, under each confining pressure, the deviator stress ($\sigma_1 - \sigma_3$) initially increased rapidly, with small increment in the strain until a peak stress was reached. Beyond the yielding point, the deviator stress slowly decreased as the strain was augmented until the test was terminated. It was also noted that, in all the shear-strain curves, the highest yielding points occurred in large confining stresses, while the lower values produced the least failure stresses. This was attributed to the more particle confinement in the high initial stress state. This improved the area of contact between grains, hence the subsequent shear resistance.

For a confining pressure of 50 kPa, the yield points were well defined and were quickly reached at a strain of approximately 2 % in all the three sets of tests. The highest yielding point was demonstrated in samples from TP01, followed by TP02, whereas TP03 had the least value. Such peaks were attributed to interlocking of densely packed particles and interparticle frictional resistance. It should be noted that for samples under investigation, the clay bonds and cementation also rigidly adhered the particles together (Figure 5-10 to 5-17). This structure had to be overcome to initiate shear mobilisation, thus the grains moved up and over the neighbouring ones (dilation). The shear stress required to resist this dilation was manifested in the form of the peak deviator stress. Once interlocking was reduced, mobility of particles was easy. This caused a gradual reduction in shear stress. The increase in strain towards the end of the tests resulted in an insignificant change in deviator stress, and this indicated a region close to the residual stress.

In all three sets, a confining pressure of 100 kPa formed shear stress-strain curves similar to those produced at a stress of 50 kPa, but with a slightly enhanced axial strain (< 4 %) at the yielding point. From this observation, it can be deduced that the high all-round pressure developed a denser packed soil structure with more resistance to shear stress-induced mobilisation. Consequently, yielding or particles sliding was initiated at higher strains under increased deviator stress. However, the peaks reached at failure were not as well distinct, indicating the possible partial resistance to dilation of grains. Samples from TP01 demonstrated the highest yield point, with the second maximum from TP02, while TP03 had the least value.

Further increase of confining stress to 250 kPa produced a rather smooth curve with no distinct yielding points. This showed that the confining pressure was beyond the yield stress and prevented the dilation of grains during shearing. In such conditions, particles are crushed, and the shear strength is attributed to the subsequent crushing resistance (Bolton, 1986). The highest resistance (shear stress) was in TP03 samples, followed by TP01, whereas TP02 had the lowest. Deviator stress was still decreasing when the tests were terminated for both the confining stresses of 100 and 250 kPa. This was indicative that soil particles were still displacing or deforming with further straining. Consequently, the residual stress (that is, the constant deviator stress) could not be identified within the selected strain range.

Shear stress-strain at saturated condition

In each various sets of tests, the deviator stress-strain curves formed a comparable failure trend when sheared under the saturated conditions (Figure 5-18 (b), 5-18 (d) and 5-18 (f)). Deviator stresses gradually increased as axial strain was amplified until the tests were ended. The maximum final shear stress varied with the confining pressure, and the highest values was observed in 250 kPa, followed by 100 kPa, but 50 kPa had the lowest stress. Like in samples

sheared at natural moisture condition, this variation could be related to the magnitude of the confining stress that influenced the particle contact area, and thus the shear resistance. Among tested samples, the maximum deviator stress was observed in soil from TP03, followed by TP01, conversely, TP02 demonstrated the least value. However, the shear stress-strain curves for all the specimens remained smooth with no apparent yielding points. This pattern was attributed to the development of the pore water pressure during the consolidation and shearing phases, which increased the spaces between the particles. The pore pressure at the commencement of the shearing phase was approximately 2 kPa in all samples tested at field moisture, whereas higher values (beyond 40, 90 and 240 kPa in confining pressures of 50, 100 and 250 kPa, respectively) were noted in saturated tests. The resulting dispersion, therefore, decreased the interparticle contact area, which subsequently reduced the interlocking and friction resistance. Consequently, the mobility of the particles against the shear stress was relatively easy and non-dilative. Under such conditions, the smooth stress-strain curves were formed during shearing. In fact, water is renowned for its tendency to reduce the shear strength of the cementing clay minerals (Liu et at., 2015). Shearing of the soil under low strength of the bonding material (seen in micrographs from Figures 5-10 through 5-17) slowly rearranged core particles to attain a closer packing state that gradually increased the resistance (shear stress) with strain.

The deviator stress at the end of all saturated specimens was, however, drastically lower than that in samples sheared at in-situ moisture content. This variation showed that the shear strength of the deposits was dependent on moisture conditions. At a low moisture content, a high shear stress was required to initiate failure due to the densely packed and cemented particles, while the soil structure was impaired by high pore pressure in saturated conditions.

A summary of the peak and final stresses with the corresponding strains in all tested specimens from various trial pits is presented in Table 5-5. Generally, the mean peak deviator stresses for the samples sheared at natural moisture contents were 260, 294 and 490 kPa for the confining pressures of 50, 100 and 250 kPa, respectively. These corresponded to the strains of 1.8, 2.7 and 15.9 %. The degree of the results deviation was decided based on ASTM E177-14. The deviation between peak deviator stresses was high (> 5 %) due to the different initial moisture contents and compactive effort. On the other hand, the strain deviation was low (< 5 %), which showed that the soil failed at about the similar strain. In specimens sheared under the saturated conditions, the average maximum shear stresses at a final strain were 69, 117 and 194 kPa for confining stresses of 50, 100 and 250 kPa, correspondingly. The high deviation (> 5 %), also associated with the sample preparation, was noted in samples from the various pits.

Table 5-5, The maximum deviator stresses and corresponding strains

Natural moisture content					
Pit ID	**TP01**	**TP02**	**TP03**	**Mean deviator stress, kPa**	**Deviation, %**
Confining stress, kPa	**Maximum deviator stress (corresponding pore pressure), kPa**				
50	326 (1.4)	249 (0.8)	206 (2.2)	260	60.8
100	359 (2.0)	268 (1.8)	256 (0.6)	294	56.3
250	502 (1.5)	460 (1.4)	510 (1.5)	490	26.9
Strain at maximum deviator stress, %				**Mean strain, %**	
50	1.5	2.0	1.9	1.8	0.3
100	2.2	2.5	3.6	4.5	0.7
250	14.4	14.9	18.4	15.9	2.2
Saturated					
Final deviator stress at a strain of 22 % (corresponding pore pressure), kPa				**Mean deviator stress, kPa**	
50	65 (55.7)	67 (33.6)	75 (46.6)	69	5.3
100	129 (95.8)	85 (128.6)	136 (81.1)	117	27.6
250	188 (339.0)	180 (335.2)	213 (298.5)	194	17.2

5.3.4.2 Shear Strength Envelopes

Based on the applied confining pressures and the subsequent peak deviator stresses, Mohr's circles were drawn for each set of samples from the various pits, and the respective failure envelopes were plotted as tangential lines of best fit (Figure 5-19). For saturated tests, with no distinct peak stresses, the final maximum shear stresses were used to draw Mohr's circles.

Mohr's envelopes represent the relationship between the confining pressure and shear stresses. They were, therefore, used to determine the shear strength parameters, which included both the cohesion and friction angle. Generally, all samples from TP01, TP02 and TP03 that were sheared at both the in-situ and saturated moisture contents demonstrated the linear failure envelopes with a gentle slope and an intercept at the vertical axis. The slope of the envelopes was attributed to the friction resistance of the cohesionless grains (sand); hence it represented the friction angle. The intercept, on the contrary, was ascribed to the cohesive nature of soil (clayey silt); thus, it indicated the cohesion parameter of shear strength. The shear strength parameters for all samples are presented in Table 5-6.

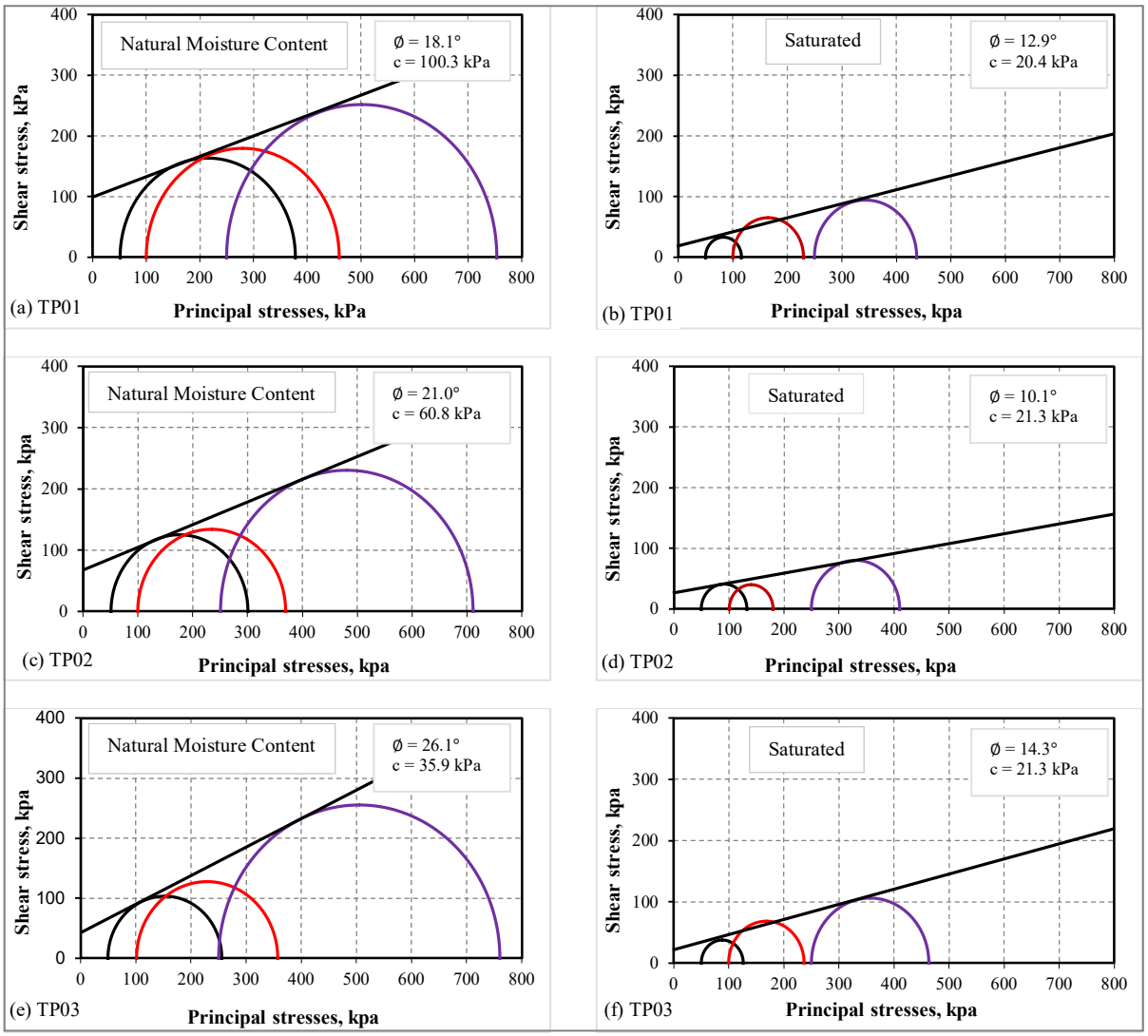

Figure 5-19, Mohr's circles and failure envelop at field moisture content and saturated conditions in samples from the various pits

Table 5-6, Summary of shear strength parameters in tested deposits

Soil properties	TP01	TP02	TP03	Mean values	Standard deviation
Field moisture test condition					
Cohesion, kPa	100.3	61.2	35.9	65.8	32.4
Friction angle, °	18.1	20.5	26.1	21.6	4.1
Moisture content, %	7.8	7.3	6.2	7.2	0.8
Saturated test condition					
Cohesion, kPa	20.4	21.3	21.3	21.0	0.5
Friction angle, °	12.9	10.1	14.3	12.4	2.1
Moisture content, %	15.1	13.5	13.1	13.6	1.1

Shear strength parameters at a natural moisture content

Based on all specimens from the various pits (Figures 5-19 (a), 5-19 (c) and 5-19 (e)) that were sheared at the respective natural moisture content, a mean cohesion of 65.8 kPa was established with a substantial deviation of 32 %. All samples were clayey sandy silt; therefore, the considerable dissimilarity in cohesion was possibly caused by the difference in moisture content. The attractive forces exist between water and negatively charged particle surfaces, particularly clays with the greatest specific surface. Due to this, soil grains are flocculated around water by cation, water-dipole and dipole cation-dipole linkages to form a cohesive matrix which improves the cohesion shear parameter (Lambe, 1953). These interparticle attractive forces are demonstrated in Figure 2-15. Consequently, when moisture content was increased, attraction forces were also augmented, hence the cohesion. Derbyshire et al. (1994) also showed that cohesion in Malan loess was improved with moisture until a threshold corresponding to water at plastic limit was reached. Accordingly, samples from TP01, having the highest moisture content (7.8 %), demonstrated the most considerable cohesion (100.3 kPa). Soil from TP02 with a moisture quantity of 7.3 % exhibited a cohesion of 61.2 kPa, while the least value (35.9 kPa) was noted in TP03 with the lowest amount of moisture (6.2 %).

In all three sets of tests at in-situ moisture content, a mean friction angle of 21.6° was demonstrated, with a permissible deviation of 4.1 % based on ASTM E177-14. It was established that the soil containing the highest amount of water exhibited the least friction angle (18.1°), while the maximum (26.1°) was noted in soil (TP03) with the lowest water content. An intermediate value of 20.5° was noted in soil from TP02, with water quantity of 7.3 %. At relatively high moisture quantity, lubrication in the contact points was the greatest and it subsequently reduced particle friction resistance, hence the smallest friction angle. Contrarily, samples with low water experienced relatively low lubrication, which contributed to higher friction resistance and friction angle. Nevertheless, it is important to point out that other factors, such as particle angularity, surface roughness, gradation, relative compaction and mineralogy composition, also affect the shear strength parameters (Langfelder & Nivargikar, 1967).

Shear strength parameters at a saturated moisture content

Mohr's circles and envelopes of saturated tests of samples from TP01, TP02 and TP03 are presented in Figure 5-19 (b), 5-19 (d) and 5-19 (f), respectively. A mean cohesion of 21 kPa was established with an insignificant deviation of 0.5, which showed that an increase in moisture had similar impact on specimens. Comparison with the cohesion of the soil that was sheared at in-situ moisture revealed a reduction by 68 %, indicating a significant dependency of shear strength on water quantity. Langfelder & Nivargikar (1967) reported that water beyond that in plastic limit state decreased soil cohesion. In fact, it increased interparticle spaces, which in turn undermined the cation, water-dipole and dipole cation-dipole linkages, hence the cohesive forces. Besides, the Van der Waal attraction, which also contributes to cohesion by flocculating the particles, decreased with an increase in distance between the particles. Soil collected from both

TP02 and TP03 produced the same cohesion of 21.3 kPa, while TP01 samples had a slightly lower value (20.4 kPa).

A mean friction angle measured under saturated tests was 12.4°, with a small deviation of 2.1 %. This friction angle showed a reduction of 43 % when compared to tests sheared at field moisture content. This was also due to pore water pressure, which reduced contact area between particles, hence the frictional resistance. The greatest friction angle (14.3°) was noted in specimens from TP03, followed by TP02 (12.9°), whereas TP02 had the least value (10.1°). It is evident from the shear strength parameters obtained in various moisture content that the dissipation of the excess pore water pressure drastically undermined the analysed deposits.

5.3.5 Slaking

Rapid expulsion of air in the form of bubbles was observed during submergence of relatively dense soil lumps in distilled water (Figure 5-20 (a), 5-20 (c) and 5-20 (e)) from TP01, TP02 and TP03. This was followed by the aggregate collapse and reduction in volume. Figures 5-20 (b), 5-20 (d) and 5-20 (f) present the deflocculated aggregates after a submergence period of 10 minutes. The respective slake rate was established in accordance with the suggestions proposed by McMullen (2000).

The fragmentation into grains in a lump from TP03 was reached within 2 minutes. Therefore, it was given a slake rate of 4. The lump from TP01 separated to grains and smaller aggregates within 2 minutes, consequently, it was given a rating ranging from 3 to 4. The soil from TP02 deflocculated into larger angular pieces and grains in 5 minutes of submergence. It was, consequently, given a slake rate of 2 to 3. Several mechanisms that disrupt and weaken the soil fabric and bonds in the slaking process include: the stresses increased by water, rise in pore water pressure, and reduction in soil moisture suction (that is, negative pore pressure) (Glassey, 1986). It was established herein that the rapid dissipation of the entrapped air from pores also disturbed the soil structure.

A study conducted by Glassey (1986) on loess in New Zealand demonstrated that slaking was responsible for erosion and formation of gully tunnels. Furthermore, Liu et at. (2015) highlighted that the collapse triggered by water in loess was rendered by the loss in shear strength of the cementing clay accompanied by slaking. This behaviour was also noted in South Island loess, which had other clay-sized particles that were not clay minerals. It was concluded that they reduced the cohesion of the saturated loess, which resulted in collapse of the soil structure (Jowett, 1995). Accordingly, slake rates measured in tested samples indicated susceptibility to collapse. This inference was further verified in double oedometer tests.

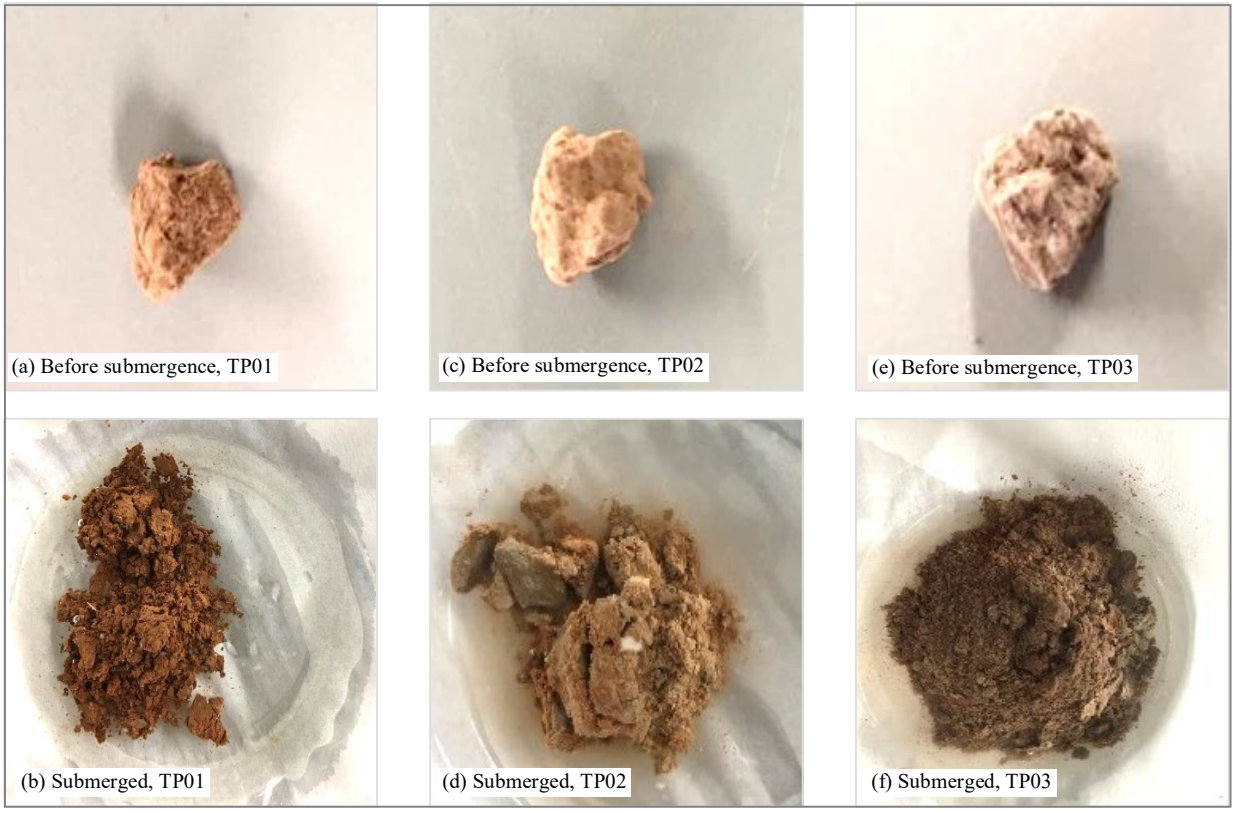

Figure 5-20, Slaking test for samples from the three pits

5.3.6 Double Oedometer

The settlement properties of the samples from TP01, TP02 and TP03 were investigated by conducting double oedometer tests. This involved the use of sets of specimens prepared at the similar density and moisture contents, but tested at differing amounts of water. Some specimens were tested at field water content, while others were saturated. This assisted in understanding the effect of an increase in water of the loaded soil on settlement behaviour. Effective stress-void ratio curves were obtained by applying a series of stresses (6 to 1600 kPa) ranging from minimal up to 10s-fold greater than the stresses from typical buildings (22 kPa) in the study area. This wider range of applied stresses was required to determine the consolidation parameters. The subsequent stress-void ratio graphical plots (Figures 5-21) are presented and discussed. This is followed by the evaluation of the potential hydrocollapse (that is, a water-induced settlement).

5.3.6.1 Effective Stress-Void Ratio Relationship

Effective stress-void ratio relationship: natural moisture content

Figures 5-21 (a), 5-21 (c) and 5-21 (e) present compression curves obtained from oedometer tests at natural moisture contents. Generally, these curves revealed the gradual reduction in void ratio that varied as a function of the applied effective stress level. In fact, the change in void ratio under each applied stress was considerably small when compared to those produced in saturated specimens (Figures 5-21 (b), 5-21 (d) and 5-21 (f)). This resistance to subsidence originated to a greater extent from the structural arrangement of the soil grains and sufficiently high shear

strength (refer to 5.3.4.2). The fabric of the soil (Figure 5-10 to 5-17) had a stable matrix formed by clay cementation of core/passive grains (silt and sand). Shear strength also provided a substantial resistance to particle rearrangement and volume decrease. Additionally, Assallay (2001) established that at low moisture content, clay in cementation and bonds is slightly compressed by the applied pressure without large relative movements. All these characteristics rendered a stable structure with small deformation. The lowest change in void ratio was exhibited by the samples from TP01 due to its high shear strength, which strongly held the particles together against the vertical stresses. Samples from both TP02 and TP03, contrarily, demonstrated a rather higher decrease in void ratio owing to lower shear strength.

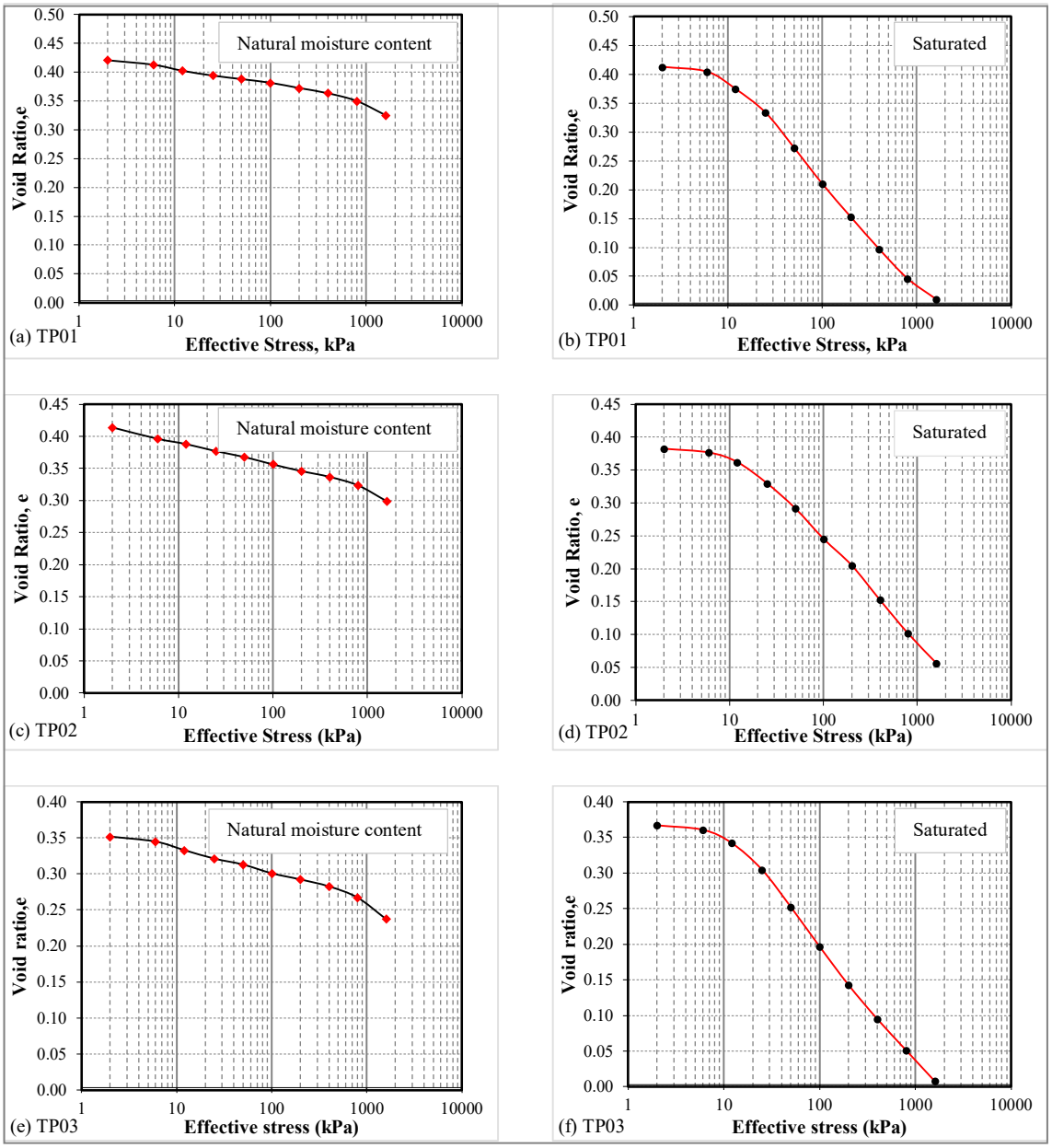

Figure 5-21, Plot of applied stress against void ratio at natural and saturated moisture content in samples from various pits

Effective stress-void ratio relationship: saturated moisture

Figures 5-21 (b), 5-21 (d) and 5-21 (f) show the graphical plots of effective stress against void ratio in samples from three trial pits at saturated test condition. In this case, the reduction in void ratio was significantly greater than that at in-situ moisture tests. The void ratio drastically decreased concurrently with the rise in applied effective stress until the tests were terminated at a final stress of 1600 kPa. This rapid reduction in void ratio was ascribed to the considerable loss in shear strength (5.3.4) that undermined the soil fabric, especially the cohesion in clay cementation and interparticle bonding (5.3.4.2). Assallay (2001) also established that wetted clay bonds in loess deposits act as a system of lubrication to passive silt and sand. This, accordingly, reduced the frictional resistance on the contact points. Moreover, it was established in section 5.3.5 that slaking disrupted the intact, rigid structure of the soil, and triggered collapse. These mechanisms synergistically initiated the mobility, and rearrangement of the loaded particles into a more stable state with reduced volume. Besides, both micropores and macropores (5.3.3) possibly provided a space for loaded and unstable passive particles to settle.

The samples from TP01 demonstrated the greatest settlement. These were followed by TP03, whereas the soil from TP02 had the lowest volume decrease. This variation could be related to factors such as slaking, which was the least in soil from TP02. Essentially, Liu et at. (2015) acknowledged that slaking contributes to the collapse of loess in the oedometer test. However, the literature that correlates this property to hydrocollapse is limited.

5.3.6.2 Soil Hydrocollapse

Santrač et al. (2015) and Yuan-Xun et al. (2013) showed that hydrocollapse is detrimental to overlaid structures. It was, therefore, necessary to study the hydrocollapse susceptibility of the samples under investigation and indicate its magnitude with variation in effective stress. This was achieved by a comparison of the oedometer compression curves from the tests at saturated and natural moisture contents. The subsequent vertical offsets (change in void ratio), as illustrated in Figure 5-22, were used to calculate this collapse. Hydrocollapse was exhibited by the smaller void ratio in saturated curves due to higher settlement than in natural moisture at equal applied pressure. Contrarily, the opposite plot displayed swelling instead of collapsing.

Comparison curves (Figure 5-22 (a) and 5-22 (b)), clearly demonstrate that the rate of change of vertical offset was small under the low effective stress (< 20 kPa), and that it increased with the level of applied pressure. However, the apparent heave, exhibited by a higher void ratio in the saturated graphical plot than that in natural moisture, occurred in samples from TP03 (Figure 5-22 (c)). This showed that the soil volume was increased under low applied pressures. A further rise in magnitude of the effective stress (> 18 kPa) exerted more pressure that counteracted the swell pressure (i.e. the stress induced by soil expansion) and initiated the subsequent collapse. The observed swell was possibly attributed to the kaolinite which was the greatest in samples from TP03 (9 %) but lower in both TP01 (8 %) and TP02 (7 %).

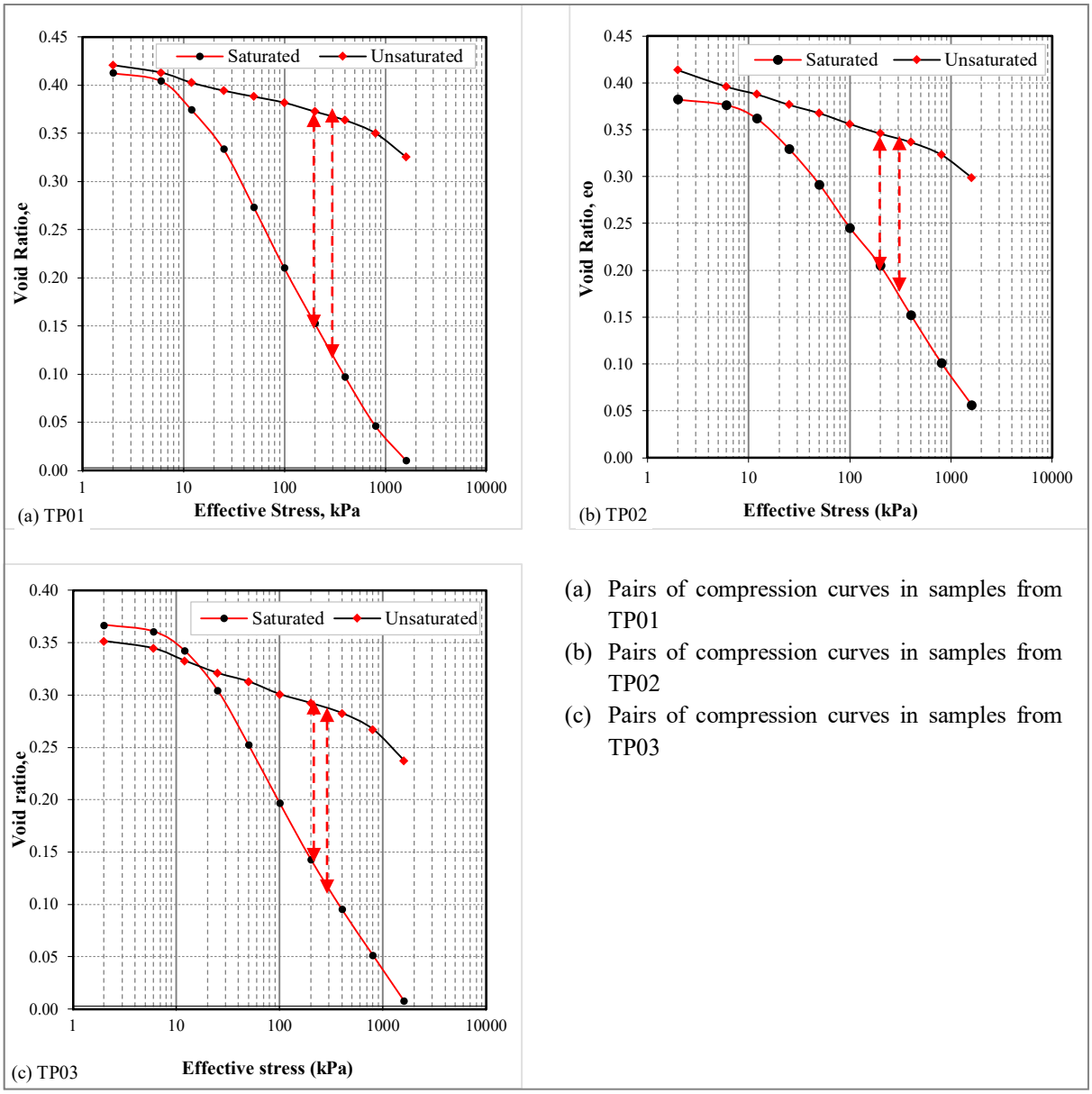

(a) Pairs of compression curves in samples from TP01
(b) Pairs of compression curves in samples from TP02
(c) Pairs of compression curves in samples from TP03

Figure 5-22, Comparison compression curves obtained from double oedometer tests for hydrocollapse determination

ASTM- D5333 – 03 and Lutenegger & Hallberg (1988) proposed equations 2-5 and 2-4, respectively, to correlate the hydrocollapse potential to the offset developed in pairs of the compression curves. Equation 2-5 together with Table 2-5 were used for the determination of the hydrocollapse index based on the effective stress of 200 kPa. Conversely, Equation 2-4 demonstrated the collapse coefficient at an effective stress of 300 kPa. Table 5-7 summarises the water induced settlement computed from these equations for samples from the various pits. In soil from TP01, results showed the magnitude of hydrocollapse ranging from 0.6 to 22.1 %, depending on the level of the applied stress. A degree of hydrocollapse was found to be 15.1 % at a stress of 200 kPa. The collapse varied from 1.6 to 16.6 %, with a value of 9.6 % corresponding to a pressure of 200 kPa in samples from TP02. In soil from TP03, the collapse increased from -

1.2 to 16.6 %, with a value of 10.7 % at a stress of 200 kPa. The negative sign was an indication that the soil was increasing in volume/swelling at low stresses. For all tested samples, an average hydrocollapse was 12 %, with a small deviation of 3 %. Table 2-5 classifies this magnitude of hydrocollapse as severe which indicated that the soil could pose settlement problems to structures.

An average collapse coefficient of 0.15 with a deviation of 0.03 % was found at a stress of 300 kPa. Lutenegger & Hallberg (1988) established that the collapse problems occurred when this coefficient was more than 0.02. This showed that the tested samples were potentially problematic for construction. In specimens from TP01, the coefficient ranged from 0.01 to 0.24, with a value of 0.18 at a pressure of 300 kPa. It increased from 0.02 to 0.19 in samples from TP02, and was 0.14 at a stress of 300 kPa. Conversely, samples from TP03 demonstrated the least value ranging from -0.01 to 0.19, with 0.13 corresponding to a pressure of 300 kPa.

The soil hydrocollapse was caused by the rotational, sliding and translational rearrangement of the loaded grains upon the soft interparticle clay bonds and cement (Assallay, 2001). This mobility was facilitated by the reduced shear resistance in saturated test conditions. It was further augmented by the process of slaking (5.3.5) in which the expulsion of entrapped air disrupted the soil structure. The highest hydrocollapse was exhibited by samples from TP01, whereas TP03 and TP02 had the least comparable values. The large collapse in TP01 was attributed to high variation in shear strength between the specimens at saturated and natural moisture contents which resulted in maximum vertical offset (Figure 5-22).

Table 5-7, Summary of hydrocollapse in samples from TP01, TP02 and TP03

Pit ID	TP01		TP02		TP03		Mean collapse coefficient	Collapse coefficient deviation, %	Mean hydrocollapse, %	Hydrocollapse deviation, %	General remark
Applied stress, kPa	Analysis Methods										
	Collapse coefficient	Hydro-collapse, %	Collapse coefficient	Hydro-collapse, %	Collapse coefficient	Hydro-collapse, %					
6	0.01	0.6	0.02	1.6	-0.01	-1.2	0.01	0.02	0.33	1.42	
12	0.02	2.0	0.02	1.9	-0.01	-0.7	0.01	0.02	1.07	1.53	
25	0.04	4.2	0.03	2.6	0.01	1.2	0.03	0.02	2.67	1.50	
50	0.08	8.0	0.06	5.9	0.05	4.3	0.06	0.02	6.07	1.86	
100	0.12	12.0	0.08	7.6	0.08	7.5	0.09	0.02	9.03	2.57	
200		**15.3**		**9.6**		**10.7**			**11.9**	**3.02**	**> 10 %, severe collapse**
300	**0.18**		**0.14**		**0.13**		**0.15**	**0.03**			**> 0.02, collapse problems**
400	0.2	18.6	0.14	12.6	0.15	13.5	0.16	0.03	14.9	3.24	
800	0.23	21.3	0.17	15.1	0.17	15.5	0.19	0.03	17.3	3.47	
1600	0.24	22.1	0.19	16.6	0.19	16.6	0.21	0.03	18.43	3.18	

The measured average hydrocollapse potential was equal to that of the loess in Libya (12 %) reported by Assallay et al. (1996), and slightly lower than that of loess in Algeria (13 %) established by Nouaouria et al. (2008). This could be related to the high densities of tested samples which offered higher resistance to settlement or the fact that the test conditions were not the same.

Figures 5-23 and 5-24 illustrate the variation of hydrocollapse and collapse coefficients with the applied effective stress. Clearly, the curves flattening at low levels of applied effective stress (that is, from 6 to 12 kPa) indicated small change in collapse rate. The plot of specimens from TP03 was negative at low stresses due to the small swell initiated by higher quantity of kaolinite. Nevertheless, all curves became steep at pressures ranging from 12 to 800 kPa and this showed significant soil collapse. Slight slanting occurred at stresses from 800 to 1600 kPa, which was indicative of the reduction in collapse. This could be associated with the reduced void ratio and a more stable, densely packed soil structure.

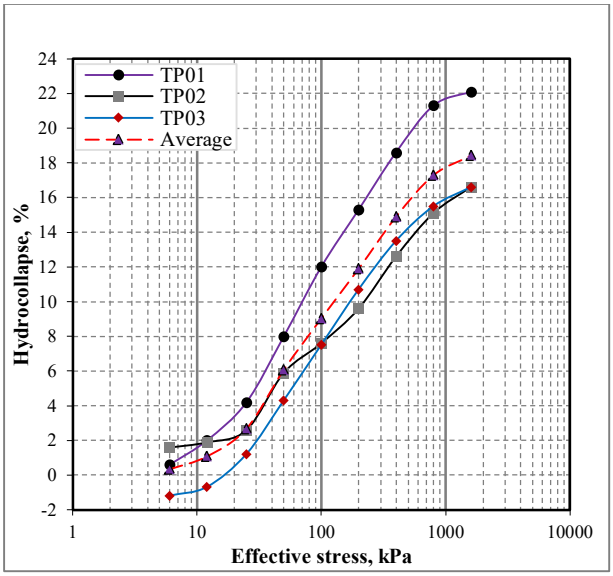

Figure 5-23, Effective stress against a hydrocollapse relationship

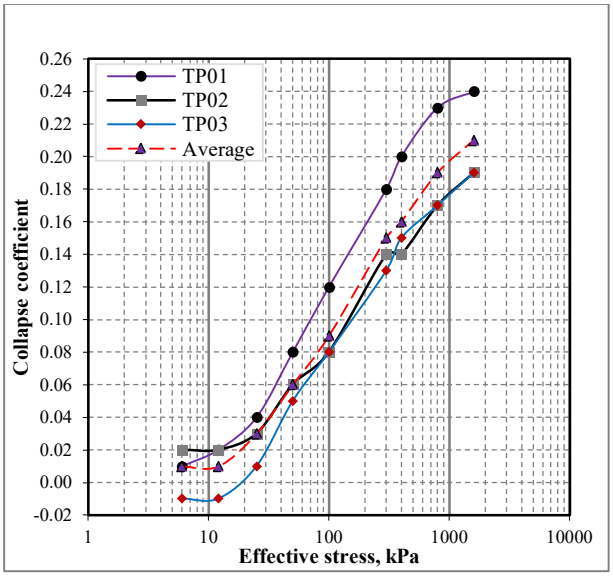

Figure 5-24, Effective stress against collapse coefficient relationship

6 Practical Application

6.1 Introduction

To ensure tolerable limit of the ground and foundation movements, the civil engineering structures are checked against ultimate and serviceability limit states. The former investigates loads that can be sustained by soil prior to shear failure, while the latter is concerned with settlement. Therefore, it was necessary to assess these criteria for a typical structure in the study area using the findings provided in section 5.

This chapter initially presents the loads estimated from a typical house in Mount Moorosi village. This is followed by checking against the Ultimate Limit State (ULS). To evaluate the variation of bearing capacity with change in moisture content, the shear strength parameters obtained from specimens tested at both the field and saturated moisture contents were considered. Finally, the Serviceability Limit State (SLS) due to the actions from the superimposed structures was assessed.

6.2 Loads Used in Practical Application

In both the ultimate and serviceability limit states checks, loads applied by the superimposed structures to the foundation soil were used. They were computed based on the common buildings in the study area. Typical structures constructed in this region are depicted in Figure 6-1. The houses were single storey with two to three bedrooms, a kitchen, sitting room and a verandah, on average. Commonly, the length of each room was 4000 mm, while the width ranged from 3000 to 4000 mm. The roofs were either flat or pitched corrugated iron sheets with timber rafters. They were supported on the load bearing masonry walls, which were constructed mostly with concrete bricks and cement mortar. The height of the superstructure above the ground level was approximately 2500 mm. These buildings were erected on strip footings at a mean depth of 600 mm.

The construction of the houses involved clearing the sites and excavating the foundation trenches (typically 600 mm deep and wide) according to the plan. A 150 mm thick and 600 mm wide blinding was formed by casting concrete on the levelled base of the pit. After the concrete setting period, the brick masonry provided with a brick-force (that is, galvanised wire welded in a ladder pattern) in each course was erected to the ground level. This was followed by masonry plinth which was covered with damp proof polyethylene plastic on the surface. The hollow section of the foundation pit was backfilled and compacted. The masonry wall was laid in stages above the plinth, with brick force at every fourth course. At the specified locations, the door and window frames as well as lintels were installed during construction. On completion of the walls, roofing was placed (that is, the rafters and corrugated iron sheets).

Figure 6-1, Typical houses in Mount Moorosi village (Source: Google map, 2019)

The house plan, sectional view as well as the foundation are respectively presented in Figure 6-2 (a), 6-2 (b) and 6-2 (c). These drawings were developed based on the observed common dwellings in Mount Moorosi residential settlement (Figure 6-1). The founding soil was subjected to permanent and variable vertical loads from structural self-weight and snow, while horizontal actions were induced by wind speed. Permanent loads consisted of the roofing material (that is, timber planks and corrugated iron sheets), masonry walls, foundations and blinding concrete. Table 6-1 summarises the loads exerted per meter length of the strip footing and the corresponding calculations are provided in Appendix D.

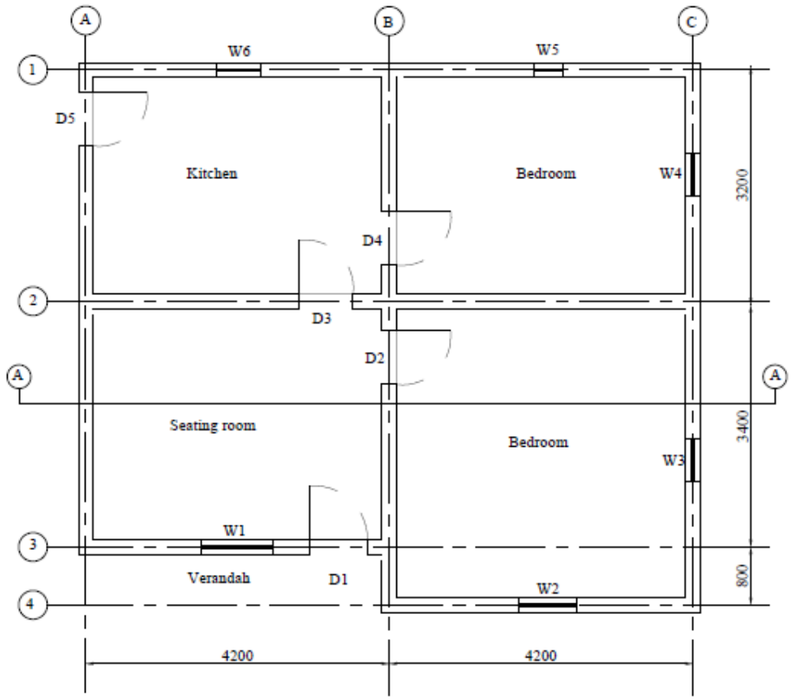

GENERAL LAYOUT PLAN
SCALE 1:100

(a)

DOOR AND WINDOW SCHEDULE	
W1	1000 X 900
W2	800 X 900
W3, W4 & W 6	600 X 900
W5	400 X 600
D1	800 X 1200
D2, D3, D4 & D5	750 X 1200

NOTES
1. All dimensions are in millimeter (mm)
2. All walls are 200 mm wide

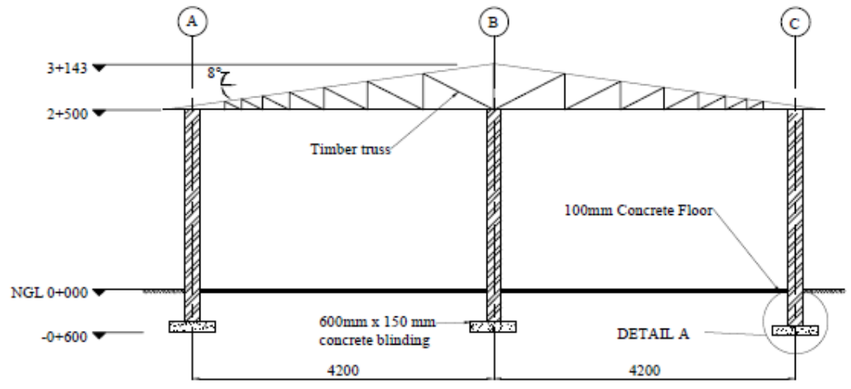

SECTION A-A
SCALE 1:100

(b)

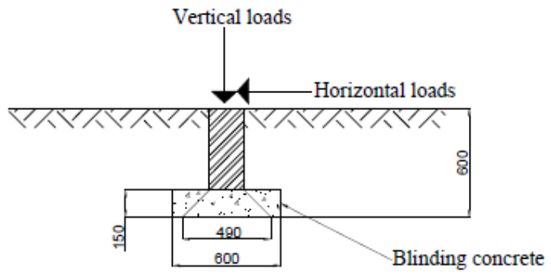

DETAIL A
SCALE 1:50

(c)

-	-	-	-
A	FIRST_EDITION	DM	05/05/19
REV:	DESCRIPTION:	BY:	DATE:

STATUS: RESEARCH

CIVIL ENGINEERING
NEB, MADIBA CIRCLE
UPPER CAMPUS,
RONDEBOSCH
Telephone +27 (0) 21 650 2584
www.civil.uct.ac.za

CLIENT: UCT-GEOTECH-RESEARCH

ARCHITECT: DAMANE_MONICA
MONYAKE_MOTLATSI

SITE: MOUNT-MOOROSI
QUTHING_DESTRICT,LESOTHO

TITLE: TYPICAL_HOUSE

SCALE AT A3:	DATE:	DRAWN:	CHECKED:
AS_SHOWN	2019-05	DM_MSM	PROF._D.K.
RESEARCH NO:	DRAWING NO:		REVISION:
01/2017	G-L		01

Figure 6-2, Plan and sectional view of a typical house in Mount Moorosi village

Table 6-1, Summary of permanent and variable actions

Item	Description	Unit weight, kN/m^3	Reference	Load per meter, kN/m
	Vertical loads, V			
	Permanent actions (unfavourable)			
1	Brickwork	18.9	National code of India, 2005	7.49
2	Blinding concrete	23.0	SANS 10160-2	2.07
	Roofing			
3	Corrugated sheets	0.048 (kN/m^2)	National code of India, 2005	0.05
4	Timber rafters	7	SANS 10160-2	0.07
	Total permanent unfavourable actions			**9.68**
5	Variable vertical actions (unfavourable): Snow loads	3	EN 1991-1-3	**1,01**
6	**Horizontal load: wind (variable, unfavourable), H**	0.976	SANS 10160-3: 2009	**0.052**

6.3 Ultimate Bearing Capacity (ULS)

The ultimate bearing capacity is the maximum pressure from the superstructure, footing self-weight and the overburden, at which soil at the foundation base is expected to fail in shear (Whitlow, 1995). Hansen's expression, modified from the Meyerhof's and Terzaghi's bearing capacity equations, considers the shape, depth, base, ground and load inclination correction factors for footing (Equation 6-1). Therefore, it provides closer correlations to the in-situ ultimate bearing capacity (Shafique & Qayyum, 2016). Consequently, it was adopted in this study. The following assumptions made by Terzaghi during the derivation of the bearing capacity equations were assumed applicable herein:

- The bottom of the footing was adequately rough to resist sliding between the foundation and soil
- The foundation was rigid as compared to the soil
- The soil underlain by the footing was a homogenous semi-infinite mass

$$q_{ult} = c\, N_c\, s_c\, d_c\, i_c\, g_c\, b_c + q\, N_q\, s_q\, d_q\, i_q\, g_q\, b_q + 0.5\, B_\gamma\, N_\gamma\, s_\gamma\, d_\gamma\, i_\gamma\, g_\gamma\, b_\gamma \qquad \textbf{Equation 6-1}$$

Where, c is the cohesion

N_c, N_q and N_γ are the bearing capacity factors

s_c, s_q and s_γ are the shape factors

d_c, d_q and d_γ are the depth factors

i_c, i_q and i_γ are inclination factors

g_c, g_q and g_γ are the ground factors

b_c, b_q and b_γ are the base factors

q is the overburden pressure (γD_f)

B is the foundation breadth

γ is the unit weight.

To ensure the safety of structures, the limit state design method recommended under the Eurocode 7 was followed in the bearing capacity determination. In this method, the partial factors increased the permanent and variable actions, while the material properties were reduced. Additionally, the soil was considered safe against the ultimate limit state if the bearing capacity resistance, R, was greater or equal to the applied action, Q (Equation 6-2).

$$Q \leq R \qquad \textbf{Equation 6-2}$$

$$R = q_{ult} \times B \qquad \textbf{Equation 6-3}$$

6.3.1 Ultimate Bearing Capacity Check Parameters

The check for bearing capacity was based on design approach 1 of the limit state design. This method consists of the following partial factor combinations which factor both the loads and soil properties:

- Combination: A1 + M1 + R1
- Combination: A2 + M2 + R1

Where A, M and R represent the action, material and resistance partial factors, respectively. The partial factors used in the design approach 1 are summarised in Table 6-2.

Table 6-2, Partial factors for design approach 1 (Source: Bond & Harris, 2008)

	Action description	Partial factors				
		A1	A2	M1	M2	R1
Design approach 1	Permanent actions 1. Unfavourable, γ_G 2. Favourable, γ_{Gfev}	1.35 1.00	1.00 1.00	–	–	–
	Variable actions 1. Unfavourable, γ_Q 2. Favourable, γ_{Qfev}	1.50 0.00	1.30 0.00	–	–	–
	Coefficient of shearing resistance (tanϕ), γ_ϕ	–	–	1.00	1.25	–
	Undrained cohesion, γ_{c_u}	–	–	1.00	1.40	–
	Bearing resistance, γ_{R_v}	–	–	–	–	1.00

The properties obtained in soil from various pits at both field and saturated moisture contents were used to conduct a bearing capacity analysis. Partial factors were applied to the actions (Table 6-1) and soil parameters obtained from Table 5-6. These factored parameters are summarised in Table 6-3.

Table 6-3, Summary of factored bearing capacity parameters

Soil properties	TP01	TP02	TP03	TP01	TP02	TP03
Actions (load × partial factors)						
Combination	1			2		
Permanent unfavourable, kN/m	13.07			9.68		
Variable unfavourable, kN/m	1.52			1.31		
Total, Q	14.52			10.99		
Horizontal variable unfavourable, kN/m	0.08			0.07		
Material properties ($\frac{\text{Soil property}}{\text{partial factor}}$)						
Field moisture test condition						
Cohesion, cu, kPa	100.3	61.2	35.9	71.6	43.7	25.6
Friction angle, °	18.1	20.5	26.1	14.5	16.4	20.9
Unit weight, kN/m3	16.5	18.4	18.0	16.5	18.4	18.0
Saturated test condition						
Cohesion, cu, kPa	20.4	21.3	21.3	14.6	15.2	15.2
Friction angle, °	12.9	10.1	14.3	10.3	8.1	11.4
Unit weight, kN/m3	19.0	21.3	20.3	19.0	21.3	20.3

Other parameters required for the computation of the bearing capacity included a foundation depth of 0.6 m. According to the Building Code Interpretation (2008), 06-BCI-014, the load is spread at an angle of 45° from the point of application to the base of a concrete footing. For this reason, a breadth of 0.490 instead of 0.6 m was utilised in the analysis (Figure 6-2 (c)).

6.3.2 Check for Ultimate Bearing Capacity (ULS)

The bearing capacity computation was only done for samples from TP01 since they demonstrated the highest shear strength parameters in tests at natural moisture content and the least values under saturated conditions. This was undertaken to avoid repetition, but the followed check procedure equally applied to all the samples from the various pits.

TP01: UBC for combination 1 at field moisture content

$q_{ult} = c\, N_c\, s_c\, d_c\, i_c\, g_c\, b_c + q\, N_q\, s_q\, d_q\, i_q\, g_q\, b_q + 0.5\, B_\gamma\, N_\gamma\, s_\gamma\, d_\gamma\, i_\gamma\, g_\gamma\, b_\gamma$

$\gamma = 16.5$ kN/m³ $H = 0.08$ kN/m $c = 100$ kN/m²

$Q = 14.5$ kN/m $\phi = 18.1°$ $q = 16.5 \times 0.6 = 9.9$ kN/m²

The horizontal force caused by the wind loads was small and produced a negligible eccentricity (approximately 0.0036). Thus, it was neglected in bearing capacity computation. Table 6-4 presents the bearing capacity factors and the values corresponding to Hansen were used.

Table 6-4, Bearing capacity factors (Source, Kalumba 2019)

∅	Terzaghi's (1943) expression			Hansen, Meyerhoff, and Vesic's expressions		Hansen (1970)	Meyerhoff (1951, 1963)	Vesic (1973, 1975)
	N_c	N_q	N_γ	N_c	N_q	N_γ	N_γ	N_γ
0	5.7	1.0	0.0	5.14	1.0	0.0	0.0	0.0
5	7.3	1.6	0.5	6.49	1.6	0.1	0.1	0.4
10	9.6	2.7	1.2	8.34	2.5	0.4	0.4	1.2
15	12.9	4.4	2.5	11.0	3.9	1.2	1.1	2.6
20	17.7	7.4	5.0	14.8	6.4	2.9	2.9	5.4
25	25.1	12.7	9.7	20.1	10.7	6.8	6.8	12.5
30	37.2	22.5	19.7	30.1	18.4	15.1	15.7	22.4
35	57.8	41.4	42.4	46.4	33.5	34.4	37.6	48.1
40	95.7	81.3	100	75.3	64.1	79.4	93.6	109.3
45	172	173	298	134	135	201	262.3	271.3

Bearing capacity factors obtained from Table 6-4

$N_c = 13.35$

$N_q = 5.45$

$N_\gamma = 2.25$

Shape factors

$L \gg B$ in strip footing ∴ it was assumed that $L \rightarrow \infty$ ∴ $S_c = 1 + \frac{Nq}{Nc}\frac{B}{L} = 1 + \frac{5.45}{13.35}\frac{0.49}{\infty} = 1$

∴ $S_q = 1 + \frac{B'}{L'} \sin \emptyset = 1 + \frac{0.49}{\infty} \sin 18.1 = 1,$ $\quad S_\gamma = 1 - 0.4\frac{B'}{L'} = 1 - 0.4 \times \frac{0.49}{\infty} = 1$

Depth factor

$K = \frac{D}{B} = \frac{0.6}{0.49} = 1.22 > 1$ ∴ k (radians) $= \tan^{-1}(\frac{D}{B}) = \tan^{-1}(\frac{0.6}{0.49}) = 0.87$

$d_c = 1 + 0.87k = 1 + 0.87 \times 1 = 1.87$

$d_q = 1 + 2\tan\emptyset(1 - \sin\emptyset)^2 k = 1 + 2\tan 18.1(1 - \sin 18.1)^2 \times 1.87 = 1.58$

$d_\gamma = 1$

Inclination factors

$$i_q = \left(1 - \left(\frac{0.5\,H}{Q + AfCacot\emptyset}\right)\right)^{\alpha 1} = \left(1 - \left(\frac{0.5x\ 0.08}{14.5 + 0.49 \times \infty \times \frac{2}{3} \times 100 \times \cot 18.1}\right)\right)^2 = 1$$

$$i_c = i_q - \frac{1 - iq}{Nq - 1} = 1 - \frac{1 - 1}{5.45 - 1} = 1$$

$$\theta° = \tan^{-1}\frac{0.08}{14.5} = 0.32° \quad i_\gamma = \left(1 - \left(\frac{\left(0.7 - \frac{\theta}{450}\right)H}{Q + AfCacot\emptyset}\right)\right)^{\alpha 1} = \left(1 - \left(\frac{\left(0.7 - \frac{0.32}{450}\right) \times 0.08}{14.5 + 0.49 \times \infty \times \frac{2}{3} \times 100 \times \cot 18.1}\right)\right)^2 = 1$$

The ground and base are assumed to be level; therefore, all the ground and base factors are equal to 1.

$g_c = b_c = g_q = b_q = g_\gamma = b_\gamma = 1$

$q_{ult} = 100 \times 13.35 \times 1 \times 1.87 \times 1 \times 1 \times 1 + 9.9 \times 5.45 \times 1 \times 1.58 \times 1 \times 1 \times 1 + 0.5 \times 0.49 \times 16.5 \times 2.25 \times 1 \times 1 \times 1 \times 1 \times 1$

$= 2496.45 + 85.25 + 9.10 = 2590.80$ kN/m^2

$R = 2590.8 \times 0.49 \times 1 = 1269$ kN per unit m

$R > Q$ (14.5 kN/m) ∴ **it is safe against ultimate limit state**

TP01: UBC for combination 1 at saturated moisture content

$q_{ult} = cN_cs_cd_ci_cg_cb_c + qN_qs_qd_qi_qg_qb_q + 0.5B\gamma N\gamma s\gamma d\gamma i\gamma g\gamma b\gamma$

$\gamma = 19.0$ kN/m^3 $H = 0.08$ kN/m $c = 20.4$ kN/m^2

$Q = 14.52$ kN/m $\emptyset = 12.9$ ° $q = 19$ x $0.6 = 11.4$ kN/m^2

Bearing capacity factors obtained from Table 6-4

$N_c = 9.88$

$N_q = 3.31$

$N_\gamma = 0.86$

Shape factors

$L \gg B$ ∴ it is assumed that L → ∞ ∴ $S_c = 1 + \frac{Nq}{Nc}\frac{B}{L} = 1 + \frac{3.31}{9.88}\frac{0.49}{\infty} = 1$

∴ $S_q = 1 + \frac{B'}{L'} \sin\emptyset = 1 + \frac{0.49}{\infty} \sin 12.9 = 1$, $S_\gamma = 1 - 0.4\frac{B'}{L'} = 1 - 0.4 \times \frac{0.49}{\infty} = 1$

Depth factor

$K = \frac{D}{B} = \frac{0.6}{0.49} = 1.22 > 1$ ∴ k (radians) $= \tan^{-1}(\frac{D}{B}) = \tan^{-1}(\frac{0.6}{0.49}) = 0.87$

$d_c = 1 + 0.87k = 1 + 0.87 \times 1 = 1.87$

$d_q = 1 + 2\tan\emptyset(1 - \sin\emptyset)^2 k = 1 + 2\tan 12.9(1 - \sin 12.9)^2 \times 1.87 = 1.52$

$d_\gamma = 1$

Inclination factors

$$i_q = \left(1 - \left(\frac{0.5\,H}{Q + AfCa\cot\emptyset}\right)\right)^{\alpha 1} = \left(1 - \left(\frac{0.5 \times 0.08}{14 + 0.49 \times \infty \times \frac{2}{3} \times 20.4 \times \cot 12.9}\right)\right)^2 = 1$$

$$i_c = i_q - \frac{1 - iq}{Nq - 1} = 1 - \frac{1 - 1}{3.31 - 1} = 1$$

$$\theta° = \tan^{-1}\frac{0.08}{14.5} = 0.32° \quad i_\gamma = \left(1 - \left(\frac{\left(0.7 - \frac{\theta}{450}\right)H}{Q + AfCa\cot\emptyset}\right)\right)^{\alpha 2} = \left(1 - \left(\frac{\left(0.7 - \frac{0.32}{450}\right)\text{x}0.08}{14.5 + 0.49\text{x}\infty\ \text{x}\ \frac{2}{3}\text{x}20.4\ \text{x}\ \cot 12.9}\right)\right)^2 = 1$$

The ground and base are assumed to be level; therefore, all the ground and base factors are equal to 1.

$g_c = b_c = g_q = b_q = g_\gamma = b_\gamma = 1$

$q_{ult} = 20.4 \times 9.9 \times 1$ x $1.87 \times 1 \times 1 \times 1 + 11.4 \times 3.31 \times 1 \times 1.52 \times 1 \times 1 \times 1 + 0.5 \times 0.49 \times 19 \times 0.86 \times 1 \times 1 \times 1 \times 1 \times 1$

$= 377.7 + 57 + 4 = 438.7$ kN/m^2

$R = 438.7 \times 0.49 \times 1 = 215$ kN per unit m

$R > Q$ (14 kN/m) ∴ **it is safe against ultimate limit state**

TP01: UBC for combination 2 at field moisture content

$q_{ult} = cN_c s_c d_c i_c g_c b_c + qN_q s_q d_q i_q g_q b_q + 0.5B\gamma N\gamma s\gamma d\gamma i\gamma g\gamma b\gamma$

$\gamma = 16.5$ kN/m^3 $H = 0.07$ kN/m $c = 71.6$ kN/m^2

$Q = 11$ kN/m $\emptyset = 14.5$ ° $q = 16.5$ x $0.6 = 9.9$ kN/m^2

Bearing capacity factors obtained from Table 6-4

$N_c = 10.73$

$N_q = 3.76$

$N_\gamma = 1.12$

Shape factors

$L \gg B$ ∴ it is assumed that $L \to \infty$ ∴ $S_c = 1 + \frac{Nq}{Nc}\frac{B}{L} = 1 + \frac{3.76}{10.73}\frac{0.49}{\infty} = 1$

$\therefore S_q = 1 + \frac{B'}{L'} \sin \emptyset = 1 + \frac{0.49}{\infty} \sin 14.5 = 1, \qquad S_\gamma = 1 - 0.4 \frac{B'}{L'} = 1 - 0.4x \frac{0.49}{\infty} = 1$

Depth factor

$K = \frac{D}{B} = \frac{0.6}{0.49} = 1.22 > 1 \therefore k \text{ (radians)} = \tan^{-1}(\frac{D}{B}) = \tan^{-1}(\frac{0.6}{0.49}) = 0.87$

$d_c = 1 + 0.87k = 1 + 0.87 \text{ x } 1 = 1.87$

$d_q = 1 + 2\tan\emptyset(1 - \sin\emptyset)^2 k = 1 + 2\tan 14.5(1 - \sin 14.5)^2 \text{ x } 1.87 = 1.54$

$d_\gamma = 1$

Inclination factors

$$i_q = \left(1 - \left(\frac{0.5\,H}{Q + AfCacot\emptyset}\right)\right)^{\alpha 1} = \left(1 - \left(\frac{0.5x\ 0.08}{11 + 0.49 \times \infty \times \frac{2}{3} \times 71.6 \times \cot 14.5}\right)\right)^2 = 1$$

$$i_c = i_q - \frac{1 - i_q}{N_q - 1} = 1 - \frac{1 - 1}{3.76 - 1} = 1$$

$$\theta° = \tan^{-1}\frac{0.07}{11} = 0.36° \qquad i_\gamma = \left(1 - \left(\frac{\left(0.7 - \frac{\theta}{450}\right)H}{Q + AfCacot\emptyset}\right)\right)^{\alpha 2} = 1 - \left(\frac{\left(0.7 - \frac{0.36}{450}\right) \times 0.07}{11 + 0.49 \times \infty \times \frac{2}{3} \times 71.6 \times \cot 14.5}\right)^2 = 1$$

The ground and base are assumed to be level; therefore, all the ground and base factors are equal to 1.

$g_c = b_c = g_q = b_q = g_\gamma = b_\gamma = 1$

$q_{ult} = 71.6 \times 10.73 \times 1 \times 1.87 \times 1 \times 1 \times 1 + 9.9 \times 3.76 \times 1 \times 1.54 \times 1 \times 1 \times 1 + 0.5 \times 0.49 \times 16.5 \times 1.12 \times 1 \times 1 \times 1 \times 1 \times 1$

$= 1436.7 + 57.3 + 4.5 = 1498.5 \text{ kN/m}^2$

$R = 1498.5 \times 0.49 \times 1 = 734.3 \text{ kN per unit m,}$

$R > Q$ (14 kN/m) $\therefore$ **it is safe against ultimate limit state**

limit state

TP01 Case 1: UBC for combination 2 at saturated moisture content

$q_{ult} = cN_c s_c d_c i_c g_c b_c + qN_q s_q d_q i_q g_q b_q + 0.5B\gamma N\gamma s\gamma d\gamma i\gamma g\gamma b\gamma$

$\gamma = 19.0 \text{ kN/m}^3$ $H = 0.07 \text{ kN/m}$ $c = 14.6 \text{ kN/m}^2$

$Q = 11 \text{ kN/m}$ $\emptyset = 10.3°$ $q = 19 \text{ x } 0.6 = 11.4 \text{ kN/m}^2$

Bearing capacity factors obtained from Table 6-4

$Nc = 8.35$

$N_q = 2.6$

$N_\gamma = 0.4$

Shape factors

$L \gg B \therefore$ it is assumed that $L \to \infty \therefore S_c = 1 + \frac{Nq}{Nc}\frac{B}{L} = 1 + \frac{2.6}{8.35}\frac{0.49}{\infty} = 1$

$\therefore S_q = 1 + \frac{B'}{L'} \sin \emptyset = 1 + \frac{0.49}{\infty} \sin 10.3 = 1, \quad S_\gamma = 1 - 0.4\frac{B'}{L'} = 1 - 0.4 \times \frac{0.49}{\infty} = 1$

Depth factor

$K = \frac{D}{B} = \frac{0.6}{0.49} = 1.22 > 1 \therefore k$ (radians) $= \tan^{-1}(\frac{D}{B}) = \tan^{-1}(\frac{0.6}{0.49}) = 0.87$

$d_c = 1 + 0.87k = 1 + 0.87 \text{ x } 1 = 1.87$

$d_q = 1 + 2\tan\emptyset(1 - \sin\emptyset)^2 k = 1 + 2\tan 10.3(1 - \sin 10.3)^2 \times 1.87 = 1.46$

$d_\gamma = 1$

Inclination factors

$i_q = (1 - (\frac{0.5\,H}{Q + AfCacot\emptyset}))^{\alpha 1} = (1 - (\frac{0.5\text{x } 0.07}{11 + 0.49 \text{ x } \infty \text{ x } \frac{2}{3}\text{x } 14.6 \text{ x } \cot 10.3}))^2 = 1$

$i_c = i_q - \frac{1 - i_q}{N_q - 1} = 1 - \frac{1-1}{3.31-1} = 1$

$\theta° = \tan^{-1}\frac{0.07}{11} = 0.36° \quad i_\gamma = \left(1 - \left(\frac{\left(0.7 - \frac{\theta}{450}\right)H}{Q + AfCacot\emptyset}\right)\right)^{\alpha 2} = \left(1 - \left(\frac{\left(0.7 - \frac{0.36}{450}\right) \times 0.07}{11 + 0.49 \times \infty \times \frac{2}{3} \times 20.4 \times \cot 10.3}\right)\right)^2 = 1$

The ground and base are assumed to be level; therefore, all the ground and base factors are equal to 1.

$g_c = b_c = g_q = b_q = g_\gamma = b_\gamma = 1$

$q_{ult} = 14.6 \times 9.9 \times 1 \times 1.87 \times 1 \times 1 \times 1 + 11.4 \times 2.6 \times 1 \times 1.46 \times 1 \times 1 \times 1 + 0.5 \times 0.49 \times 19 \times 0.4 \times 1 \times 1 \times 1 \times 1 \times 1$

$= 270 + 43.3 + 1.9 = 315 \text{ kN/m}^2$

$R = 315 \times 0.49 \times 1 = 154$ kN per unit m

$R > Q$ (11 kN/m) $\therefore$ **it is safe against ultimate limit state**

Table 6-5 summarises the soil ultimate bearing capacity in all assessed combinations. Generally, the natural moisture content condition, having higher shear strength parameters provided large bearing values in both combinations 1 and 2. However, the bearing capacity was higher in combination 1 than in 2 because of lower adopted material partial factors. The saturated

conditions, with relatively low shear strength parameters, drastically reduced the ultimate capacity by nearly 80 %. Though the change in bearing capacity was substantial, it was still greater than the applied load and adequate to guard against the ultimate limit state.

Table 6-5, Summary of ultimate limit state check

Design approach 1	Combinations	Vertical action, kN/m	Allowable load, kN/m	Vertical action, kN/m	Allowable load, kN/m	Potential failure against ULS
		Field moisture condition		Saturated moisture condition		
	1	14.5	1269	14.5	215	Safe
	2	11	734	11	154	

Kalpakci (2017) reported a settlement that caused tilting and cracks on a cement plant in Azerbaijan. The structure was designed against the bearing capacity and not serviceability limit state. Consequently, the check for settlement was also conducted for the samples tested in this study to avoid the unforeseen ground movements.

6.4 Settlement Analysis (SLS)

Generally, the vertical reduction in volume pertaining to mechanisms such as deformation of soil structure or expulsion of either air or water from the pores is referred to as settlement. The findings presented in 5.3.6 showed substantial water induced collapse, which could trigger settlement problems on the infrastructure. Slight ground displacement results in damage in the form of cracks due to the brittle nature of the masonry bricks (Whitlow, 1995). It was, therefore, important to assess the degree of potential settlement caused by the construction of a typical house in the study area.

6.4.1 Settlement Analysis Using Settle 3D Software

Settle 3D programme is a package of Rocscience software used for the analysis of settlement from applied civil engineering structural loads (foundations, embankments or excavations). Its capability to demonstrate in 3-dimensional the stress distribution caused by the rectangular, circular or polygonal loadings and corresponding settlement makes it the world's leading programme for soil volume decrease analysis (Geotechnical Tools, 2019). The Westergaard, Vertical Ratio (2:1, angle), Boussinesq and Multiple Layer are approaches used to assess both stress variation with depth and subsequent settlement. Nevertheless, owing to the parameters that were investigated in this study, the Boussinesq Method was most appropriate. This method uses Equation 6-4 for the calculation of the soil vertical pressures, σ_z, under a strip pressure, Q_S, with breadth B (refer to Figure 6-3).

$$\sigma_z = \frac{Q_s}{\pi}(\theta + \sin\theta) \qquad \textbf{Equation 6-4}$$

$$\theta = 2tan^{-1}(\frac{\frac{B}{2}}{z}) \qquad \textbf{Equation 6-5}$$

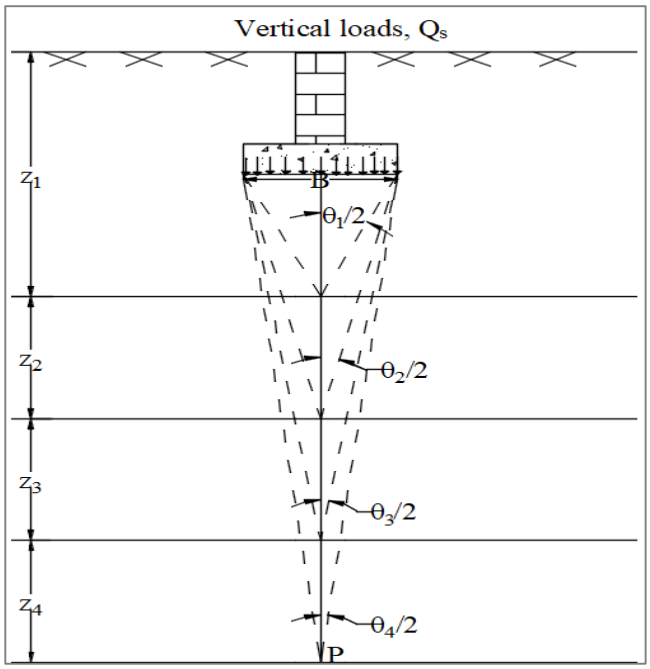

Figure 6-3, A conceptual model for decrease in pressure distribution below a strip load, based on the Boussinesq theory

The Boussinesq Method considers the exerted pressure intensity below the centre of a strip footing as decreasing with depth, as illustrated by the dotted lines in Figure 6-2. The evaluation of pressure distribution involves dividing the soil stratum into smaller sub-layers to determine the change in vertical stress at the centre of each layer (that is, z_1 to z_4 for an example demonstrated in Figure 6-3). The total stress, σ, at point P is given by the mean effective soil pressure, σ_0, and increment, $\int_1^4 \Delta\sigma$, due to surcharge.

Once the pressures have been computed, Equation 6-6 is used for the corresponding settlement deterministic calculation, in which the subsequent void ratios are obtained from the effective stress-void ratio graphical plot.

$$S = \frac{e_0 - e_1}{1 + e_0} H \qquad \textbf{Equation 6-6}$$

Where, e_o is a void ratio at a vertical soil pressure, σ_0, before the surcharge was applied

e_1 is the new void ratio due to pressure increment, $\Delta\sigma$

H is the thickness of the soil stratum

After settlement has been computed, query points and graphs were used to display and report volume decrease magnitude. The Eurocode 7 does not apply the partial factors in the check for serviceability limit state. However, it regards the SLS to be satisfied if settlement does not exceed 50 mm. Conversely, the South African Home Building Manual (2014) allows for a maximum settlement of 20 mm on residential buildings with no basement. Subsidence beyond these values poses damage to brittle structures.

6.4.2 Settlement Check Parameters

A settlement check analysis was conducted for a typical house in the study area (Figure 6-2), based on the loads summarised in Table 6-1. AccuWeather (2019) reported a rainfall in consecutive days in Mount Moorosi. Therefore, to simulate the long inundation periods, the water table was assumed to vary from the ground surface down to the pit final depth. It was also presumed that the thickness of the soil stratum was equivalent to that observed in trial pits (section 5.2.1) and was underlaying a bedrock. In fact, the deeper depths were outside the zone of influence of the applied pressure (three times the base). The effective stresses and the corresponding hydrocollapse (refer to Table 5-7), level of water table and the quantity of the applied pressure were inputted into the settle 3D program. The following average values were adopted:

- Depth of footing, D = 0.6 m
- Breadth of footing, B = 0.49 m
- Pressure from the building, $Q_s = \frac{\text{Load per unit meter}}{\text{breadth}} = \frac{10.69}{1 \text{ x } 0.49} = 21.8$ kN/m^2
- Unit weight: TP01 = 16.5 kN/m^3, TP02 = 18.4 kN/m^3, TP03 = 18.0 kN/m^3
- Saturated unit weight: TP01 = 19.0 kN/m^3, TP02 = 21.3 kN/m^3, TP03 = 20.6 kN/m^3
- Stratum thickness: TP01 = 3.0 m, TP02 = 2.1 m, TP03 = 3.0 m

An analysis was conducted for two cases of soil from each trial pit (TP01, TP02 and TP03). In the first analysis, only the settlement induced by wetting (hydrocollapse) was considered. Conversely, the second scenario regarded the total settlement (that is, the sum of compression and hydroconsolidation volume change). For this case, additional parameters given in Table 6-6, derived from Figures 5-21 (b), 5-21 (d) and 5-21 (f), were also inputted.

Table 6-6, Summary of the settlement parameters

Parameters	TP01	TP02	TP03	Mean values	Deviation, %
Compression index, c_c	0.21	0.15	0.18	0.17	0.02
Swell index, c_s	0.010	0.010	0.014	0.01	0.00
Effective Pre-consolidation pressure, $\sigma p'$, kPa	13	16	16	15	1.73
Initial void ratio, e_o	0.429	0.444	0.387	0.43	0.04

6.4.3 Check for Settlement (SLS)

Figure 6-4 illustrates a top view of the model that was used in settlement analysis. It was assumed that pressure was uniformly distributed throughout the strip footing length. Thus, the evaluation was conducted per unit length. The region of masonry wall on the footing is shown by the dotted lines.

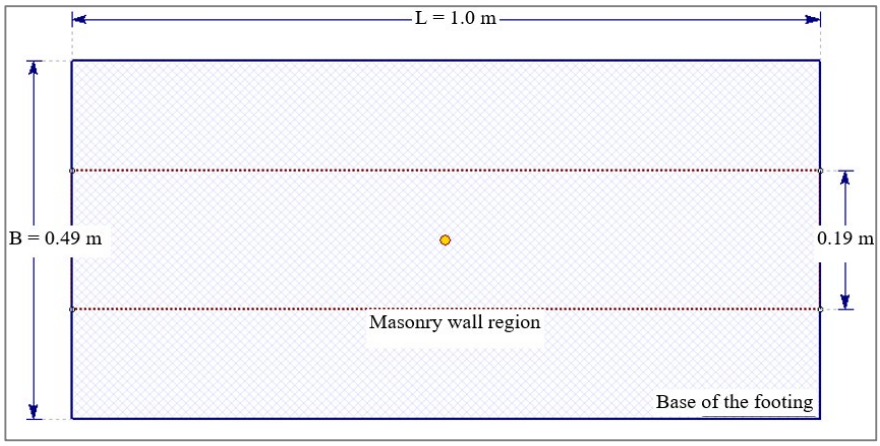

Figure 6-4, A model for settlement analysis

Case 1: Settlement due to hydrocollapse (TP01)

A 3-dimensional model of the strip footing loads acting on a 3 m thick stratum in soil from TP01 is demonstrated in Figure 6-5. The contours below the centre showed variation of the subsequent settlement with depth, while the lines along the soil indicated water table levels. The maximum hydroconsolidation (that is hydrocollapse) settlement occurred directly below the footing (128 mm) when the water table was raised to the ground surface. It was greater than the tolerable values of 20 or 50 mm, thus unsafe against the serviceability limit state. Due to reduced pressure increment ($\Delta\sigma$) at deeper depths, settlement was smaller than at shallow levels. This was shown by the linear increase of contour lengths from deep to shallow depths.

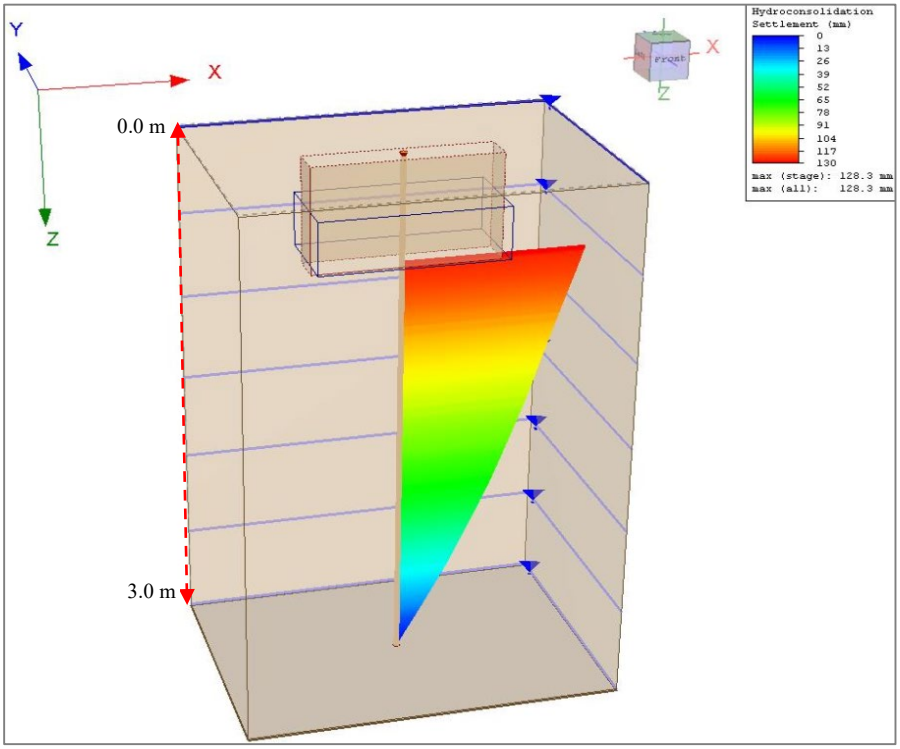

Figure 6-5, Hydrocollapse settlement of loaded soil from TP01

A hydroconsolidation analysis was made at each water level and the corresponding cumulative settlement was computed (Figure 6-6). Hydroconsolidation is a function of water; therefore, the settlement only occurred below the water table. The upper regions only moved relative to the lower saturated section. For this reason, settlement remained constant above the water table. This was indicated by the vertical graphs in Figure 6-6. Conversely, the cumulative hydroconsolidation settlement at various depths below the water table was shown by a slanting curve. A summation of all recorded cumulative displacement below the footing indicated the total hydroconsolidation settlement.

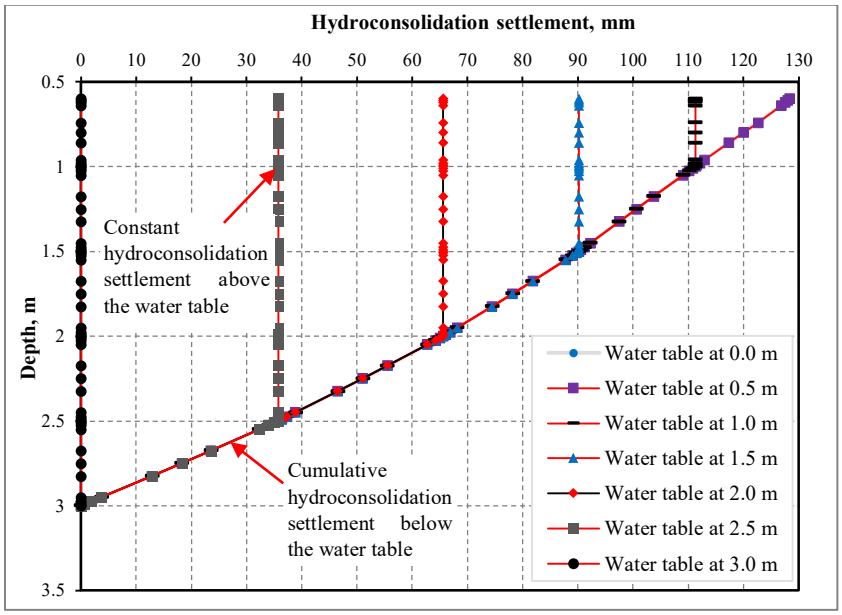

Figure 6-6, Variation of hydrocollapse settlement with increase in water table level, TP01

Case 1: Settlement due to hydrocollapse (TP02)

Raising the water table to the surface of a 2.1 m thick stratum in TP02 induced a maximum hydrocollapse settlement of 48 mm (Figure 6-7). The corresponding variation in settlement with water table levels is shown in Figure 6-8. The attained failure pattern was similar to that of TP01; however, the overall settlement was lower. This reduction was attributed to the thinner soil layer that was adopted in the settlement calculation (refer to Equation 6-6). In addition, the soil from TP01 demonstrated the highest compression index (0.21), while TP02 had the least value (0.15). This property influenced the susceptibility of the soil to decrease in volume under the applied strip loadings. The high value in TP01 resulted in substantial magnitude of settlement.

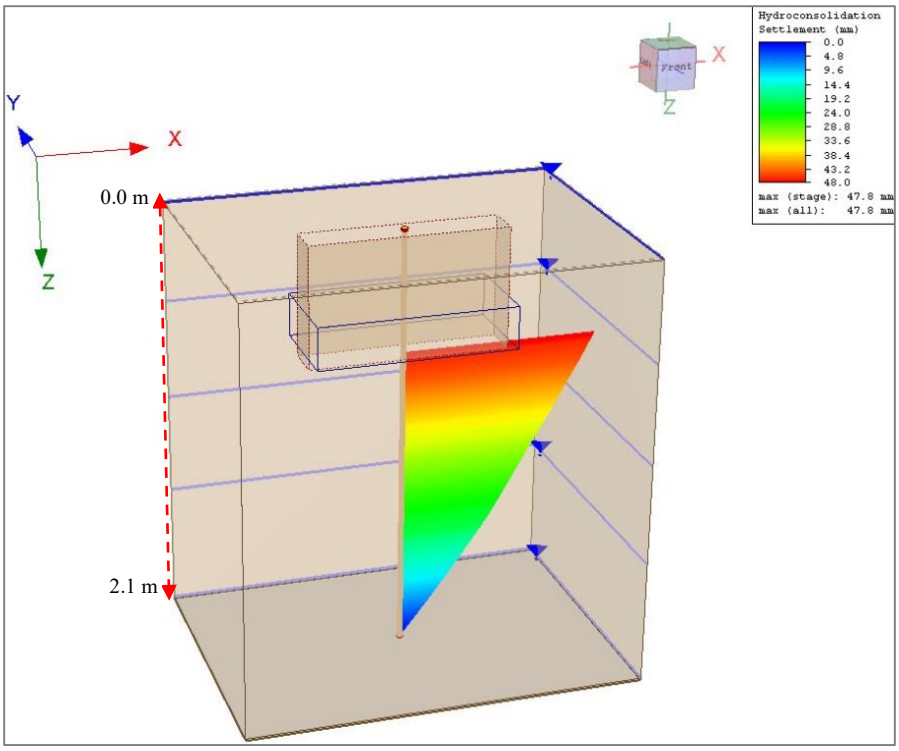

Figure 6-7, Hydrocollapse settlement of loaded soil from TP02

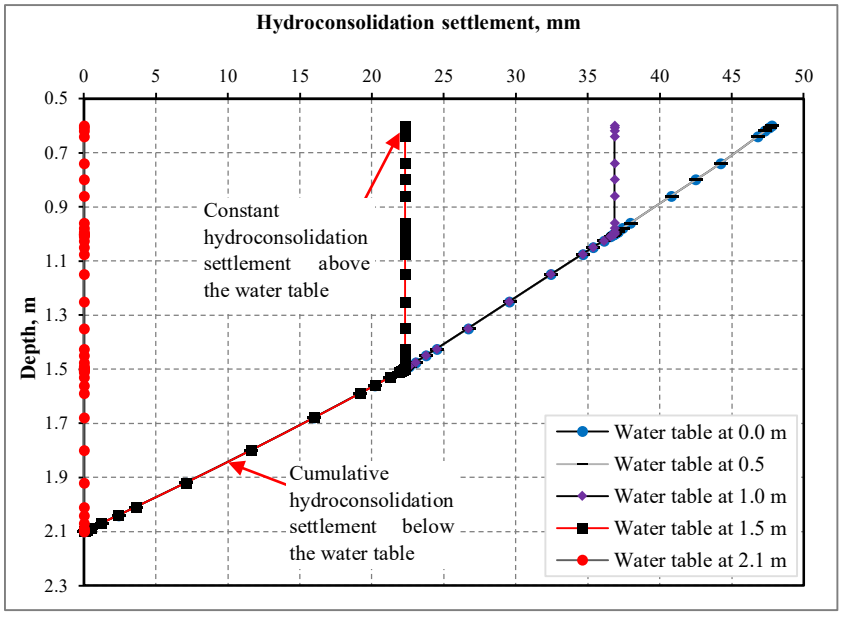

Figure 6-8, Variation of hydrocollapse settlement with increase in water table level, TP02

Case 1: Settlement due to hydrocollapse (TP03)

A hydroconsolidation settlement of 59 mm was demonstrated by the 3.0 m thick soil stratum in TP03 (Figure 6-9). This value was lower than the permissible limit, hence showed potential settlement problems on houses constructed within this locality. The graphical plot of settlement variation with levels of the water table is presented in Figure 6-10. The failure trend was similar

to those produced by samples from TP01 and TP02. The soil thickness was equal to that of TP01, but due to lower compression index (0.18), it exhibited the lower displacement.

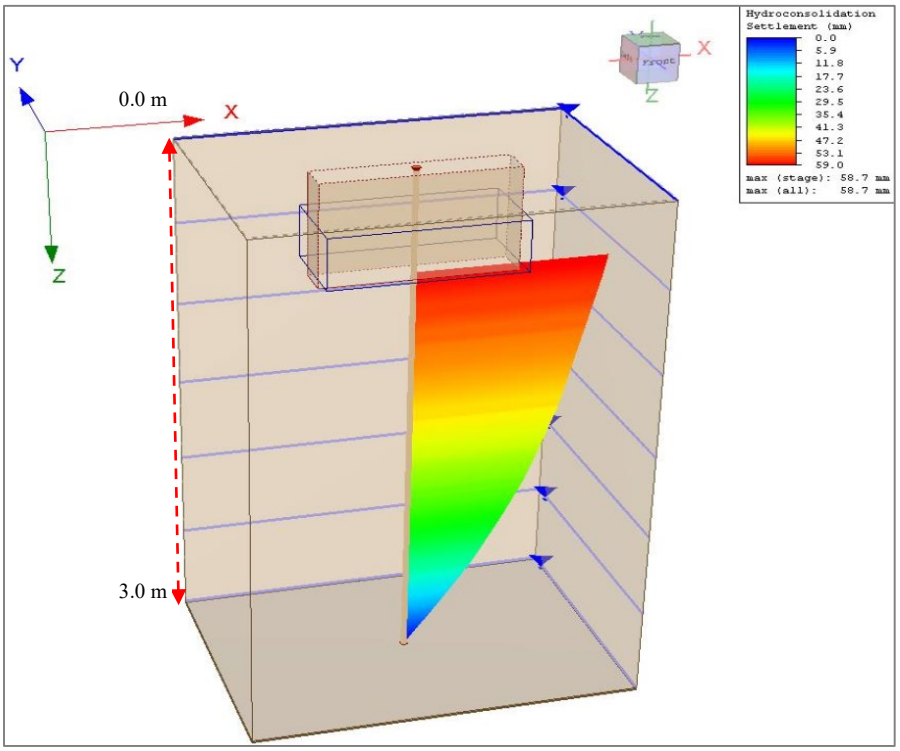

Figure 6-9, Hydrocollapse settlement of loaded soil from TP03

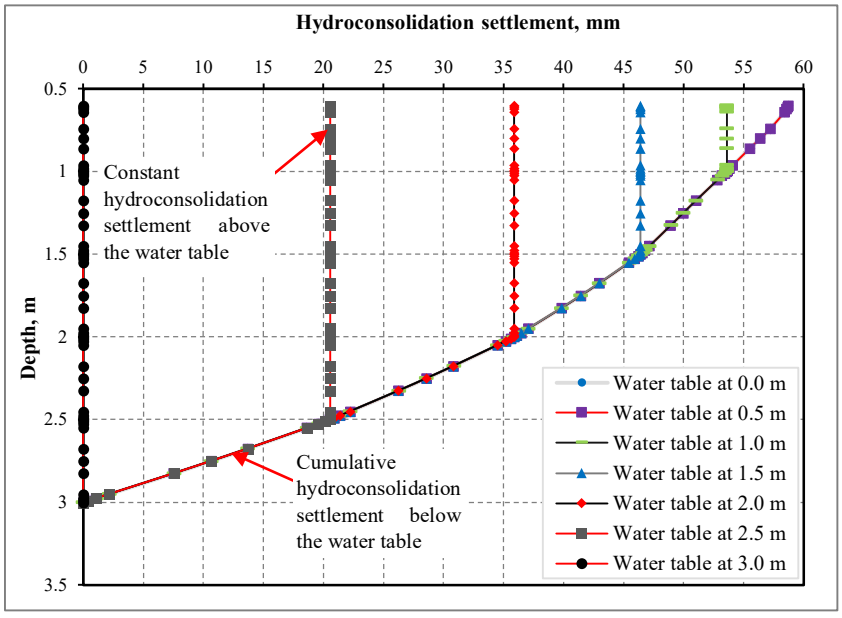

Figure 6-10, Variation of hydrocollapse settlement with increase in water table level, TP03

Case 2: Total settlement

The settlement was a total reduction in soil volume due to compression and hydroconsolidation (Table 6-7). The settlement at field moisture content was less than a limiting value of 50 mm,

hence less detrimental to the structures. Conversely, saturation drastically augmented the settlement to the magnitude that exceeded the allowable values. Based on serviceability limit state, the investigated soil has potential to induce the volume change problems such as cracks and could be related to the deformation observed in structures. Ground improvement techniques should, therefore, be deployed to reduce this settlement.

Table 6-7, Summary of total settlement

Pit number	TP01	TP02	TP03	Mean, m	Potential failure against the serviceability limit state
Settlement at field moisture condition, mm	29	17	25	24	Safe
Hydroconsolidation settlement, mm	128	48	59	78	Unsafe
Total settlement, mm	158	64	84	102	

7 Conclusions and Recommendations

7.1 Introduction

In this study the characteristic volume change properties of loess-like samples collected from Mount Moorosi, Lesotho were investigated using laboratory experiments such as Atterberg limits, wet sieving, sedimentation, free swell, x-ray diffraction, scanning electron microscope, slaking, triaxial and oedometer. The research revealed minimal swell potential and intolerable settlement due to the presence of kaolinite and structural arrangement of the soil, respectively. Consequently, the settlement was associated with the cracks observed on structures in Mount Moorosi. The summary of the research outcomes as well as recommendations for future studies on the tested soil are presented in this chapter.

7.2 Conclusions

The following conclusions were drawn from this effort:

- The soil from Mount Moorosi primarily consisted of silt-sized particles (49 to 87 %), followed by sand (4 to 32 %), while clay had the least composition by weight (5 to 16 %). Soil was classified as silt and sandy loess based on the particle size distribution. Profiling of this soil revealed that the loess-like stratum is averagely over 3 m in thickness. Based on index tests and the Unified Soil Classification System, the soil was categorised as clay of low plasticity (PI ranged from 9 to 17 %). In fact, the expansiveness potential was less than 2 %, which indicated least possibility to damage of superimposed structures by heaving. Furthermore, free swell index ranged from 0 to 12 %, which also validated low soil expansion under saturated conditions. The material, however, demonstrated a substantial vertical displacement/warping (up to 27 mm) in linear shrinkage on drying, which could induce detrimental stresses to structures.

- The soil mineralogy composed of quartz as the most dominant passive mineral (42 %), followed by feldspar (32 %), whereas mica was the third-most prevalent (12 %). The subordinate active minerals (14 %) chiefly consisted of kaolinite (8 %), whereas others were each less than 3 % by composition (halides, sulfates, carbonates, the oxides and hydroxides of aluminium and iron). The presence of minerals that become active in saturated conditions substantiated that the overall stability of the soil particles was possibly undermined at high moisture contents or under saturated conditions. Therefore, unfavourable to the founding soil.

- A morphological analysis revealed three distinct structures that could synergistically contribute to saturated volume decrease properties. These included porous clays, silts coated by clay and silts bonded with clay, which all rendered a metastable fabric to a soil.

- The deviator stress was relatively high at field moisture content and was reduced by up to 73 % under saturated tests. This was caused by augmentation of the interparticle spaces by pore water pressure that reached a maximum enhancement of 337 kPa. The subsequent shear strength parameters were also drastically reduced by up to 80 %. This indicated high resistance to the applied pressure at relatively low moisture content, but lower strength at higher moisture condition. These results implied that rise in moisture content of the loaded soil decreased the volume and contributed to the noted cracks.

- Inundation of the soil lumps in distilled water during slaking tests showed deflocculation into finer particles and smaller aggregates. This was an indication of high susceptibility to collapse and settlement under saturated conditions. Therefore, structures built on this type of soil are vulnerable to settlement induced damage.

- The soil demonstrated low decrease in void ratio at field moisture content as compared to that in saturated conditions. The subsequent hydrocollapse potential ranged from 10 to 15 % at an effective stress of 200 kPa and a collapse coefficient from 0.13 to 0.18 at stress of 300 kPa. These values showed the high possibility of damage to the superimposed structures caused by soil volume decrease. Furthermore, it was established that an increase in magnitude of applied effective stresses reduced the void ratio. Greatest changes were observed at stresses ranging from >12 to 400 kPa. The pressures from the typical houses in the region of study were within these detrimental range (22 kPa). This substantiated that the induced settlement was associated with the observed structural deformation.

7.3 Recommendations

- This study established the volume change properties of the loess like deposits in Mount Moorosi. However, more research work must be done to understand the magnitude of the pressures exerted during soil shrinkage.

- Since the soil volume decrease is unfavourable to structures constructed on this soil, the most suitable ground improvement techniques that could be deployed to overcome this problem should be explored.

- The distribution and provenance of loess-like soil in Lesotho should be studied to understand the extend of the volume change problem.

References

Adaira, J. H., Suvacib, E. & Sindela, J. 2001. Surface and Colloid Chemistry. Encyclopedia of Materials: Science and Technology, Second Edition:1 - 10.

Al-Harthi A. A. & Bankher, K. A. 1999. Collapsing loess-like soil in Western Saudi Arabia. *Journal of Arid Environments,* Vol. 41: 383 - 399.

Altmeyer, W. T. 1955. Discussion of Engineering properties of expansive clays. Proceedings of the American Society of Civil Engineers, Vol. 81 (658).

American Standard Test Methods (ASTM D4767-11), Standard test method for consolidated undrained triaxial compression test for cohesive soils

American Standard Test Methods (ASTM D5333 – 03 – 1996), Standard Test Method for Measurement of Collapse Potential of Soils.

American Standard Test Methods (ASTM E177-14), Standard Practice for Use of the Terms Precision and Bias in ASTM Test Methods

Anagnosti, P. 1973. Storage Dams Founded on Collapsing Loess Soils. Proceedings of the 8th International Conference on Soil Mechanics and Foundation Engineering, Vol. 2: 7-11, Moscow.

Arvind, R. 2017. Investigation of Cracks in Buildings. *ResearchGate.*

Assallay, A.M., Rogers, C.D.F. & Smalley, I.J. 1996. Engineering properties of loess in Libya: *Journal of Arid Environments,* Vol. 32: 373–386. Specific gravity graph

Assallay, A. m. 2001. Structure and Hydrocollapse Behaviour of Loess. Doctoral Thesis: Loughborough University Institutional Repository.

Barden, L., McGown, A. & Collins, K. 1973. The Collapse Mechanism in Partly Saturated Soil. *Engineering Geology,* Vol. 7: 49 - 60.

Barta, G. 2011. Secondary Carbonates in Loess-Paleosoil Sequences: A General Review. *Central European Journal of Geosciences,* Vol: 3(2): 129 - 146.

Basma, A. A. & Tunc, E. R. 1992. Evaluation and Control of Collapsible Soils. *Journal of the Geotechnical Engineering Division, ASCE,* Vol. 118 (10), 1491 - 1504.

Bell, F. G. & Haskins, D. R. 1997. A Geotechnical Overview of Katse Dam and Transfer Tunnel, Lesotho, with a Note on Basalt Durability. *Engineering Geology,* Vol. 46:175 - 198.

Bell, F. G. & Maud, R. R. 2015. Dispersive Soils: A Review from a South African Perspective. *Quarterly Journal of Engineering Geology,* Vol. 27: 195 – 210.

Bíl, M. & Kubeèek, J. 2012. Piping in Loess-Like and Loess-Derived Soils: Case Study of Halenkovice Site, Czech Republic. *Annales Societatis Geologorum Poloniae,* Vol. 82 (1): 45 - 50.

Black, D.K & Lee, K. 1973. Saturating Laboratory Samples by Back Pressure. *Journal of soil mechanics and foundations,* Vol. 99, 75-93.

Blight, G. E. & Leong, E. C. 2012. Origin and formation of residual soils. Mechanics of Residual Soils, 2nd edition. Leiden: CRC Press Taylor & Francis Group.

Bond, A. & Harris, A. 2008. Decoding Eurocode 7. London and New York: Taylor and Francis.

Bray, J. 2000. As reported by Hayden, C. P. 2014. Liquefaction-Induced Building Performance and Near-Fault Ground Motions. PhD Thesis: University of California, Berkeley.

Brink, A. B. A. 1983. Engineering Geology of Southern Africa: The Karoo Sequence, Volume 3. Cape Town: Building Publications.

Brink, A. B. A. 1985. Engineering Geology of Southern Africa: Post-Gonndana Deposits, Volume 4. Cape Town: Building Publications.

British Standard (BS 1377-2-1990). Methods of test for Soils for civil engineering purposes, Part 2: Classification tests.

British Standard (BS 1377-4-1990). Methods of test for Soils for civil engineering purposes, Part 4: Compaction-related tests.

British Standard (BS 1377-5-1990). Methods of test for soils for civil engineering purposes. Compressibility, permeability and durability tests, Part 5: Compaction-related tests.

British Society for Geomorphology, 2018. Educational Resources – Glacial Environments: Ice Movements and Glacier Flow. https://www.geomorphology.org.uk

Building Code Interpretation 2008 (06-BCI-014). STANDATA: The Alberta Building Code 2006 for footing design.

Burland, J. B. 1977. Behaviour of Foundations and Structures. *ResearchGate.*

Buttrick, D.B., Schalkwyk, A. V., Kleywegt, R., & Watermeyer, R.B. 2001. Proposed method for dolomite land and hazard and risk assessment in South Africa. *Journal of South Africa Institution of Civil Engineers,* Vol. 43: 27-36.

Byrne, A. D. & Berry, G. 2008. A Guide to Practical Geotechnical Engineering in Southern Africa. Fourth Edition: Franki

Catuneanua, O. & Elangob, H. N. 2001. Tectonic control on Fluvial styles: the Balfour Formation of the Karoo Basin, South Africa. *Sedimentary Geology,* Vol. 140: 291 - 313.

Carroll, D.M. & Bascomb, C.L. 1967. Notes on the Soils of Lesotho. Technical Bulletin No.1: Land Resources Division. Directorate of Overseas Surveys. Tolworth, Surrey, England.

Coelho, A. (2007) TOPAS-Academic, Coelho Software, Brisbane, Australia.

Craig, R. F. 2004. Craig's Soil Mechanics: seventh edition. New York and Canada: Taylor and Francis Group.

Craig, R. F. & Knappett, J. A. 2012. Craig's Soil Mechanics: eighth edition. New York and Canada: Taylor and Francis Group.

Crouvi, O., Amit, R. Enzel, Y. & Gillespie, A. R. 2010. Active Sand Seas and the Formation of Desert Loess. *Quaternary Science Reviews,* Vol. 29: 2087 - 2098.

Darwell, J. L. & Denness, B. 1976. Prediction of Metastable Soil Collapse. International Association of Hydrological Sciences: Proceedings of the Anaheim Symposium.

Das, B. M. 2013. Advanced Soil Mechanics, Fourth Edition. CRC Press

Delage, P., Cui1, Y. J. & Antoine, P. 2005. Geotechnical problems related with loess deposits in Northern France. Proceedings of International Conference on Problematic Soils, Eastern Mediterranean University, Famagusta, N. Cyprus.

Derbyshire, E., Dijkstm, T. A., Smalley, I. J. & Li, Y. 1994. Failure Mechanisms in Loess and the Effects of Moisture Content Changes on Remoulded Strength. *Quaternary International,* Vol. 24: 5-15.

Djogo, M. & Milović, D. 2013. Differential settlement of foundations on loess. Seventh international conference on case histories in geotechnical engineering. *Missouri University of Science and Technology.*

Dollman, K. N., Viglietti, P. A. & Choiniere, J. N. 2017. A New Specimen of Orthosuchus Stormbergi (Nash 1968) and a Review of the Distribution of Southern African Lower Jurassic Crocodylomorphs. *ResearchGate.*

Edgar, H. N. 1991. Dispersive Clays: Soil Mechanics Note No. 13. U.S. Department of Agriculture Soil conservation Service Engineering Division.

Egri, G. 1972. The Physico-Chemical Properties and Engineering Problems of the Loess Soils. *Acta Gelo. Acad, Sci. Hung,* Vol. 16: 337 - 345.

Elges, H.F.W.K. 1985. Dispersive Soils. *Transactions of the South African Institution of Civil Engineers, Special Issue: Problem soils in South Africa*, Vol. 27: 347-353.

Eurocode 7 (DD ENV 1997-1:1995), Geotechnical design - Part 1: General rules.

Finn, W.D.L. & Fujita, N. 2002. Piles in Liquefiable Soils: Seismic Analysis and Design Issues. *Soil Dynamics and Earthquake Engineering,* Vol. *22: 731-742.*

Fredlund, D. G. 1975. Engineering Properties of Expansive Clay. Presented to a seminar on shallow foundations on expansive soils in Regina, Saskatchewan.

Gao, G. 1996. The Distribution and Geotechnical Properties of Loess Soils, Lateritic Soils and Clayey Soils in China. *Engineering Geology*, Vol. 42: 95 - 104.

Geotechnical tools, 2019. Settlement and Consolidation Analysis: https://www.rocscience.com

Gerber, F. A., & Harmse, H. J. V. M. 1987. Proposed Procedure for Identification of Dispersive Soils by Chemical Testing. *Civil Engineer in South Africa,* Vol. 29: 397-399.

Gibbs, H. J. & Holland, W. Y. 1960. Petrographic and Engineering Properties of Loess. United States Department of the Interior Bureau of Reclamation: Engineering Monographs No. 28.

Glassey, P. J. 1986. Geotechnical Properties of Lime Stabilised Loess, Port Hills, Canterbury. Master's dissertation: University of Canterbury

Grab, S. Linde, J. & Lemos, H. D. 2017. Some Attributes of Snow Occurrence and Snowmelt/Sublimation Rates in the Lesotho Highlands: Environmental Implications. *African Journals Online,* Vol. 43.

Grigoryan. A.A. 1991. Construction on loess soil.

Grim, R. E. 1953. Clay Mineralogy. New York: McGraw-Hill.

Guideline for Human Settlement Planning and Design, South Africa, 2005. Pretoria: CSIR Building and Construction Technology. Vol 2.

Guidelines for Soil and Rock Logging in South Africa, 2002. Proceedings, Geoterminology Workshop organised by AEG, SAICE and SAIEG, 1990.

Holtz, W. G. & Gibbs, H. J. 1956. Engineering properties of expansive clays. *American Society of Civil Engineers*, Vol. 121 (1): 641 - 663.

Home Building Manual, South Africa 2014.

Howayek, A.E.I., Huang, P., Bisnett, R. & Santagata, M.C. 2011. Identification and Behavior of Collapsible Soils, *Joint transportation research program*, FHWA/IN/JTRP-2011/12.

Huat, B. B. K. 1998. An Investigation of an Embankment Failure in Soft Clay. *Proceedings: Fourth International Conference on Case Histories in Geotechnical Engineering, St. Louis, Missouri.*

Jennings, Brink, A. B. A. & Williams, A. A. B. 1973. Revised Guide to Soil Profiling for Civil Engineering Purposes in Southern Africa. *South African Institution of Civil Engineers,* Vol. 15: 3 - 12.

Jennings, J. E., Brink, A. B. A., Louw, A., & Gowan, G. D. 1965. Sinkholes and Subsidences in the Transvaal Dolomite of South Africa.

Jeong, G. Y., Hillier, S. & Kemp, R. B. 2011. Changes in Mineralogy of Loess–Paleosol Sections Across the Chinese Loess Plateau. *Quaternary Research,* Vol. 75: 245 - 255.

Johnson, M. R., Vuuren, C. J. V., Hegenberger, W. F., Key, R. & Shoko, U. 1996. Stratigraphy of the Karoo Supergroup in southern Africa: an overview. *Journal of African Earth Sciences,* Vol. 23 (1): 3 - 15.

Jones, G. A. & Davies, P. 1985. Soft clays: Problem Soils in South Africa: State of the Art. Civil Engineer in South Africa, Vol. 27 (7): 355 - 357.

Jowett, T. W. D. 1995. An Investigation of the Geotechnical Properties of Loess from Canterbury and Marlborough. Master's dissertation: University of Canterbury.

Kalpakci, V. 2017. Collapse of Base Soil and its Consequences During a Cement Plant Construction. *Selcuk University Journal of Engineering, Science and Technology,* Vol. 5: 500 -510.

Kalumba, D. 2019. Foundation Design Notes: University of Cape Town.

Karathanasis, A. D. 2009. Soil Mineralogy. Land Use, Land Cover and Soil Sciences, 6.

Kie, T. T. 1985. Fundamental Properties of Loess from Northwestern China. *Engineering Geology,* Vol. 25: 103 - 122.

Kitcher J.S.D. 1980. Brief Note on Estimates of the Cost of Structural Repair to Houses Built on Active Clays in South Africa Between 1980 and 2000. Proceedings of the South African Geotechnical Conference, Silverton, 11-13.

Klukanova, A. & Frankovska, J.1995. The Slovak Carpathians Loess Sediments, their Fabric and Properties. Genesis and properties of collapsible soils. London and New York: Plenum Publishing Corporation.

Kodikara, J., Barbour, S. L. & Fredlund, D. G. 2002. Structure Development in Surficial Heavy Clay Soils: A Synthesis of Mechanisms. *Australian Geomechanics,* Vol. 37 (3): 25 - 40.

Konrad, R., Roscher, B., Knabe, K., & Smykatz-Kloss, W. 2004. Alluvial Loess in the Central Sinai: Occurrence, Origin, and Palaeoclimatological Consideration. *ResearchGate.*

Knodel, P. C. 1992. Characteristics and Problems Soils. U.S. Department of the Interior Bureau of Reclamation Denver Office Research and Laboratory Services Division Materials Engineering Branch.

Krinitzsky, E. L. & Turnbull, W. J. 1967. Loess Deposits in Mississippi. Geological Society of America, Special Paper Series, Vol. 94,64 p. New York: The Geological Society of America, INC.

Lambe, T. W. 1953. The Structure of Inorganic Soil. Proceedings of the American Society of Civil Engineers, Vol. 79 (10): 1 - 49. Reported by Punmia B. C., Jain, A. K. & Jain, A. K. 2005. Soil Mechanics and Foundations, Sixteenth Edition. Delhi: Laxmi Publications (P) Ltd.

Langfelder, L. J. & Nivargikar, V. R. 1967. Some Factors Influencing Shear Strength and Compressibility of Compacted Soils. Symposium on Compaction of Earthwork and Granular Bases.

Letsie, M. M. & Grab, S. W. 2015. Assessment of Social Vulnerability to Natural Hazards in the Mountain Kingdom of Lesotho. *Mountain Research and Development,* Vol. 35 (2):115 - 125.

Li, R., 2, Liu, J. YAN, R., Zheng, W. & Shao, S. 2014. Characteristics of Structural Loess Strength and Preliminary Framework for Joint Strength Formula. *Water Science and Engineering,* Vol. 7 (3): 319 - 330.

Li, Y., He, S., Deng, & Xuc, Y. 2018. Characterization of Macropore Structure of Malan loess in NW China Based on 3D Pipe Models Constructed by Using Computed Tomography Technology. *Journal of Asian Earth Sciences,* Vol 154: 271 - 279.

Liu, Z., Liu, F., Ma, F., Wang, M., Bai, X., Zheng, Y., Yin, H. & Guoping Zhang, G. 2015. Collapsibility, Composition, and Microstructure of a Loess in China. *Canadian Geotechnical Journal,* Vol. 53 (4): 673 - 686.

Lobdel, G.T. 1981. Hydroconsolidation potential of Palouse loess. *Journal of the Geotechnical Engineering Division: American Society of Civil Engineers,* Vol. 107: 733-742.

Lopes, R. P., Dillenburg, S. R, & Schultz, C. L. 2016. Cordão Formation: Loess Deposits in the Southern Coastal Plain of the State of Rio Grande Do Sul, Brazil. *Anais da Academia Brasileira de Ciências,* Vol. 88: 2143 - 2166.

Lucian, C. 2006. Geotechnical Aspects of Buildings on Expansive Soils in Kibaha, Tanzania: Preliminary Study. Licentiate Thesis: Royal Institute of Technology Stockholm, Sweden.

Lutenegger, A.J. & Hallberg, G.R. 1988. Stability of Loess. *Engineering Geology,* Vol. 25: 247 – 261.

Marcelino, V., Stoops, G., Schaefer & C. E.G.R. 2010. 14 - Oxic and Related Materials. Interpretation of Micromorphological Features of Soils and Regoliths, 305 - 327.

McCarthy, T. & Rubidge, B. 2005. The Story of the Earth & Life: A Southern African Perspective on a 4.6 Billion Year Journey. Cape Town: Struik Nature.

McGarry, D. 2004. A Methodology of a Visual Soil – Field Assessment Tool - to Support, enhance and Contribute to the LADA Programe.

McMullen, M. 2000. SOILpak for Vegetable Growers: New South Wales Agriculture.

Mineral Map of the Republic of South Africa (RSA), 2018. Council for Geoscience: https://www.geoscience.org.za

Moriwaki, Yoshiharu & Mitchell, J. K. 1977. The Role of Dispersion in the Slaking of Intact Clay: *Dispersive Clays, Related Piping, and Erosion in Geotechnical Projects, ASTM STP 623,* J. L. Sherard and R. S. Decker, Eds., American Society for Testing and Materials, 287 - 302.

Muggler, C. C., Buurman, P. & Doesburg, J. D. J. V. 2007. Weathering Trends and Parent Material Characteristics of Polygenetic Oxisols from Minas Gerais, Brazil: I. Mineralogy. *Geoderma,* Vol. 138: 39 - 48.

Ng, C. W. W., Mu, Q. Y. & Zhou, C. 2017. Effects of Soil Structure on the Shear Behaviour of an Unsaturated Loess at Different Suctions and Temperatures. *Canadian Geotechnical Journal,* Vol. 54 (2): 270 - 279.

Nouaouria, M. S., Guenfoud, M. & Lafifi, B. 2008. Engineering Properties of Loess in Algeria. *Engineering Geology,* Vol. 99: 85 - 90.

Olivier, H. J. 1979a. Some Aspects of the Influence of Mineralogy and Moisture Redistribution on the Weathering Behaviour of mudrocks. Proceedings of the fourth International Society for Rock Mechanics. Vol. I, 467 - 474.

Oosthuizen A. C. & Richardson, S. 2011. Sinkholes and Subsidence in South Africa. *Council for Geoscience.*

Osipov, V. I., & Sokolov, V. N. 1994. Factors and mechanism of loess collapsibility. *Proceesings of the NATO Advanced Research Workshop on Genesis and Properties of Collapsible Soils, Loughborough, U.K.*

Page, A. W. 2001. The Serviceability Design of Low-rise Masonry Structures. *Progress in structural engineering and materials,* 257 - 267.

Pecsi, M. 1990. Loess is Not Just the Accumulation of Dust. *Quaternary International,* Vol. 7/8: 1 - 21.

Punmia B. C., Jain, A. K. & Jain, A. K. 2005. Soil Mechanics and Foundations, Sixteenth Edition. Delhi: Laxmi Publications (P) Ltd.

Puppala, A.J., Wejrungsikul, T., Puljan, V. & Manosuthikij, T. 2012. Measurements of Shrinkage Induced Pressure (SIP) in Unsaturated Expansive Clays. *Geotechnical Engineering Journal of the SEAGS & AGSSEA,* Vol. 43 (1).

Pye, K. 1984. Loess. *Progress in physical geography: earth and environment,* Vol. 8: 176 – 217.

Pye, K. 1987. Aeolian dust and dust deposits. London: Academic press.

Raeside, J. D. 1964. Loess Deposits of the South Island, New Zealand, and Soils Formed on them. *New Zealand Journal of Geology and Geophysics,* Vol. 7.

Rahardjo, P. P. 2014. Geotechnical Failures Case Histories of Construction on Soft Soils, Forensic Investigations and Counter Measures in Indonesia. *International Journal of Integrated Engineering,* Vol. 6: 11-23.

Raza, M. 2017. Oxygen Vacancy Stabilized Zirconia; Synthesis and Properties. Ph.D. Thesis: Chimie des Interactions Plasma-Surface (ChIPS), Faculty of Sciences University of Mons BE-7000 Mons, Belgium.

Rogers, C.D.F., Dijkstra, T.A. & Smalley I.J. 1994. Hydroconsolidation and subsidence of loess: Studies from China, Russia, North America and Europe. Engineering Geology, Vol. 37: 83-113.

Rogers, J. D., Olshansky, R. & Rogers, R. B. 2015. Damage to Foundations from Expansive Soils. *ResearchGate.*

Rogers, C. D. F. 1995. Types and Distribution of Collapsible Soils. Proceedings of the NATO Advanced Research Workshop on Genesis and Properties of Collapsible Soils.

Rooy, J. L. V. & Schalkwyk, A. V. 1993. The geology of the Lesotho Highlands Water Project with Special Reference to the Durability of Construction Materials. *Journal of African Earth Sciences,* Vol. 16: 181-192.

Rowell, D. L. 2014. Soil Science: Methods & Applications 1st Edition, Kindle Edition. New York: Routedge.

Rust, E., Heymann, G. & Jones, G. 2010. Collapsible Soils an Overview. Sabinet: African Journals.

Santrač, P., Bajić, Z., Grković, S., Kukaras, D. & Hegediš, I. 2015. Analysis of Calculated and Observed Settlements of the Silo on Loes, *Tehnički vjesnik,* Vol. 22: 539-545.

Schwartz, K. 1985. Collapsible Soils: Problem Soils in South Africa: State of the Art. The Civil Engineer in South Africa, Vol. 27: 379 - 393.

Seed, R. B., Cetin, K. O., Moss, R. E. S., Kammerer, A. M., Wu, J., Pestana, J. M., & Riemer, M. F. 2001. Recent Advances in Soil Liquefaction Engineering and Seismic Site Response Evaluation. Fourth International Conference on Recent Advances in Geotechnical Earthquake Engineering and Soil Dynamics, *Scholars' Mine.*

Sene, K.J., Jones, D.A., Meigh, J.R. & Farquharso, F.A.K. 1997. Rainfall and Flow Variations in the Lesotho Highlands. *International Journal of Climatology,* Vol. 18: 329 - 345.

Shafiei, A. & Dusseault, M. B. 2015. Engineering Properties of Loess from NE Iran. *ResearchGate.*

Shafique, M. A. & Qayyum, T. I. 2016. Comparison of Bearing Capacity Equations for Vertical Central Loading. *ResearchGate.*

Sheeler, J. B. 1968. Summarization and Comparison of Engineering Properties of Loess in the United States.

Sinclair, H. D. & Allen, P. A. 1992. Vertical Versus Horizontal Motions in the Alpine Orogenic Wedge: Stratigraphic Response in the Foreland Basin. *Basin Research,* Vol. 4: 215 - 232.

Smalley, I. 1990. Possible Formation Mechanisms for the Modal Coarse-Silt Quartz Particles in Loess Deposits. *Quaternary international,* Vol. 7/8: 23 - 27.

Smith, B. J., Wright, J. S. & Whalley, W. B. 2001. Sources of Non-Glacial, Loess-Size Quartz Silt and the Origins of ‘‘Desert Loess’’. *Earth-Science Reviews*, Vol. 59: 1 - 26.

Sobhee-Beetul, L. & Kalumba, D. 2015. Stone Column Reinforcement of a Soft South African Clay: A Laboratory Investigation. *Geotechnical Engineering Journal of the SEAGS & AGSSEA*, Vol. 46 (4).

Sun, J. 2002. Provenance of Loess Material and Formation of Loess Deposits on the Chinese Loess Plateau. *Earth and Planetary Science Letters*, Vol. 203: 845 - 859.

Terzaghi, K. 1943. Theoretical Soil Mechanics. New York: John Wiley and Sons, INC.

Thomaz, E., Sousa, H., Roman, H., Morton, J., Silva, J. M., Corrêa, M., Pfeffermann, O., Lourenço, P. B., Vicente, R. S., Sousa, R. 2014. Defects in Masonry Walls Guidance on Cracking: Identification, Prevention and Repair, *International Council for Research and Innovation in Building and Construction.*

Vandanapu, R., Omer, J. R., & Attom, M. F. 2016. Geotechnical Case Studies: Emphasis on Collapsible Soil Cases. Proceedings of the Institution of Civil Engineers: *Forensic Engineering,* Vol. 169.

Wagener, F. V. M. 1985. Dolomites. Problems of soils in South Africa - State of the art. *The Civil Engineer in South Africa,* Vol. 27: 395-407.

Watermeyer, R. B., & Tromp, B. E. 1992. A Systematic Approach to the Design and Construction of Single-Storey Residential Masonry Structures on Problem Soils.

Weinert, H. H. 1980. The Natural Road Construction Materials of Southern Africa. Pretoria: H & R Academia Publishers.

Whitlow, R. 1995. Basic of soil mechanics: third edition. London: Longman group limited.

Yang, Y. 1989. Study of the Mechanism of Loess Collapse. *Science in China*, Vol. 32: 604 - 617.

Yuan-xun, L., Yan-peng, Z., Shuai-hua, Y. & Zhong-mao, H. 2013. Analysis of foundation non-uniform settlement for building on collapsible loess. *Applied Mechanics and Materials*, 353-356.

Zeuner, F. E. 1950. Frost Soils on Mount Kenya, and the Relation of Frost Soils to Aeolian Deposits. *European Journal of Soil Mechanics.*

Zhu, Y., Jia, X. & Shao, M. 2018. Loess Thickness Variations Across the Loess Plateau of China. *Surveys in Geophysics,* Vol. 39: 715 - 727.

List of Appendices

Appendix A: Ground profiles from the borehole Logs

The geotechnical exploration borehole logs were prepared by Enviro-geotech company which provides drilling services. This was undertaken during the construction of a bridge between Phamong and Mount Moorosi across the Senqu river in 2014. These boreholes were located approximately 3 km from the Mount Moorosi residential site. The subsequent ground profiles were herein developed (Figure 1). They were utilised to confirm the geomorphology presented from both the literature and geological maps regarding the Stormberg lithology.

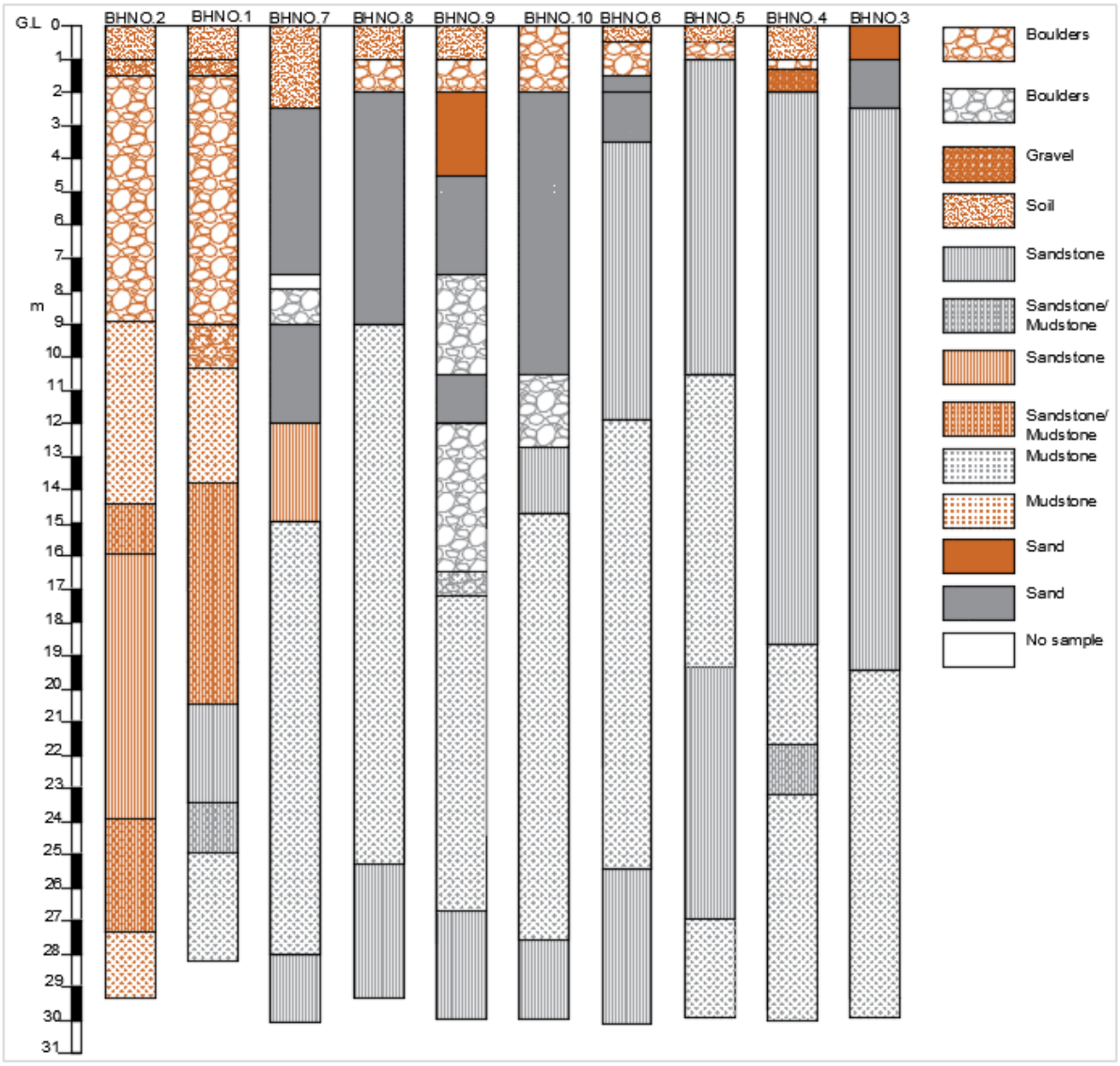

Figure 1, Soil profile at the Senqu river bridge in Mount Moorosi (Generated from Enviro-geotech report, 2014)

The soil profile indicated the prevalence of sand, boulders, minor gravel deposits and major occurrence of sandstone along with mudstone intrusions. It showed that the soil was shallow and only extended to a depth of less than 0.5 m. This could be associated with a continual soil erosion and deposition by the river. The sand and boulders were underlain by either greyish sandstones

or red and grey mudstones. It was also reported in the logs that some of the encountered boulders were from either sandstone or dolerite origin. The recorded rocks were in agreement with the documented geology within the Stormberg landform (Brink, 1983; Rooy & Schalkwyk, 1993). It should, however, be pointed out that this ground profile could only be used as a guide and not the exact representation of the soil distribution in the Mount Moorosi residential settlement due to the difference in altitude. The boreholes were located at an elevation of 1455 m amsl which is lower than that of the residential area. Besides, a rapid physical weathering took place in the river due to frequent water currents and abrasions of rocks.

Appendix B: Trial pits

Figure 2 is a map which shows the study area and the locations of the three trial pits that were excavated in Mount Moorosi village. These pits are depicted from Figure 1 to 5.

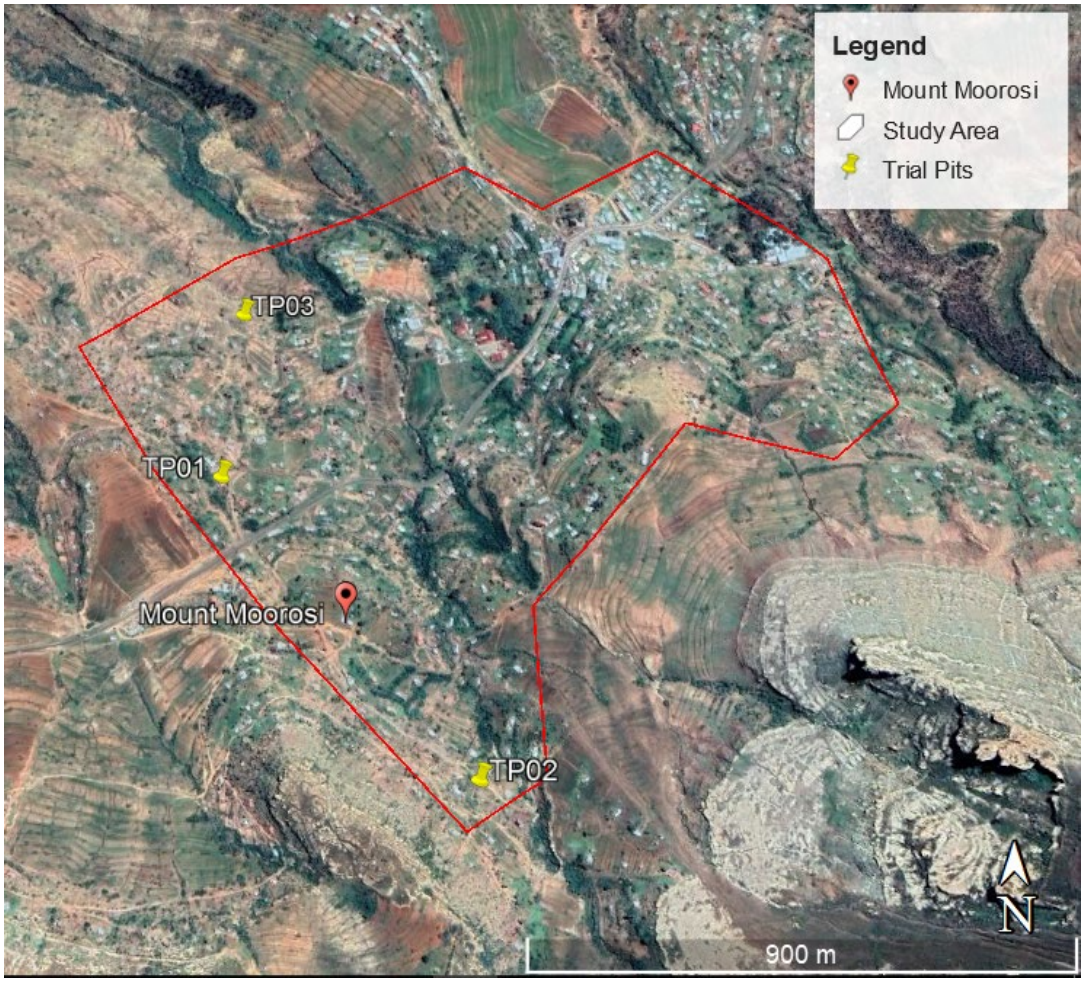

Figure 2, Locations for the trial pits in Mount Moorosi (Source: Google earth, 2019)

Figure 3, Trial pit 1 (TP01) in Mount Moorosi

Figure 4, A pinholed soil aggregate, TP01

Figure 5, Trial pit 2 (TP03) in Mount Moorosi

Figure 6, The green to grey boulders extracted from the bedrock at the base of the pit, TP01

Figure 7, Trial pit 3 (TP03) in Mount Moorosi

Figure 8, A soil aggregate, TP03

Appendix C: Micrographs

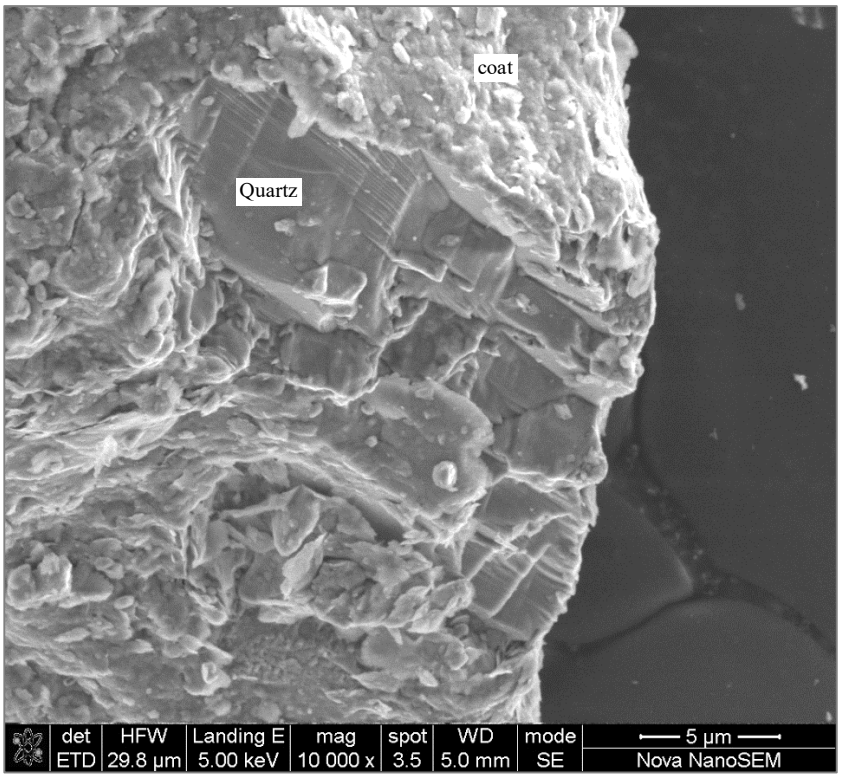

Figure 9, SEM-Micrograph of cemented quartz, TP01

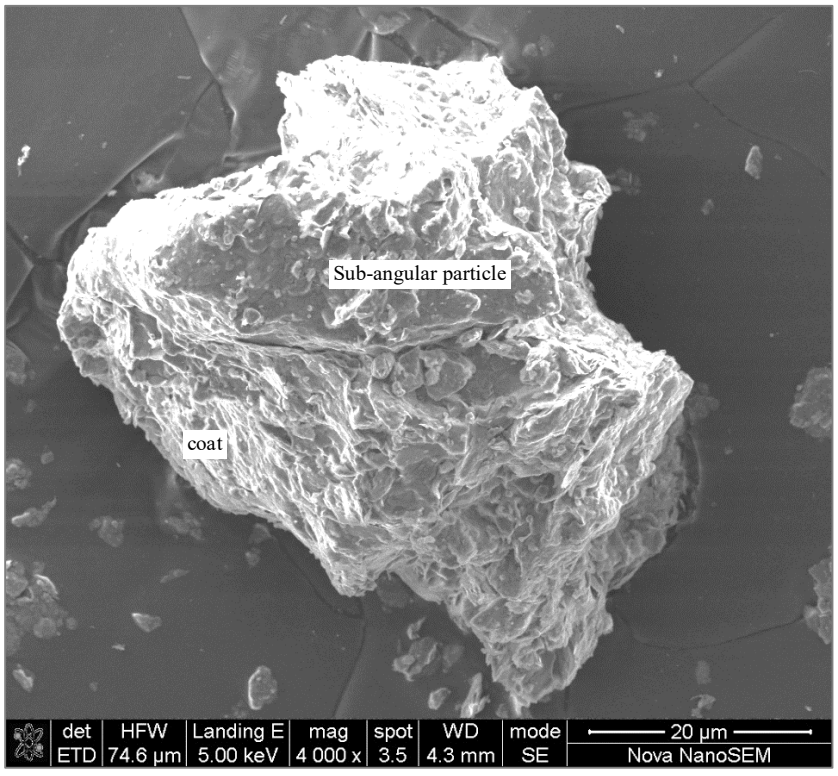

Figure 10, SEM-Micrograph of cemented sub-angular particles, TP02

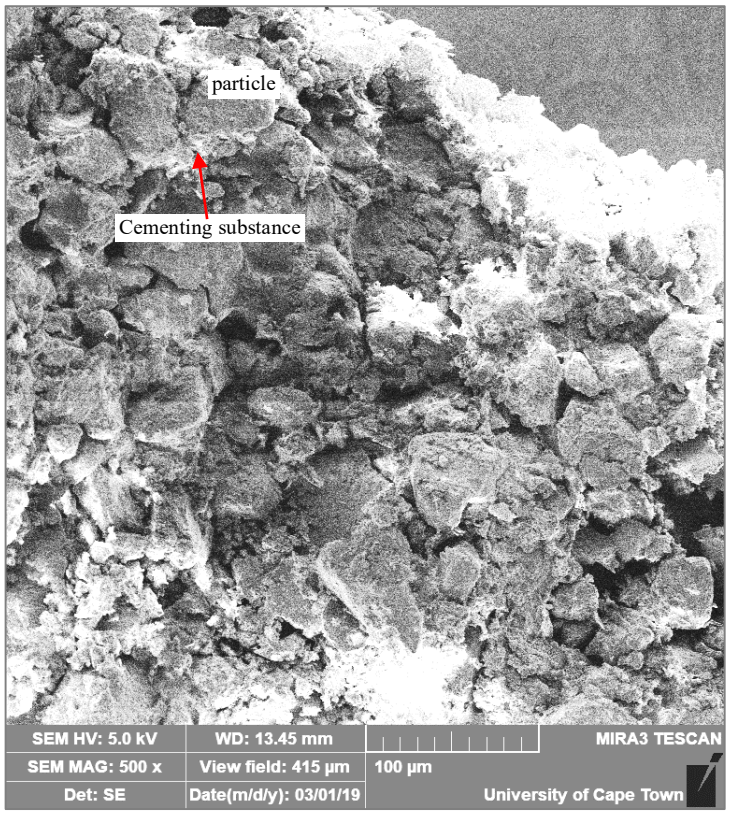

Figure 11, SEM-Micrograph of bonded sand and silt particles, TP03

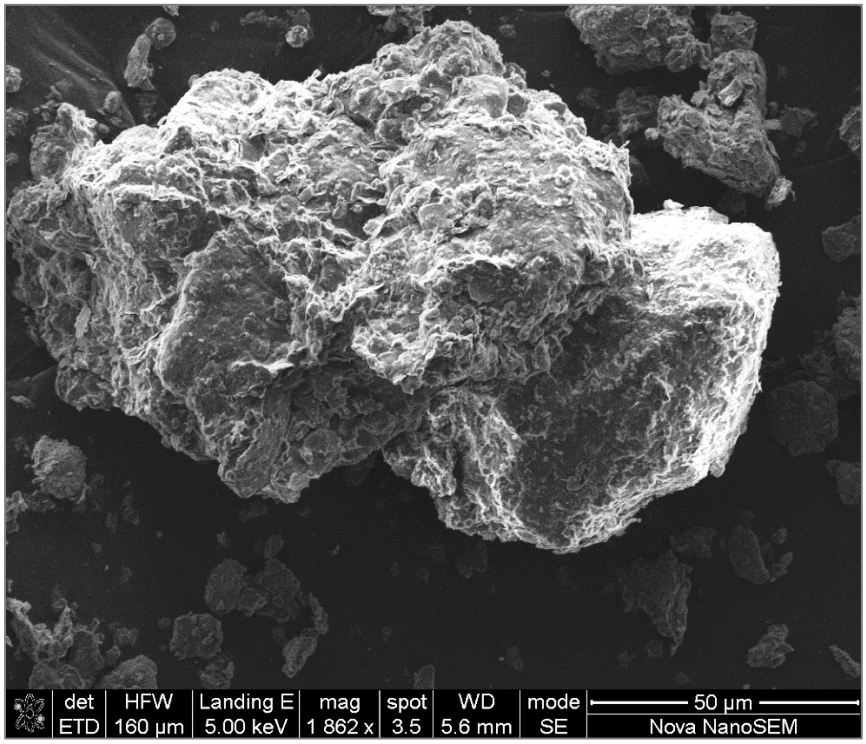

Figure 12, SEM-Micrograph of the cemented particles, TP03

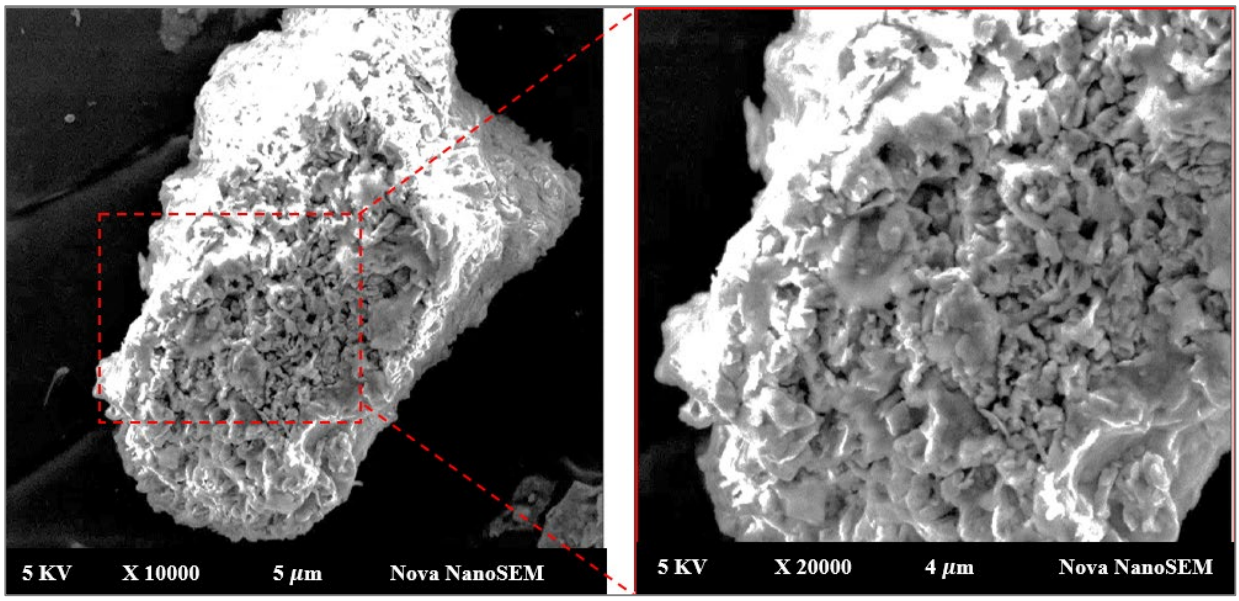

Figure 13, SEM-Micrograph of a tubular porous aggregation, TP03

Appendix D: Loads from typical houses in Mount Moorosi

Description	Best reference	Weight per meter length, kN/m
VERTICAL ACTIONS		
Wall (permanent)		
Size of one hollow brick: length = 0.39 m, breadth = 0.19 m and height = 0.19 m	Capebrick, 2019	
Unit weight of bricks = 18.9 kN/m^3	National code of India, 2005	
Number of bricks on one column of the brick wall + foundation = (2.5 + 0.45) /0.19 = 15. 5 no		
Total wall load per meter = ((0.19 x 0.19 x 0.39) – (0.09 x 0.19 x 0.12 x 2) /0.39) x 18.9 x 15.5		**7.493**
Blinding concrete (permanent)		
Unit weight of concrete = 23 kN/m^3	SANS 10160-2	
Blinding width is 0.6 m and thickness is 0.15 m		
Load per meter = 0.15 x 0.6 x 23 = 2.07 kN/m		**2.070**
Roofing		
Corrugated sheets (permanent)		

Description	Best reference	Weight per meter length, kN/m
Weight per unit area = 0.048 kN/m^2	National code of India, 2005	
Load per meter unit length = 0.048 x 1 = 0.048 kN/m		**0.048**
Rafters (permanent)		
Unit weight of timber = 7 kN/m^3	SANS 10160-2	
8.9 m rafters, width = 0.047m, breadth = 0.100 m		
Load per meter = 7 x 0.047 x 0.100 = 0.04 kN/m		**0.033**
7.9 m rafters width = 0.047m, breadth = 0.100 m		
Load = 7 x 0.047 = 6.008 x 0.100 = 0.040kN/m		**0.033**
Snow load on roof (imposed)		
Unit weight of snow = 3 kN/m^3	EN 1991-1-3	
Maximum snow thickness in Mount Moorosi from 2009 to 2019 = 0.35 m	World weather online, 2019	
Ground snow pressure, Sr = 0.35 x 3 = 1.050 kN/m^2		
Snow pressure on roofs, S = μ_ICeCtSr μ_I is the shape coefficient (0.8), Ce is the exposure coefficient (1.2) and Ct is the thermal coeffient (1)	EN 1991-1-3	
S = 0.8 x 1.2 x 1 x 1.05 = 1.01 kN/m^2		
Imposed loads on roofs		
Snow load per unit m = 1.01 x 1 = 1.01 kN/m		**1.008**
TOTAL VERTICAL LOAD		**10.685**
HORIZONTAL IMPOSED LOAD		
Wind loads		
$F_w = C_sC_dC_fq_p(Z_e)A_{ref}$	SANS 10160-3:2009	
C_sC_d are the structural factors (1), C_f is the force coefficient of structures (0.2), A_{ref} is the reference area of the structure (length x height), $q_p(Ze)$ is the peak wind speed pressure = $0.5pv^2$ where p is the wind density (0.976) and v is the wind speed		
Average gust wind speed in Mount Moorosi from 2009 to 2019, v = 4.87 m/s	World weather online, 2019	

Description	Best reference	Weight per meter length, kN/m
Fw = 1 x 0.2 x 8.9 x 2.5 x 0.5 x 0.976 x (4.87^2) = 52. 0 N		
Fw = 52.0/1000 = 0.052 kN		
Wind load per unit meter = 0.052/1 = 0.053 kN/m		**0.052**